



**IJOER**  
RESEARCH JOURNAL

ISSN  
2395-6992

# International Journal of Engineering Research & Science



[www.ijoer.com](http://www.ijoer.com)  
[www.adpublications.org](http://www.adpublications.org)

Volume-3! Issue-6 ! June, 2017

[www.ijoer.com](http://www.ijoer.com) ! [info@ijoer.com](mailto:info@ijoer.com)

## Preface

We would like to present, with great pleasure, the inaugural volume-3, Issue-6, June 2017, of a scholarly journal, *International Journal of Engineering Research & Science*. This journal is part of the AD Publications series *in the field of Engineering, Mathematics, Physics, Chemistry and science Research Development*, and is devoted to the gamut of Engineering and Science issues, from theoretical aspects to application-dependent studies and the validation of emerging technologies.

This journal was envisioned and founded to represent the growing needs of Engineering and Science as an emerging and increasingly vital field, now widely recognized as an integral part of scientific and technical investigations. Its mission is to become a voice of the Engineering and Science community, addressing researchers and practitioners in below areas

Chemical Engineering	
Biomolecular Engineering	Materials Engineering
Molecular Engineering	Process Engineering
Corrosion Engineering	
Civil Engineering	
Environmental Engineering	Geotechnical Engineering
Structural Engineering	Mining Engineering
Transport Engineering	Water resources Engineering
Electrical Engineering	
Power System Engineering	Optical Engineering
Mechanical Engineering	
Acoustical Engineering	Manufacturing Engineering
Optomechanical Engineering	Thermal Engineering
Power plant Engineering	Energy Engineering
Sports Engineering	Vehicle Engineering
Software Engineering	
Computer-aided Engineering	Cryptographic Engineering
Teletraffic Engineering	Web Engineering
System Engineering	
Mathematics	
Arithmetic	Algebra
Number theory	Field theory and polynomials
Analysis	Combinatorics
Geometry and topology	Topology
Probability and Statistics	Computational Science
Physical Science	Operational Research
Physics	
Nuclear and particle physics	Atomic, molecular, and optical physics
Condensed matter physics	Astrophysics
Applied Physics	Modern physics
Philosophy	Core theories

Chemistry	
Analytical chemistry	Biochemistry
Inorganic chemistry	Materials chemistry
Neurochemistry	Nuclear chemistry
Organic chemistry	Physical chemistry
Other Engineering Areas	
Aerospace Engineering	Agricultural Engineering
Applied Engineering	Biomedical Engineering
Biological Engineering	Building services Engineering
Energy Engineering	Railway Engineering
Industrial Engineering	Mechatronics Engineering
Management Engineering	Military Engineering
Petroleum Engineering	Nuclear Engineering
Textile Engineering	Nano Engineering
Algorithm and Computational Complexity	Artificial Intelligence
Electronics & Communication Engineering	Image Processing
Information Retrieval	Low Power VLSI Design
Neural Networks	Plastic Engineering

Each article in this issue provides an example of a concrete industrial application or a case study of the presented methodology to amplify the impact of the contribution. We are very thankful to everybody within that community who supported the idea of creating a new Research with IJOER. We are certain that this issue will be followed by many others, reporting new developments in the Engineering and Science field. This issue would not have been possible without the great support of the Reviewer, Editorial Board members and also with our Advisory Board Members, and we would like to express our sincere thanks to all of them. We would also like to express our gratitude to the editorial staff of AD Publications, who supported us at every stage of the project. It is our hope that this fine collection of articles will be a valuable resource for *IJOER* readers and will stimulate further research into the vibrant area of Engineering and Science Research.

Mukesh Arora  
(Chief Editor)

## **Board Members**

### **Mukesh Arora(Editor-in-Chief)**

BE(Electronics & Communication), M.Tech(Digital Communication), currently serving as Assistant Professor in the Department of ECE.

### **Dr. Omar Abed Elkareem Abu Arqub**

Department of Mathematics, Faculty of Science, Al Balqa Applied University, Salt Campus, Salt, Jordan, He received PhD and Msc. in Applied Mathematics, The University of Jordan, Jordan.

### **Dr. AKPOJARO Jackson**

Associate Professor/HOD, Department of Mathematical and Physical Sciences, Samuel Adegboyega University, Ogwa, Edo State.

### **Dr. Ajoy Chakraborty**

Ph.D.(IIT Kharagpur) working as Professor in the department of Electronics & Electrical Communication Engineering in IIT Kharagpur since 1977.

### **Dr. Ukar W.Soelistijo**

Ph D , Mineral and Energy Resource Economics, West Virginia State University, USA, 1984, Retired from the post of Senior Researcher, Mineral and Coal Technology R&D Center, Agency for Energy and Mineral Research, Ministry of Energy and Mineral Resources, Indonesia.

### **Dr. Heba Mahmoud Mohamed Afify**

h.D degree of philosophy in Biomedical Engineering, Cairo University, Egypt worked as Assistant Professor at MTI University.

### **Dr. Aurora Angela Pisano**

Ph.D. in Civil Engineering, Currently Serving as Associate Professor of Solid and Structural Mechanics (scientific discipline area nationally denoted as ICAR/08—"Scienza delle Costruzioni"), University Mediterranea of Reggio Calabria, Italy.

### **Dr. Faizullah Mahar**

Associate Professor in Department of Electrical Engineering, Balochistan University Engineering & Technology Khuzdar. He is PhD (Electronic Engineering) from IQRA University, Defense View, Karachi, Pakistan.

### **Dr. S. Kannadhasan**

Ph.D (Smart Antennas), M.E (Communication Systems), M.B.A (Human Resources).

### **Dr. Christo Ananth**

Ph.D. Co-operative Networks, M.E. Applied Electronics, B.E Electronics & Communication Engineering Working as Associate Professor, Lecturer and Faculty Advisor/ Department of Electronics & Communication Engineering in Francis Xavier Engineering College, Tirunelveli.

## **Dr. S.R.Boselin Prabhu**

Ph.D, Wireless Sensor Networks, M.E. Network Engineering, Excellent Professional Achievement Award Winner from Society of Professional Engineers Biography Included in Marquis Who's Who in the World (Academic Year 2015 and 2016). Currently Serving as Assistant Professor in the department of ECE in SVS College of Engineering, Coimbatore.

## **Dr. Maheshwar Shrestha**

Postdoctoral Research Fellow in DEPT. OF ELE ENGG & COMP SCI, SDSU, Brookings, SD  
Ph.D, M.Sc. in Electrical Engineering from SOUTH DAKOTA STATE UNIVERSITY, Brookings, SD.

## **Zairi Ismael Rizman**

Senior Lecturer, Faculty of Electrical Engineering, Universiti Teknologi MARA (UiTM) (Terengganu) Malaysia  
Master (Science) in Microelectronics (2005), Universiti Kebangsaan Malaysia (UKM), Malaysia. Bachelor (Hons.) and Diploma in Electrical Engineering (Communication) (2002), UiTM Shah Alam, Malaysia

## **Dr. D. Amaranatha Reddy**

Ph.D.(Postdoctoral Fellow,Pusan National University, South Korea), M.Sc., B.Sc. : Physics.

## **Dr. Dibya Prakash Rai**

Post Doctoral Fellow (PDF), M.Sc.,B.Sc., Working as Assistant Professor in Department of Physics in Pachhungga University College, Mizoram, India.

## **Dr. Pankaj Kumar Pal**

Ph.D R/S, ECE Deptt., IIT-Roorkee.

## **Dr. P. Thangam**

BE(Computer Hardware & Software), ME(CSE), PhD in Information & Communication Engineering, currently serving as Associate Professor in the Department of Computer Science and Engineering of Coimbatore Institute of Engineering and Technology.

## **Dr. Pradeep K. Sharma**

PhD., M.Phil, M.Sc, B.Sc, in Physics, MBA in System Management, Presently working as Provost and Associate Professor & Head of Department for Physics in University of Engineering & Management, Jaipur.

## **Dr. R. Devi Priya**

Ph.D (CSE),Anna University Chennai in 2013, M.E, B.E (CSE) from Kongu Engineering College, currently working in the Department of Computer Science and Engineering in Kongu Engineering College, Tamil Nadu, India.

## **Dr. Sandeep**

Post-doctoral fellow, Principal Investigator, Young Scientist Scheme Project (DST-SERB), Department of Physics, Mizoram University, Aizawl Mizoram, India- 796001.

## **Mr. Abilash**

MTech in VLSI, BTech in Electronics & Telecommunication engineering through A.M.I.E.T.E from Central Electronics Engineering Research Institute (C.E.E.R.I) Pilani, Industrial Electronics from ATI-EPI Hyderabad, IEEE course in Mechatronics, CSHAM from Birla Institute Of Professional Studies.

## **Mr. Varun Shukla**





M.Tech in ECE from RGPV (Awarded with silver Medal By President of India), Assistant Professor, Dept. of ECE, PSIT, Kanpur.

## **Mr. Shrikant Harle**

Presently working as a Assistant Professor in Civil Engineering field of Prof. Ram Meghe College of Engineering and Management, Amravati. He was Senior Design Engineer (Larsen & Toubro Limited, India).

## Table of Contents

S.No	Title	Page No.
1	<p><b>Numerical Calculation and Analysis of the Normal Relationship of the Dual-Frequency Altimeter Backscatter Coefficient</b>  <b>Authors:</b> Jiasheng Tian, Junwu Tao, Jian Shi</p> <p> <b>DOI:</b> 10.25125/engineering-journal-IJOER-APR-2017-24</p> <p> <b>DIN Digital Identification Number:</b> Paper-June-2017/IJOER-APR-2017-24</p>	01-14
2	<p><b>Hydration kinetics of calcium sulphate hemihydrate modified by water-soluble polymers</b>  <b>Authors:</b> Patrycja Mróz, Maria Mucha</p> <p> <b>DOI:</b> 10.25125/engineering-journal-IJOER-MAY-2017-25</p> <p> <b>DIN Digital Identification Number:</b> Paper-June-2017/IJOER-MAY-2017-25</p>	15-19
3	<p><b>A new novel crosslinker with space structure for low-polymer-loading fracturing fluid</b>  <b>Authors:</b> Yuan Qing, Li Fengguang, Bi Yanxia, Niu Zengqian, Li Shiheng, Cai Jingchao, Tan Rui, Lu Wei, Chang Qing, Chen Deyu</p> <p> <b>DOI:</b> 10.25125/engineering-journal-IJOER-JUN-2017-2</p> <p> <b>DIN Digital Identification Number:</b> Paper-June-2017/IJOER-JUN-2017-2</p>	20-26
4	<p><b>ECC-based User Authentication Scheme for Wireless Sensor Networks</b>  <b>Authors:</b> Imanbaev Temirlan, Yue Li</p> <p> <b>DOI:</b> 10.25125/engineering-journal-IJOER-JUN-2017-5</p> <p> <b>DIN Digital Identification Number:</b> Paper-June-2017/IJOER-JUN-2017-5</p>	27-30
5	<p><b>Utilization of bottle caps in concrete</b>  <b>Authors:</b> S.T. Rathod, L.R.Bankar, U.R.Hakepatil, M.M.Vhanamane, S.S.Warpe</p> <p> <b>DOI:</b> 10.25125/engineering-journal-IJOER-JUN-2017-6</p> <p> <b>DIN Digital Identification Number:</b> Paper-June-2017/IJOER-JUN-2017-6</p>	31-45
6	<p><b>Haze Removal Using Color Attenuation Prior With Varying Scattering Coefficients</b>  <b>Authors:</b> Anandhu Balakrishnan, Shine P James</p> <p> <b>DOI:</b> 10.25125/engineering-journal-IJOER-JUN-2017-10</p> <p> <b>DIN Digital Identification Number:</b> Paper-June-2017/IJOER-JUN-2017-10</p>	46-57
7	<p><b>Switching System, a Zero Power Standby Solution</b>  <b>Authors:</b> Stefan Mozar FIEEE, Nobuo Funabiki</p> <p> <b>DOI:</b> 10.25125/engineering-journal-IJOER-JUN-2017-7</p> <p> <b>DIN Digital Identification Number:</b> Paper-June-2017/IJOER-JUN-2017-7</p>	58-63
8	<p><b>Kinetic modeling of Immobilized Yeast Batch Fermentation</b>  <b>Authors:</b> Terkida Prifti (Vaso), Luljeta Pinguli, Ilirjan Malollari</p> <p> <b>DOI:</b> 10.25125/engineering-journal-IJOER-JUN-2017-8</p> <p> <b>DIN Digital Identification Number:</b> Paper-June-2017/IJOER-JUN-2017-8</p>	64-68

9	<p><b>Water Chemistry Management toward Corrosion for Secondary Cooling Piping of Multi Purpose Reactor GA Siwabessy Indonesia</b></p> <p><b>Authors:</b> Geni Rina Sunaryo, Herry Sander, Djarot S. Wisnubroto</p> <p> <b>DOI:</b> 10.25125/engineering-journal-IJOER-JUN-2017-9</p> <p> <b>DIN Digital Identification Number:</b> Paper-June-2017/IJOER-JUN-2017-9</p>	69-73
10	<p><b>Additive Manufacturing of PE/Fluorouracil Waffles for Implantable Drug Delivery in Bone Cancer Treatment</b></p> <p><b>Authors:</b> G. V. Salmoria, F. E. Vieira, G. B. Ghizoni, I. M. Gindri, L. A. Kanis</p> <p> <b>DOI:</b> 10.25125/engineering-journal-IJOER-JUN-2017-12</p> <p> <b>DIN Digital Identification Number:</b> Paper-June-2017/IJOER-JUN-2017-12</p>	74-81



# Numerical Calculation and Analysis of the Normal Relationship of the Dual-Frequency Altimeter Backscatter Coefficient

Jiasheng Tian<sup>1</sup>, Junwu Tao<sup>2</sup>, Jian Shi<sup>3</sup>

<sup>1,3</sup>School of Electronic Information and Communications, Huazhong University of Science and Technology, Wuhan City, China.

<sup>2</sup>Researcher at Laboratoire Plasma et Conversion d'Energie (LAPLACE), INP-ENSEEIH, 2, rue Charles Camichel- BP7122-31071 Toulouse Cedex7, France.

**Abstract**—To improve effectively sea surface wind speed retrieval accuracy when it is raining, it is very interesting to find out a more accurate normal relationship between Ku band backscatter coefficient  $\sigma_{ku}^0$  and C band backscatter coefficient  $\sigma_c^0$  for a dual frequency altimeter (13.58GHz/5.25GHz). In this paper an electromagnetic scattering model with a rough surface profiles is established. In terms of the established rough sea surface model  $\sigma_{ku}^0$  and  $\sigma_c^0$  are calculated by electromagnetic numerical methods of method of moment (MOM) and Kirchhoff approximation (KA) when the rms of the rough surface is various. The simulation results are in a good agreement by these two different methods: MOM and KA. Those calculated results show that the relationship between  $\sigma_{ku}^0$  and  $\sigma_c^0$  obtained by calculating electromagnetic scattering from Gaussian random rough sea surface profiles exists positive differences from the normal relationships while those obtained by calculating electromagnetic scattering from Exponential rough sea surface profiles exist negative differences from thoses. It is obvious that the calculated relationship can be in a good agreement with an empirical normal relationship by adjusting compositions of those ocean spectrums. It is a good way to find out the normal relationship between  $\sigma_{ku}^0$  and  $\sigma_c^0$  by theoretical calculation and analysis, and also is an effective way to study the ocean spectrum and sea states.

**Keywords**—Dual frequency altimeter, Normal relationship, Backscatter coefficient, MOM, KA.

## I. INTRODUCTION

The Topex/Poseidon satellite, which was developed by National Aeronautics and Space Administration (NASA) and the French Space Agency (CNES) was launched on August 10,1992, carrying the first dual frequency altimeter (13.58GHz/5.25GHz). It was because of the presence of the dual-frequency altimeter, removing rainfall influence on wind speed inversion had a substantial progress. It was known that the prime effect of rainfall was the attenuation of the return pulse and there was an order of magnitude larger at Ku band than at C-band, in addition to attenuation, rain can also change the shape of the return pulse and hence the measurement of the significant wave height (swh) and sea surface height (ssh) can also be affected. In terms of Topex/Poseidon measurements, a statistical relationship (or normal relationship) between  $\sigma_{ku}^0$  and  $\sigma_c^0$  was presented in [1]. With the normal relationship the rainfall influence on  $\sigma_{ku}^0$  has to be eliminated in order to improve wind speed retrieval. After that many normal relationships [2-4] were put forward to be used to define a new rain flag to detect all rain events, as well as to improve wind speed retrieval. Those presented normal relationships are all empirical and statistical in terms of measurements provided from a certain altimeter. For  $\sigma_{ku}^0$  and  $\sigma_c^0$  there is a correlation on the physical mechanism, but now it is difficult to theoretically reduce the formula, And thus many empirical relationships were usually proposed and adopted.

The main motivations for this study are firstly, to better understand the normal relationship between  $\sigma_{ku}^0$  and  $\sigma_c^0$  when rain is not present, and secondly, to show that the differential effect of oceanic spectrums on Ku and C band microwave signals can be used to define a better and possibly operational normal relationship. A further goal is to investigate the possibility of using dual-frequency altimeter data to improve sea surface wind speed retrieval [5,6].

## II. ELECTROMAGNETIC MODEL AND NUMERICAL CALCULATION

The electromagnetic model is established by Monte Carlo simulation. Numerical calculations are carried out by MOM and KA.

**2.1 Electromagnetic scattering model**

**2.1.1 Ocean spectrum**

It is more convenient to supposing that the ocean spectrum case is still a Gaussian process with the ocean spectral density. For 1-D spectrum, the Gaussian spectrum is

$$W(k) = \frac{h^2 l}{2\sqrt{\pi}} \exp\left(-\frac{k^2 l^2}{4}\right) \tag{1}$$

If the ocean spectrum case is an exponential process, it may be given as

$$W(k) = \frac{h^2 l}{\pi(1+k^2 l^2)} \tag{2}$$

where  $k$  is space wave number,  $h$  and  $l$  are RMS height and correlation length. Other spectrums are not studied in this paper.

**2.1.2 Random Rough Surface**

We generate Gaussian or exponential rough surface with Monte Carlo simulation and Fourier Transform. For 1-D case, we have

$$f(x) = \frac{1}{L} \sum_{i=-N/2+1}^{N/2} F(k_i) \exp(jk_i x) \tag{3}$$

where

$$F(k_i) = \frac{2\pi}{\sqrt{2\Delta k}} \sqrt{W(k_i)} \begin{cases} N(0,1) + jN(0,1), & i \neq 0, N/2 \\ N(0,1), & i = 0, N/2 \end{cases} \tag{4}$$

Some parameters were defined in [7]. We can see that the exponential spectrum surface of fig.2.2 is more than spiky than the Gaussian surface of fig.2.1.

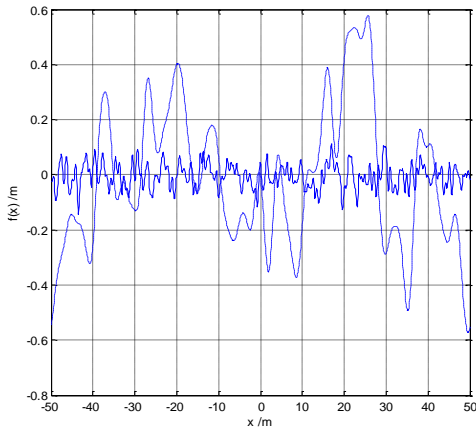


**FIG.2.1 1D GAUSSIAN ROUGH SURFACE PROFILE --  $h=0.221m, l=2.21m$ ; —  $h=0.0442m, l=4.42m$**

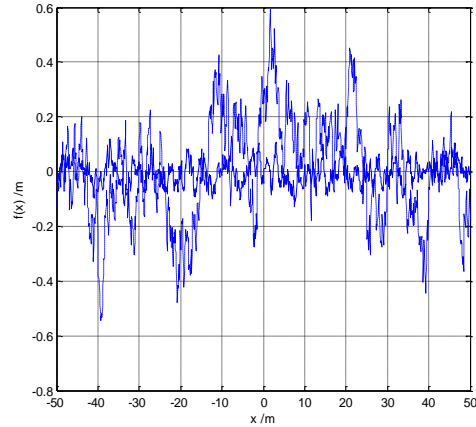


**FIG.2.2 1D EXPONENTIAL ROUGH SURFACE PROFILE --  $h=0.221m, l=2.21m$ ; —  $h=0.0442m, l=4.42m$**

**2.2 MOM**

Consider an incident wave  $\psi_{in}(\vec{r})$  impinging upon a rough sea surface (fig.2.1 or fig.2.2) with height profile  $z=f(x)$ . The wave function  $\psi(\vec{r})$  can be given as

$$\psi(\vec{r}) = \psi_{in}(\vec{r}) + \psi_s(\vec{r}) \tag{5}$$

Where  $\psi_s(\vec{r})$  is the scattered wave and position vector  $\vec{r} = x\hat{x} + z\hat{z}$ . In terms of wave equation and Green's theorem, we can obtain

$$\begin{aligned} & \psi_{in}(\vec{r}') + \int_s ds \hat{n} \cdot [\psi(\vec{r}) \nabla g(\vec{r}, \vec{r}') - g(\vec{r}, \vec{r}') \nabla \psi(\vec{r})] \\ & = \begin{cases} \psi(\vec{r}') & \vec{r}' \in V_0 \\ 0 & \vec{r}' \in V_1 \end{cases} \end{aligned} \tag{6}$$

Note that in equation (6),  $\bar{r}$  is on the sea surface while  $\bar{r}'$  is in region  $V_0$  above the sea surface or in region  $V_1$  under the sea surface. Applying electromagnetic field boundary conditions, we can obtain

$$\sum_{n=1}^N A_{mn} U_n + \sum_{n=1}^N B_{mn} \psi_n = b_m \tag{7}$$

$$\sum_{n=1}^N A_{mn}^{(1)} \rho U_n + \sum_{n=1}^N B_{mn}^{(1)} \psi_n = 0 \tag{8}$$

Some quantities in equation (7) and equation (8) can be defined in[7].

### 2.3 KA

From equation (1) and the second Green's theorem, the scattered field  $\psi_s(\bar{r})$  can be given by[8]

$$\begin{aligned} \psi_s(\bar{r}) &= \psi(\bar{r}) - \psi_{in}(\bar{r}) \\ &= \int_c \left[ \psi(\bar{r}') \frac{\partial g(\bar{r}, \bar{r}')}{\partial \hat{n}'} - g(\bar{r}, \bar{r}') \frac{\partial \psi(\bar{r}')}{\partial \hat{n}'} \right] dl' \end{aligned} \tag{9}$$

Where

$$\psi(\bar{r}') = \psi_{in}(\bar{r}') [1 + R(\bar{r}')] \tag{10}$$

$$\frac{\partial \psi(\bar{r}')}{\partial \hat{n}'} = \frac{\partial \psi_{in}(\bar{r}')}{\partial \hat{n}'} [1 - R(\bar{r}')] \tag{11}$$

position vector  $\bar{r}'$  is on the rough sea surface and  $R(\bar{r}')$  is Fresnel reflection coefficient other parameters are defined in[8-9].

## III. SIMULATION RESULTS

In terms of equation (7), equation (8) and equation (9) we can calculate scattering from the rough sea surface with Gaussian or exponential distribution. In order to avoid artificial reflection from the two endpoints of the rough surface, we taper the incident wave so that the incident wave decays to zero in a Gaussian manner for large  $x$ .

In fig.3.1, the results by mom and KA are in a good agreement and valid. The rough surface is Gaussian. The scattering from the rough surface with Gaussian distribution is more than the normal relationship does, while the scattering from the rough surface with exponential distribution is less than the normal relationship, as shown in fig.3.2. Note that the scattering from the rough surface with Gaussian and exponential distribution is among some normal relationships. It is obvious that a normal relationship only stands for a practical sea state with one or several ocean spectrums. From fig.3.1 and fig.3.2 it is obvious that the normal relationship between  $\sigma_{ku}^0$  and  $\sigma_c^0$  is relative to several ocean spectrums.

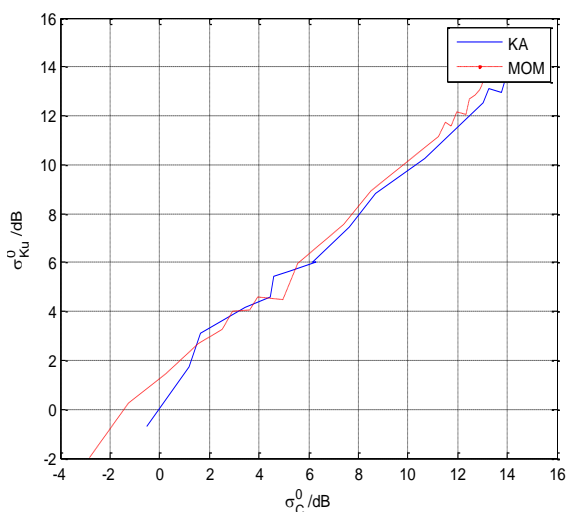


FIG.3.1 RELATIONSHIP BETWEEN  $\sigma_{ku}^0$  and  $\sigma_c^0$

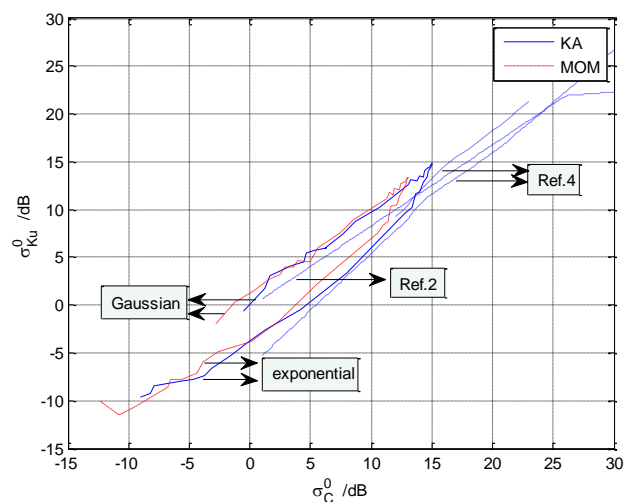


FIG.3.2 THE CALCULATED RELATIONSHIP AND SEVERAL NORMAL RELATIONSHIPS

All in all, for different oceans and sea states there perhaps exists different normal relationships with different ocean spectrums.

#### IV. CONCLUSION

Applying MOM and KA, we finish simulating scattering from Gaussian random rough sea surface profiles and exponential random rough sea surface profiles with various rms height  $h$ , respectively. The relationship between  $\sigma_{ku}^0$  and  $\sigma_c^0$  is presented and can be in a good agreement with the normal relationships by adjusting or simulating ocean spectrum compositions. The relationship between  $\sigma_{ku}^0$  and  $\sigma_c^0$  from Gaussian and exponential distribution is among those normal relationships. Our simulating is a good way to study the normal relationships between  $\sigma_{ku}^0$  and  $\sigma_c^0$ .

#### ACKNOWLEDGEMENTS

The project is supported by National Natural Science Foundation of China (No. 41376181, No.41676090).

#### REFERENCES

- [1] Quarty G D, Guymer T H, Srokosz M A, "The effects of rain on Topex radar altimeter data"[J], Journal of Atmospheric and Oceanic Technology, 1996,13(6):1209-1229.
- [2] Le Yang, Juhong Zou, Mingsen Lin, Delu Pan, "Method to correct both foam and rain effects on dual frequency altimeter Jason1 wind measurements in typhoon Shanshan", Proceedings of SPIE-The International Society for Optical Engineering, October 2008.
- [3] Ge Chen, "A dual-frequency approach for retrieving sea surface wind speed from TOPEX altimetry", Journal of Geophysical Research, Vol.107,NO.C12,3226, doi:10. 1029/2001JC001098, 2002.
- [4] Jiang Zhu-hui, Huang Si-xun, Liu Bo, "Standard relationship adjustment of dual frequency altimeter backscatter coefficient", Journal of PLA University of Science and Technology(Natural Science Edition), Vol.12,NO.5,Oct. 2011,pp.555-558.
- [5] Jiasheng Tian, Hang Xue, Jian Shi, "Study on the Parameters Retrieval and Correction Algorithms of Radar Altimeter Accounting for the Mispointing Angle", Remote Sensing Science, August 2015, Vol.3 Issue 3,pp.36-41.
- [6] Jiasheng Tian; Qiaoyun Liu; Wan Pan; Jian Shi; "Improved algorithm of retrieving oceanic surface wind speed based on a stratified media model at high sea states", IET Microwaves, Antennas & Propagation, Volume 8, Issue 15, 09 December 2014. pp.1333- 1339.
- [7] Leung Tsang, Jin Au Kong, Kung-Hau Ding, Chi On Ao, "Scattering of Electromagnetic Waves- Numerical Simulations", A Wiley-Interscience Publication, John Wiley & Sons, Inc. 2001.
- [8] J. A. Ogilvy, "Theory of Wave Scattering from Random Rough Surface", Bristol:Adam Hilger, 1991.
- [9] Jiasheng Tian, Jian Tong, Jian Shi, and Liangqi Gui, "A new approximate fast method of computing the scattering from multilayer rough surfaces based on the Kirchhoff approximation", Radio Science, Vol.52, 12, February 2017, pp.186-195.

# Hydration kinetics of calcium sulphate hemihydrate modified by water-soluble polymers

Patrycja Mróz<sup>1\*</sup>, Maria Mucha<sup>2</sup>

Faculty of Process and Environmental Engineering, Lodz University of Technology, Wólczajska 215, 90-924 Łódź, Poland

**Abstract**— Pastes based on gypsum (calcium sulphate hemihydrate) and two chosen water-soluble polymer admixtures, i.e. hydroxyethylmethyl cellulose (HEMC) and poly(vinyl acetate) (PVAC) were prepared. The impacts of the polymers on gypsum setting, as well as thermal and mechanical properties were studied. Heat effect and the rate of setting depending on water to gypsum ratio and the presence of admixtures were measured. The results have shown a strong effect of the polymer admixture (1%) on the prolongation of gypsum setting time. The presence of polymer molecules in water solution hinders the crystallization process of gypsum dihydrate. HEMC and PVAC have also a significant influence on gypsum mechanical properties especially at low water content. Kinetics of the setting process of gypsum hemihydrate is discussed.

**Keywords**— admixture, gypsum, heat of hydration/crystallization, hydroxyethylmethyl cellulose, poly(vinyl acetate), setting.

## I. INTRODUCTION

Dramatically altering setting rates as well as microstructures and properties of cement or gypsum products are often accompanied by the use of admixtures. They include accelerators or retarders of setting. Better understanding of the chemistry and physics of product hydration and setting is important. More progress can be made by systematically examining how the setting rate is influenced by chemical admixtures.

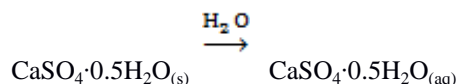
Also gypsum industry turns to sustainable development and production of greener concrete [1-6]. Thus, instead of toxic materials (e.g. KNO<sub>3</sub>, NH<sub>4</sub>Cl, resins such as sulfonated melanin or sulfonated naphthalene [7]) water-soluble (environment friendly) polymers are used.

Gypsum products are known for their fire resistance, thermal insulation and acoustic properties. However, due to low water resistance and mechanical strength, gypsum is not a suitable material for external construction works. The protection of gypsum requires prevention against penetration of moisture to avoid any damage [8]. Polymer plasticizers are often used as additives in construction materials (gypsum, concrete) in order to reduce water content which generally leads to higher strength of the product, extended or reduced setting time and lowering the possibility of mixture separation. A longer duration of the mixture adequate consistency improves workability and flowability of gypsum and concrete.

Appropriate mixing of hemihydrate sulphate (gypsum) with 1% of polymer (e.g. cellulose derivatives) substantially modifies the mechanical properties, rate of setting (crystallization) and water retention of the material obtained. This has an important impact on the application.

Hemihydrate sulphate (gypsum) hydration involves a set of coupled chemical and physical processes [9,10]:

1. Dissolution of hemihydrate involves detachment of molecules from a solid surface in contact with water



2. Diffusion involves the transport of solution components through the paste pores and nucleation which initiates the precipitation of solids (dihydrate is less soluble in water).
3. A complex reaction between simple ions to form ion complexes together with hydration of a hemihydrate into dihydrate.



4. Adsorption and accumulation of ions or other molecular units at an interface (crystallization).

These processes may operate in series, parallel or in some complex combinations. Each stage can be a rate-controlling stage.

The stages are affected by the presence of admixtures leading to a possible control of the hydration process and material properties. Garg et al. [8] have studied the properties of fluorogypsum – a slag composite binder. They found much improved flexural strength, prolonged setting time and increased thermal conductivity in comparison to gypsum without additives. Tesárek et al. [11] found that gypsum porosity increased quickly with an increasing amount of water in the mixture.

One of the main polymeric substances added to construction materials as admixtures are cellulose ethers. Cellulose is one of natural polymers having crystalline complex structure. This feature makes it insoluble in water. On the other hand, the crystalline region of cellulose can be disrupted due to modification when the hydroxyl group of cellulose is substituted with methoxy, hydroxypropyl and hydroxyethyl groups. Thus formed cellulose ethers (as organic admixtures) are soluble in water also as a result of amorphous characteristics [12]. The cellulose ethers like hydroxypropylmethyl cellulose (HPMC) and hydroxyethylmethyl cellulose (HEMC) are non-toxic and edible. In the dissolved state they are viscous enough to easily form films. Thus they found widespread use in medicine and architecture.

HEMC is one of cellulose ethers affecting the properties of construction materials and improving their workability. In the case of cement it was proved that macromolecules had an impact on cement and gypsum hydration delay [13,14]. The authors predicted that the biggest effect on the hydration delay had the presence of a methoxyl group.

Plank et al. [15,16] showed that HEMC improved water retention of cement and gypsum. Already a 0.3% dose of HEMC causes 97% of water retention capability. HEMC doses higher than 1% produce extremely viscous cement pastes. This effect is dependent on the molecular weight of the polymer sample. An increase in filtrate viscosity may play a role in the working mechanism of HEMC [17]. Currently, the main applications of HEMC and other cellulose ethers are wall plasters, floor screeds, water-proofing membranes, joint compounds for gypsum board paneling and cement tile adhesives.

Another polymer used also as an admixture in construction materials is poly(vinyl acetate) (PVAC) and its copolymers. It was found that the use of PVAC as a plasticizer of cement or gypsum [18] improved material adhesion to the substrate. Furthermore, the application of PVAC does not require preservatives and fungicides, the polymer inhibits the growth of mildew [19].

In this paper, both HEMC and PVAC polymers are chosen as admixtures to modify gypsum properties which have not been sufficiently tested up to now. Research methods such as calorimetry, setting and mechanical tests help us to discuss and identify the effect of polymer admixture on the kinetics of solid gypsum plaster formation leading to its specific properties.

## II. MATERIAL AND METHODS

### 2.1 Materials

Material used in this study was gypsum – calcium sulphate hemihydrate ( $\beta$  form) supplied by Dolina Nidy (Poland). The gypsum meets the requirements of standard PN- EN 13279-1:2009. Calcium sulphate ( $\text{CaSO}_4$ ) in gypsum amounted to 90.98%. Other components were:  $\text{CaCO}_3$  – 2.79%,  $\text{SiO}_2$  – 1.62%, montmorillonite – 3.07%, illite – 0.79%, and chlorite – 0.16%. Distilled water was used for mixing gypsum with admixtures. Hydroxyethylmethyl cellulose (HEMC) ( $\mu = 3000$  mPa\*s) and poly(vinyl acetate) (PVAC) were supplied by Atlas Company (Poland).

### 2.2 Preparation of samples

The following samples were prepared to use in calorimetric, setting time and mechanical studies: gypsum powder (hemihydrate) without admixtures, gypsum doped with 1% HEMC or 1% PVAC. Various amounts of water from 35 to 50% by weight (water to gypsum ratio  $x = 0.54 - 1.0$ ) were added. The samples were prepared according to standard PN-86 B-04360 (Plasters, Test methods, Physical characteristic determination).

Polymer admixtures in appropriate amounts were first dissolved in distilled water at room temperature. Then, the composition with gypsum powder was vigorously mixed for 30 seconds using a mechanical stirrer.

### 2.3 Calorimetric studies of the samples

A Mettler differential scanning calorimeter (DSC) model FP90 was used to study the hydration process of gypsum powder – hemihydrate with admixtures. Immediately after mixing samples of the paste (about 10 mg) were transferred in special capsules into the calorimeter chamber for measurements. At the first step the samples were kept for 2 hours at constant temperature of 30°C. Thus, heats of hydration and crystallization of hemihydrates-gypsum samples were investigated in

isothermal conditions. Then, at the second step the samples were heated at constant rate of  $10^{\circ}\text{C}/\text{min}$  from  $30^{\circ}\text{C}$  to  $250^{\circ}\text{C}$  in the air to measure dehydration by evolution of various states of water in the hydrated product.

## 2.4 Setting tests

The setting time was measured at room temperature using a Vicat's device (Master, Italy) equipped with a stainless steel needle and ebonite ring. Contact surface of the needle was polished after every measurement. The study consists in a measure of free needle penetration in to the gypsum paste every 30 seconds. The study was conducted according to standard PN-86 B-04360 (Plasters. Test methods. Physical characteristic determination.).

## 2.5 Mechanical tests

Mechanical bending test of flexural Young modulus and strength was carried out using Instron 3345 (Instron, USA).

Samples were prepared for the bending test by spreading gypsum plaster into rubber molds attached to the glass plates. Dimensions of the molds were 50 mm/18 mm/5 mm. The tests were repeated 6 times for every sample. Before the experiment the entire mold was smeared with oil. The applied samples were set for 48 hours at room temperature.

The test was conducted according to standard PN-86 B-04360 (Plasters. Test methods. Physical characteristic determination.).

## III. RESULTS AND DISCUSSION

Gypsum samples prepared with various water to gypsum ratios and containing two polymer admixtures – HEMC or PVAC (in weight fraction 1%) were studied by DSC in setting and mechanical experiments. Results are shown graphically and discussed. A difference between the effect of both admixtures on the process of gypsum – calcium hemihydrate sulphate hydration/crystallization kinetics measured by DSC and setting tests is shown.

### 3.1 Setting time

Setting of material is a transition period during which the physical state of material changes from paste to solid. This transformation occurs as a result of the development of hydration products which cause rigid connections between hydrating grains. It is usually characterized by two points in the hydration process, namely initial and final setting time. The development of connected hydration product which reflects the transition of material state was measured by the penetration resistance technique (Vicat needle test).

Figures 1 and 2 show selected results of the Vicat needle tests. The beginning of the setting period was estimated as the first inflection point on  $h = f(t)$  (where  $h$  is the height of the needle). The time of setting was measured as the time of the intersection of straight line on  $h = f(t)$  curve. The time from the onset of the experiment to the beginning of the setting period is known as the induction period  $t_i$ .

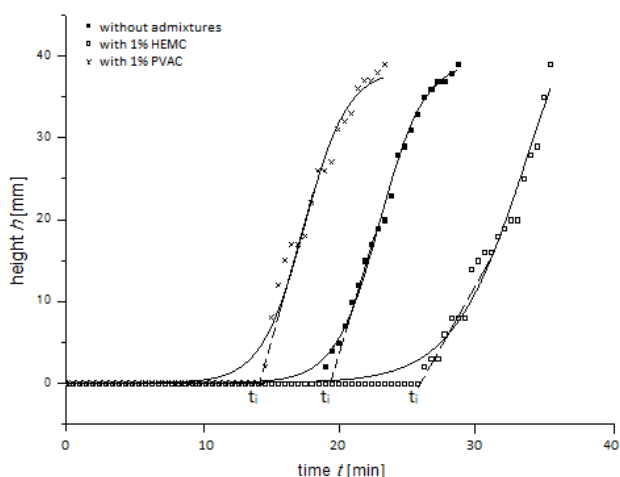


**FIG. 1. SETTING PROCESS  $h=f(t)$  OF SAMPLES WITH WATER TO GYPSUM RATIO  $x= 0.60$ .**

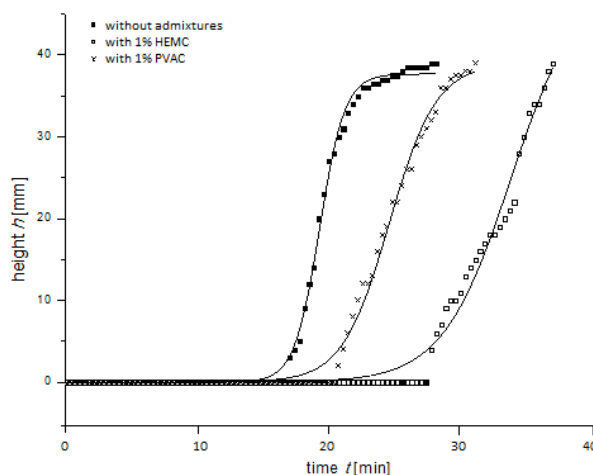
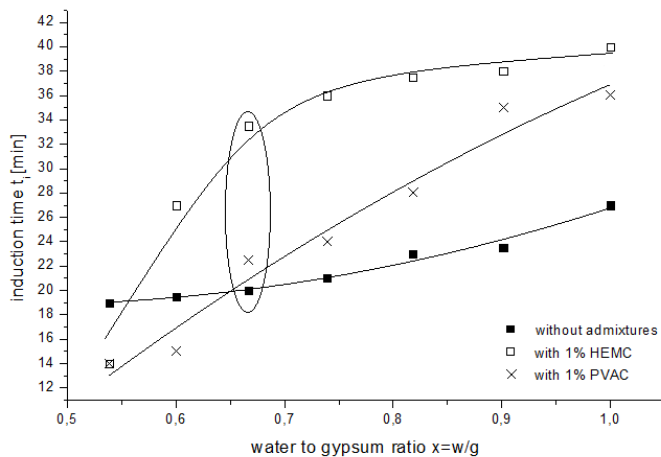


**FIG. 2. SETTING PROCESS  $h=f(t)$  OF SAMPLES WITH WATER TO GYPSUM RATIO  $x= 0.82$ .**

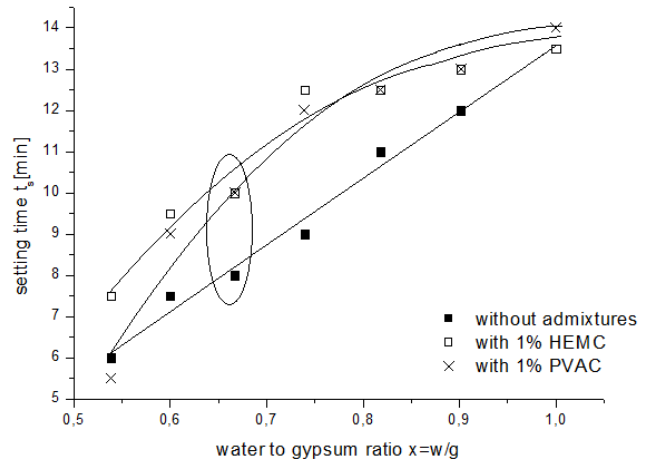
In the case of higher water content (higher water to gypsum ratio) the initiation of setting process followed later (induction time increased). Gypsum setting time was prolonged with a rising content of water.

Figure 1 shows the setting process of samples with water to gypsum ratio  $x$  equal to 0.60. The PVAC admixture reduces the setting induction period, while HEMC extends it. For higher water content the trend changes. Starting from  $x = 0.67$ , both HEMC and PVAC admixtures (Fig. 3) extend the setting induction time (Fig. 2 for  $x = 0.82$  water to gypsum ratio).

The observed retardation of setting in the case of the applied polymers can be the effect of disturbed diffusion of ions (also water) and molecules to the binder surface due to relatively rigid polymer molecule conformation in the water phase. No electrostatic interactions of polymer active groups with the binding surface of gypsum are predicted because the gypsum zeta potential is close to zero [20].



**FIG. 3. DEPENDENCE OF INDUCTION PERIOD  $t_i$  ON INITIAL WATER TO GYPSUM RATIO  $x$ .**



**FIG. 4. DEPENDENCE OF SETTING TIME  $t_s$  ON INITIAL WATER TO GYPSUM RATIO  $x$ .**

Figure 3 presents the dependence of induction period on initial water to gypsum ratio  $x$  for the studied samples. Acceleration of the hydration process of hemihydrates caused by the presence of admixture in the case of low water to gypsum ratio  $x$  (the induction period is shorter) is observed.

In the case of higher water content ( $x > 0.67$ ) the induction period starts to be longer due to limited diffusion process of gypsum (ions) molecules leading to nucleation and crystallization.

Figure 4 shows setting time versus  $x$  ratio for the studied samples. The admixtures significantly influence the setting time interval of gypsum. They cause delay of the induction period and increase of the setting time (decreasing rate of hydration – for  $x > 0.67$ ).

### 3.2 Hydration/crystallization process

Reaction of gypsum powder – sulphate hemihydrate with water [9] is divided into three main stages and involves a set of coupled chemical processes in the gypsum – water system:

1. A nucleation period (occurring in induction time) starts after gypsum powder is mixed with water solvent. First, gypsum hemihydrate is dissolved in water. The dissolution involves detachment of molecular units from a solid surface in contact with water as well as diffusion and transport of solution components into paste volume. The solution becomes supersaturated with respect to  $\text{Ca}^{2+}$  and  $\text{SO}_4^{2-}$  ions which leads to the precipitation of solid grains (crystalline structure) – nucleation process.
2. An acceleration period in which complex reactions between ions or molecular compounds adsorbed on solid surfaces occur – hydration/crystallization process.
3. A deceleration period in which very slow adsorption and accumulation reactions of ions or other molecular units occur at an interface. The late stage of hydration is thus controlled by a diffusion process.



The rate of all the reactions can be changed if a third nonreactive material (polymer admixture) adheres to gypsum particles reducing their reactive surface or solution viscosity. For example, the induction period can be prolonged with [21]

- a) reduced diffusion of water and calcium ions at the gypsum surface because the adsorbed polymer (if so) hinders the process,
- b) formation of a complex between calcium ions and polymer,
- c) change in the growth kinetics and morphology of hydrated phases caused by the dispersive action of the polymer.

Experimental observations suggest that the rate of formation of gypsum hydration product is a rate-controlling process of hydration at early stages [22]. These observations lead to the development of hydration kinetics models based on nucleation and growth phenomena.

The simplest and most widely used equation proposed by Avrami [23] and independently by Johnson and Mehl [24] and Kolmogorov [25] is derived using the assumption within the transforming (from liquid to crystal) volume. The well known results are described by the Avrami equation as follows:

$$X(t) = 1 - \exp(-K t^n) \quad (1)$$

where:

$X(t)$  – is the volume fraction of crystalline phase that has transformed at time  $t$ ,

$K$  – is the combined rate constant that involves the rates of growth and nucleation,

$n$  – Parameter dependent on the mechanism of nucleation and dimensionality of growth.

If  $n \approx 1$ , the growth is one-dimensional (needle). When  $n \approx 2$  two dimensions are observed and at  $n \approx 3$  isotropic growth (sphere) appears. The authors [26] first applied the Avrami equation to  $C_3S$  hydration data and they reported an exponent value of  $n = 3$ . However, X-ray diffraction data resulted in a low value of  $n = 1$ . Similar values of  $n$  close to unity were reported more recently [27] from kinetic data obtained from the measurement of pore structure development. However, Thomas [28,29] showed that when the Avrami equation is applied to calorimetry rate data (limited to the rate peak), the value of  $n$  was 3.7 (the value close to 4 denoted a phase boundary control, three-dimensional growth and thermal nucleation).

The volume of the transformed phase will increase with the simple power law (Avrami equation) in the early stages of the process before adjacent regions of growing product are impinged. Thus overall growth rate in the system decreases with time.

It is commonly assumed that hydration is diffusion controlled by the rate at which the reactants can diffuse through the nanoporous layer of hydration product around the remaining unhydrated gypsum particles. The point in which the hydration process shifts away from nucleation and growth is not well established, but it is an important aspect of the hydration process.

The increasing use of mineral or polymer admixtures to gypsum materials leads to the question how the admixtures can affect hydration rate especially at early stages.

A wide range of properties, including heat of hydration phase, volume fraction, chemical shrinkage, percolation of capillary porosity and setting time, can be followed as hydration (and crystallization) proceeds.

Hydration/crystallization process of gypsum pure and with admixtures was studied using DSC. It is a direct way to monitor the extent of reactions by measuring the heat flow rate. Figure 5 shows DSC thermograms of 1. pure gypsum, 2. gypsum with 1% HEMC by weight, 3. gypsum with 1% PVAC by weight, at  $w/g$  ratio equal to 0.54. Gypsum hydration occurs in the main three-stage processes: nucleation, acceleration and deceleration. The crystallization process occurs faster in the case of sample 1 (without admixtures). The HEMC and PVAC admixtures cause a delay of the hydration/crystallization process due to a decrease of nucleation rates of the reaction products (lower value of  $\log K$ , Table 1).

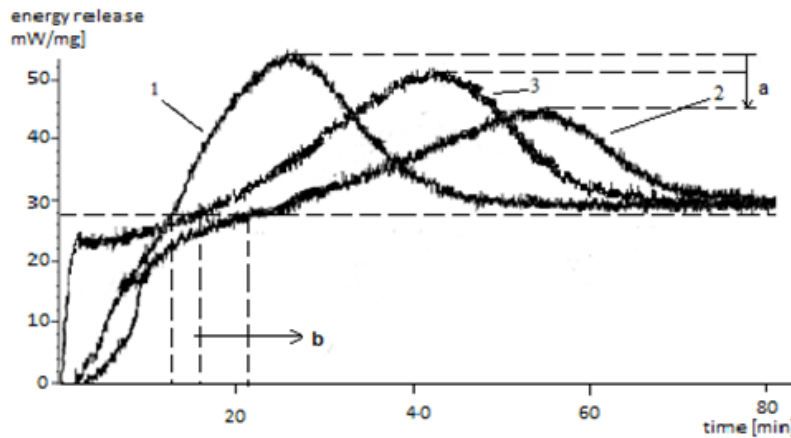


**FIG. 5. DSC THERMOGRAMS AT ISOTHERMAL CONDITIONS, T= 30°C FOR GYPSUM SAMPLES WITH X = 0.54. 1 – WITHOUT ADMIXTURES, 2 – WITH 1% HEMC, 3 – WITH 1% PVAC; A – INFLUENCE OF THE ADMIXTURE ON THE MAXIMUM HEAT RELEASE RATE; B – INFLUENCE OF THE ADMIXTURE ON THE ONSET OF HEAT RELEASE.**

**TABLE 1**

**log K AND n PARAMETERS OBTAINED USING THE AVRAMI EQUATION (DATA OBTAINED BY DSC ANALYSIS AND SETTING TESTS – ACCELERATION PROCESS).**

Sample	DSC x = 0.54		Setting x = 0.54	
	log K	n	log K	n
1.	-1.8	1.4	-3.4	1.3
2.	-2.6	1.4	-3.5	1.3
3.	-2.3	1.2	-3.6	1.4

In the case of calorimetric studies a volume fraction of increasing transforming phase X is taken (in Avrami plot) as a ratio of crystallization/hydration heats:

$$X = \Delta H_x / \Delta H_c \tag{2}$$

where

$\Delta H_x$  – part of heat released changing with time,

$\Delta H_c$  – total heat release.

The heat transformation data are fitted reasonably well to the Avrami equation.

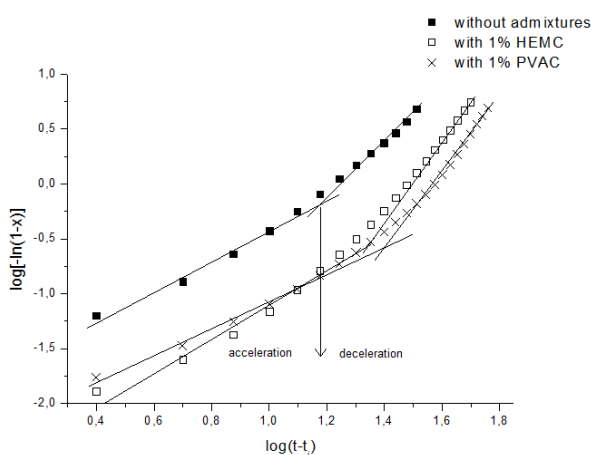


**FIG. 6. log[-ln(1-X)] versus log (t-t<sub>i</sub>) for x = 0.54.**

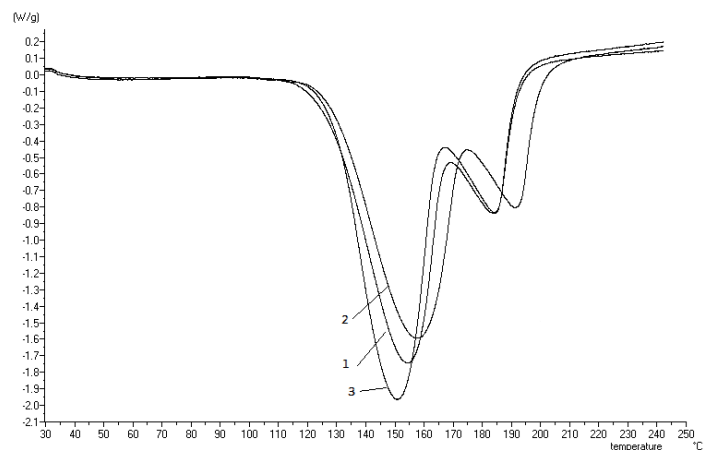


**FIG. 7. DSC THERMOGRAMS OF GYPSUM SAMPLES: pure (1) and with 1% admixtures of HEMC (2), PVAC (3) when x= 0.54 (β = 10°C/min).**

Figure 6 presents an example of Avrami plots in the double log form. It shows two regions of fitting, which can be caused by a complex chemical reaction of gypsum with water. The calculated parameters  $\log K$  and  $n$  of the equation are given in Table 1. The results indicate that the additives behave as efficient disturbing agents in the nucleation and crystallization process of gypsum – lower  $\log K$  value.

In respect to the presented study on setting time, the volume fraction of crystalline phase  $X$  in the Avrami plot is taken as the ratio:

$$X = h/h_{max} \quad (3)$$

where  $h$  and  $h_{max}$  are the height of needle changing with time of setting and maximum height at the end of the process, respectively (Figures 3 and 4).

Parameter  $n$  equal to 1.2 – 1.4 means that the crystallization process during hydration proceeds in nearly one direction. Parameter  $n$ , measured by two different methods (calorimetry and setting tests), shows similar values. The values of  $\log K$  are found to be smaller in the case of setting time experiments.

### 3.3 DSC analysis of set gypsum

After two hours of crystallization (hydration) at 30°C, the samples were heated from 30 to 250°C at heating rate  $\beta=10^\circ\text{C}/\text{min}$  in the DSC apparatus. Results in the form of thermograms are shown in Fig. 7.

The peaks in Fig. 7 denote the heat of bound water evaporation. The values of heat are shown in Table 2 together with corresponding peak temperatures  $T$ . The observed temperature range from 130°C to 200°C is associated with dehydration of gypsum by transition from dihydrate into hemihydrate.

TABLE 2  
THE VALUES OF  $dH_1$ ,  $dH_2$ ,  $T_1$ ,  $T_2$  OBTAINED FROM DSC ( $x=0.54$ ).

Sr	Sample	$dH_1$ [J/g]	$T_1$ [°C]	$dH_2$ [J/g]	$T_2$ [°C]
1	H <sub>2</sub> O with gypsum	187.0	153.9	38.5	185.7
2	H <sub>2</sub> O with gypsum and 1% HEMC	196.0	158.0	44.5	193.6
3	H <sub>2</sub> O with gypsum and 1% PVAC	219.0	150.6	46.7	186.9

$T_1$  – peak temperature of dehydration in the first step [°C] – bound water;  
 $T_2$  – peak temperature of dehydration in the second step – bound water [°C];  
 $dH_1$  – heat of dehydration in the first step [J/g] – for 1 g of sample;  
 $dH_2$  – heat of dehydration in the second step [J/g] – for 1 g of sample.

The bound water is divided into the adsorbed bound water (hygroscopic) where the layer of cations is strongly associated with solid particles to form hydrated crystals and weaker bounded water (by hydrogen bonds) called diffused water. The release temperatures are  $150.6 < T_1 < 158.0$  and  $185.7 < T_2 < 193.6$ , respectively (see Table 2).

No free water peak ( $\approx 100^\circ\text{C}$ ) is observed for low  $x$  (in the case of drying at room temperature for 24 h).

The heat of dehydration  $dH_1$ ,  $dH_2$  and temperatures  $T_1$ ,  $T_2$  can indicate the effects associated with the presence of the polymeric additive system. It was found (calculated) that the amount of water released from both aqueous states, i.e. hygroscopic and diffused, associated with the gypsum structure is proportional to the gypsum mass in the material, which increases with decreasing  $X$  (gypsum to water ratio), even in the case when a polymer is added. The average calculated values of heat absorbed during the dehydration – transformation of gypsum dihydrate to hemihydrate – associated with each of the states for pure gypsum, gypsum plaster with PVAC and gypsum plaster with HEMC are:  $dH_1=290.0$ ,  $271.0$  and  $269$  kJ/g; and  $dH_2=66.7$ ,  $63.8$  and  $56.2$  kJ/g, respectively (for 1 g of gypsum). The amount of heat consumed during dehydration of the adsorption state is about 17-19% of the total heat of bound water and it does not depend on the presence of the polymeric additives.

### 3.4 Results of mechanical tests

The results of mechanical tests are shown in Figures 8 and 9. The graphs present the dependence of flexural strength  $\sigma_{max}$  and E modulus on water to gypsum ratio  $x$ .

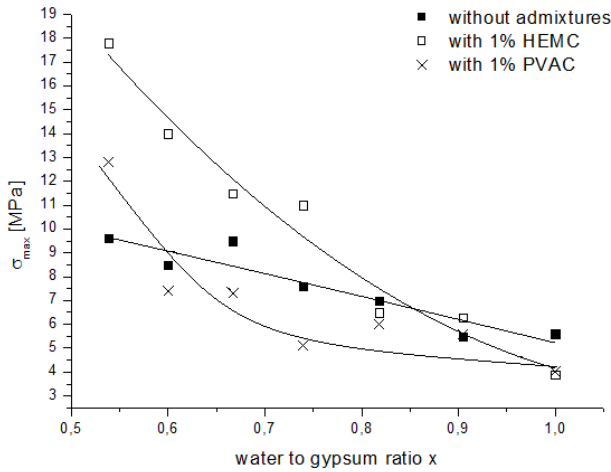


**FIG. 8. Bending flexural strength  $\sigma_{max}$  versus  $x$  (initial water to gypsum ratio). Bar error  $\Delta\sigma_{max}$  E1 MPa**

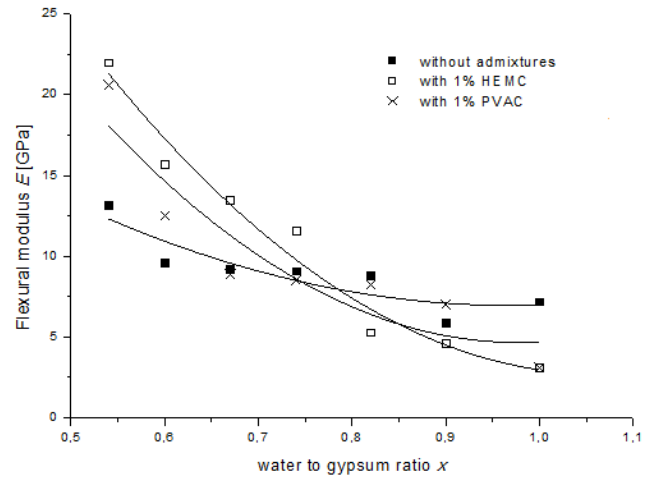


**FIG. 9. Dependence of flexural modulus  $E$  on  $x$  (initial water to gypsum ratio). Bar error  $\Delta E$  E2 GPa**

It can be seen that both flexural strength properties decrease with increasing water amount. This trend is observed for all samples being studied.

It can be seen that the influence of admixtures, such as HEMC or PVAC, on mechanical properties of gypsum is important merely for gypsum samples with low water content. Higher water content causes increased induction and setting times, while residual water acts as a plasticizer making larger pores in gypsum plaster.

The amount of bound water is almost the same in all tested samples (the differences are small), so that the amount of free water must be similar for the three discussed samples of the same  $x$ . Thus, porosity associated with the evaporation (free water release) should be the same. It is predicted that the polymers are deposited in the form of a film layer in the pore structure improving mechanical properties of gypsum. In the case of high  $x$  the decreasing values of modulus and flexural strengths are observed. Thus, there is a pronounced effect of the polymer on the mechanical properties for low  $x$  values. Assuming that with an increasing  $x$  value the sample porosity rises and taking into account the dependence of  $\sigma$  and  $E$  on porosity  $p$  proposed by [30], we have:

$$\sigma = \sigma_0 e^{-bp} \tag{4}$$

$$E = E_0 e^{-bp} \tag{5}$$

The values of  $\sigma_0$  and  $E_0$  are taken (equation 4 and 5) by approximation for  $x = 0.2$  – no porosity (at about 20% water is bounded), parameter  $b$  is characteristic for the material. The values of  $\sigma_0$  and  $E_0$  are much higher for gypsum plaster with the admixture applied.

The  $b$  parameter shows a difference in material properties – gypsum pores dependent on the polymer admixture.

The values of parameter  $b$  for 1: sample without admixtures, 2: sample with 1% HEMC, 3: sample with 1% PVAC obtained from flexural strength plots are equal to: 1.6, 2.7 and 2.2, respectively. Similar values were calculated from the plots of Young modulus.

#### IV. CONCLUSIONS

In this paper, the influence of selected polymers on gypsum properties, was studied by DSC, setting process and mechanical tests. The results indicate clear influence of such admixtures as HEMC or PVAC on gypsum properties, i.e. time and rate of setting, mechanical results (flexural strength and modulus), and crystallization kinetics. The setting and crystallization processes can be prolonged with reduced diffusion of water and calcium ions at the formed gypsum crystalline surface because polymer molecules in water solution hinder the process. It is predicted that the polymer film inside material pores is formed changing mechanical properties of the resulting gypsum material. Future work will be focused on the properties changing with the amount of admixtures (0.25-1.5%) and on morphological aspects of the prepared gypsum plasters.

The role of calcium sulphate anhydrate in hydration process is not discussed here.

#### ACKNOWLEDGEMENTS

The research was funded by the National Science Centre (OPUS 6) under project no. UMO-2013/11/B /ST8/04308.

#### REFERENCES

- [1] Crépy L., Petit J.Y., Wirquin E, Martin P, Joly N. Cement and Concrete Compounds 2014;45:29-38.
- [2] Etsuo S. Cement and Concrete Research 2006;36:2049-2053.
- [3] Martinelli E. Cement and Concrete Research 2013;40:48-58.
- [4] Jansen D., Neubauer J. Cement and Concrete Research 2012;42:327-332.
- [5] Peng J. Cement and Concrete Research 2005;35:527-553.
- [6] Pointot T., Bartholin M.C., Govin A., Grosseau P. Cement and Concrete Research 2015;70:50-59.
- [7] Yilmaz V.T., Glasser F.P. Advances in Chemistry Research 1989;7:111.
- [8] Garg M., Pundir A. Cement and Concrete Research 2014;45:227-233.
- [9] Bullard J.W. et al. Cement and Concrete Research 2011;41:1208-1223.
- [10] Singh N.B. Progress in Crystals Growth and Characterization of Materials 2007;53:57-77.
- [11] Tesárek P., Drchalová J., Kolísko J., Rovnaníková P., Černý R. Construction and Building Materials 2007;21:1500-1509.
- [12] Pourchez J. Cement and Concrete Research 2010;40:242-252.
- [13] Pourchez J. Cement and Concrete Research 2006;36:1777-1780.
- [14] Pourchez J. et al. Cement and Concrete Research 2006;36:288-294.
- [15] Plank J., Kainz J., Büllichen D. Cement and Concrete Research 2012;42:953-959.
- [16] Büllichen D., Plank J. Cement and Concrete Research 2013;46:66-72.
- [17] Brumaud C. et al. Cement and Concrete Research 2013;53:176-184.
- [18] Bojadjieva C., Glavchev I. Cement and Concrete Research 2004;34:611-613.
- [19] Toxqui-López S., Olivares-Pérez A., Fuentes-Tapia I. Optical Materials 2006;28:342-349.
- [20] Plank J., Hirsch Ch. Cement and Concrete Research 2007;37:537-542.
- [21] Kiesewetter et al. Cement and Concrete Composites 2014;53:25-34.
- [22] Thomas J.J., Biernacki J.J., Bullard J.W., Bishnoi S., Dolado J.S., Scherer G.W., Luttage A. Cement and Concrete Research 2011;41:1257-1258.
- [23] Avrami M. Journal of Chemical Physics 1939;7:1103-1112 and 1940;7:1212-1124.
- [24] Johnson W.A., Mehl R.F. Transactions of the American Institute of Mining and Metallurgical Engineers 1939;135:416.
- [25] Kolmogorov A.N. Bulletin of the Russian Academy of Sciences: Physics 1937;255.
- [26] Ridi F., Dei L., Fratini E., Chen S.-H., Baglioni P. Journal of Physical Chemistry 2003; 107:1056-1061.
- [27] Jansen D., Goetz-Neunhoffer F. Cement and Concrete Research 2013;35:71-77.
- [28] Damasceni A., Dei L., Fratini E., Ridi F., Chen S.H., Baglioni P. Journal of Physical Chemistry 2002;106:11572-11578.
- [29] Thomas J.J. Journal of the American Ceramic Society 2007;90:3282-3288.
- [30] Colak A. Material Letters 2006;60:1977-1982.

# A new novel crosslinker with space structure for low-polymer-loading fracturing fluid

Yuan Qing<sup>1</sup>, Li Fengguang<sup>2</sup>, Bi Yanxia<sup>3</sup>, Niu Zengqian<sup>4</sup>, Li Shiheng<sup>5</sup>, Cai Jingchao<sup>6</sup>,  
Tan Rui<sup>7</sup>, Lu Wei<sup>8</sup>, Chang Qing<sup>9</sup>, Chen Deyu<sup>10</sup>

<sup>1,2,3,4,6,7,8,9,10</sup>Engineering Technology Research Institute, CNPC Bohai Drilling Engineering CO., Ltd., Tianjin, Tanggu  
300457, China

<sup>5</sup>Oil & Gas Cooperation and Development Company, CNPC Bohai Drilling Engineering CO., Ltd., Tianjin, Dagang 300280,  
China

**Abstract**— Boron-based crosslinkers are used commonly to increase viscosity and to improve fluid-loss control and proppant transportability of guar and its derivative fluids. Boron crosslinkers are usually preferred because of their ability to reheel after shearing and their favorable environmental properties. In order to reduce both the formation and the proppant-pack damage from polymer residues and to reduce over-all fluid cost, more-efficient crosslinkers capable of crosslinking fluids with reduced polymer loading is of great interest. Previous studies demonstrated that polymer solutions have critical overlap concentration ( $C^*$ ), below which no intermolecular crosslinking leading to increased viscosity can occur. However, recent studies demonstrated that increased crosslinker size or length can lead to the crosslinking of polymer solutions well lower than the  $C^*$  and can reduce polymer loading without compromising the rheology of the fracturing fluid.

This paper shows the effect of new crosslinkers with space structure capable of interacting with multiple poly-saccharide strands to form crosslinking networks at lower polymer loadings than conventional guar fluids. The crosslinker is formed by the reaction of boric acid and a Polyamine with six-member ring to improve the spatial structure. The formation procedures of the new crosslinker by Boric and six-member Polyamine is very simple, and the synthetic condition is also very mild. The concentration of guar fluid with this new crosslinkers can be reduced by 30%. In addition, the crosslinker reacted with glucose to improve the control of the fluid-viscosity buildup can make the product fit into broader applications. The time of the fluid-viscosity buildup ranges from 15 to 180s. The pH value is very important to the heat resistance characteristics of the fracturing liquid system, the heat resistance characteristics increase with the increase NaOH loading. The polymer residual of the new fracturing system with new crosslinkers is much lower than that with conventional crosslinkers because of the low polymer loading. The cost of new crosslinkers is low because of the low price of raw material and the simple formation procedure and the mild synthetic condition, which is very important for extensive used in the oil field.

**Keywords**— Cross linker Boric acid, Polyamine space structure.

## I. INTRODUCTION

Wells drilled into low-permeability reservoir need to be treated with hydraulic fracturing to increase the conductivity and thereby to obtain the economic production. Hydraulic-fracturing cracks in the zone are created by forcing a fluid at a pressure higher than the parting pressure of the rock. The fractures expanded as the continued injection of fracturing liquid with proppants. When the predetermined amount of liquid is injected into the formation, the pressure in the surface is released, and the fracturing gel will break and retreat from the formation to the surface leaving the proppants in the fractures to inhibit the fractures from closing. The viscosity of the fluid is typically generated by polymers, such as polysaccharides and its derivatives. Hydrated guar and derivatives create linear gels that do not achieve the required viscosity for proppant transport at elevated temperatures <sup>[1]</sup>. Thus, crosslinkers, such as boron, zirconium or titanium compounds, are used to significantly increase the viscosity of the fluid system. Boron-Based crosslinkers are used to increase viscosity, fluid-loss control and proppant transportability of guar fluid. Boron crosslinkers can reheel after shearing, so they are used very commonly in the oil field. Guar gum contain protein species, insoluble even after the breaking of the fluid that is damaging to the formation, so that less polymer usage will result in less damage to the subsurface formation. More efficient crosslinkers capable of crosslinking fluids with reduced polymer loading have always been of great interest to reduce formation and proppant pack damage from polymer residues, and to reduce overall fluid cost <sup>[1]</sup>.

The lower polymer loadings can be realized by several ways: firstly, the processed enhanced guar can be used to reduce the guar loadings, for example, Dawson et al. [4] developed a new generation of guar that yields high crosslinked fluid viscosity at reduced loadings. Cramer and Woo [5] utilized processed enhanced guar crosslinked with borate at a reduced polymer loading and applied the borate crosslinked PEG for treatment of several wells in the Monument Butte area. Secondly, Dawson et al. [2] and Clark [3] demonstrated that polymer solution have critical overlap concentration, below which no intermolecular crosslinking leading to increased viscosity can occur. However, Sun and Qu [1] demonstrated that increased crosslinker size or length can lead to the crosslinking of polymer solutions well lower than  $C^*$  and can reduce polymer loading without compromising the rheology of the fracturing liquid, at the same time, they reported the synthesis of polyaminoboronates (PAB), bulky compounds containing multiple boron sites and capable of interacting with multiple polysaccharide strands to form more complex crosslinking networks at lower polymer loadings than conventional guar fluids. The PAB was successfully used in two wells in green River sandstone formations of the Uintah Basin In 2014 [6]; Lu Yongjun et al. [7] formed a new novel crosslinker by sodium borate and salt of organic acid, such as sodium gluconate, sodium lactate; Xue Xiaojia et al. [8] formed a novel crosslinker including borate, NaOH, sodium carbonate, Benzene boron cyclic compound, with the new crosslinker, the guar loading can decrease more than by 25% than conventional fracturing liquid system; Sui Mingwei [9] formed a new crosslinker with raw materials of sodium tetraborate decahydrate, glucose. The amount of crosslinking agent was used to crosslink 0.2% guar glue solution is 1.2%-1.6%. Temperature tolerance can be as high as 80°C. Thirdly, the thermal enhanced agent can also used to decrease the guar loading, for example, Du et al. [10] used organic bases, including triethanolamine, ethanediamine, as the thermal enhanced agent to form a fracturing liquid with low guar loadings.

However, the raw material of novel crosslinker in the literatures of Sun and Qu [1] is very expensive, so the cost down by the low guar loading is offset by the higher cost of the crosslinker. A lower-cost combination of raw materials is sought in order to improve the marketable acceptance of the product. In this work, the tripolycyanamide is used to replace the tetraethylenepentamine (TEPA) as the base scaffold, which has two merits: firstly, tripolycyanamide is much cheaper than TEPA; secondly, the tripolycyanamide has better spatial outstretched capacity than TEPA.

## II. EXPERIMENTAL PROCEDURES

Approximately 150ml of alcohol and 100ml of water were added into a 500-cm<sup>3</sup>, three-necked, round-bottomed flask equipped with a thermometer and a Dean-Stark adaptor equipped with a reflux condenser; 50 g of boric acid was added to the flask and heated for five minutes. And then 50g of tripolycyanamide was added to the flask. The reaction mixture was then heated at 90 °C for 4h. 90g of glucose was added and heated for 1 hour in order to obtain the delay properties. 10g of NaOH is added and stirred until the NaOH dissolved completely. A white liquid was obtained as the final solution.

## III. RESULTS AND DISCUSSION

### 3.1 Pick-up time

The crosslinking performances of two new type crosslinkers are evaluated by the time that fracturing liquid can be picked up by the glass rod. 0.3g hydroxypropyl guar gum was added in 100 ml water, and stirred for 20 min to make sure that the guar gum was swelling sufficiently. And then NaOH solution and crosslinker were weighted into the guar gum solution, respectively. The solution was stirred with the glass rod until the solution can be picked up, the time from the injection of the crosslinker into the solution to the solution can be picked up is the pick-up time. The pick-up time usually depends on the NaOH, the crosslinker, and polymer loadings.

The experimental results were shown in Table 1. The pick-up time of crosslinkers without glucose in 0.3% guar gum, at 10wt% NaOH solution loadings of 0.1-0.6ml, was in the range of 15 to 40 seconds. However, the pick-up time of crosslinkers with glucose in the same condition was in the range of 25 to 150 seconds. The glucose can extend the pick-up time, a logical explanation for this observation is that the reaction between glucose and hydroxides of crosslinker effectively blocks the borate sites of the crosslinker, resulting in improved pick-up closure. It can be seen from table 1 that the NaOH has a higher influence on crosslinker with glucose than that without glucose. The pick-up time decreased with the increase of crosslinker loadings, which is because that higher crosslinker loading will result in more crosslinking points density and then increase the crosslinking rate.

**TABLE 1**  
**SUMMARY OF PICK-UP TIME FOR GUAR LINEAR GEL CONTAINING DIFFERENT NaOH AND CROSSLINKER LOADINGS AT ROOM TEMPERATURE**

Crosslinker	Guar Loading (g)	NaOH Loading (ml)	Crosslinker Loading (g)	Pick-up Time (s)
Without glucose	0.3	0.1	0.3	15
Without glucose	0.3	0.3	0.3	25
Without glucose	0.3	0.6	0.3	40
Without glucose	0.3	0.3	0.4	32
Without glucose	0.3	0.3	0.5	22
With glucose	0.3	0.1	0.3	48
With glucose	0.3	0.3	0.3	90
With glucose	0.3	0.6	0.3	150
With glucose	0.3	0.3	0.4	76
With glucose	0.3	0.3	0.5	47

### 3.2 Sand-Carrying Capacity of Crosslinked Fluid

About 90 ml of hydrated guar fluid were mixed with 20 ml of 20/40 sand, buffered and crosslinked with novel crosslinker while stirring. The sand crosslinked fluid suspension was poured into 100 mL graduated cylinders. Picture was taken at 40 min after the sample was placed on the table. Illustrated in fig. 1 is the sand settling test picture for 0.4 wt% borate-crosslinked guar gel contained 20 wt% of 20/40 sand. After 40 min, sand settling level was at 97mL from initial 110ml, which illustrated that the gel has a good sand-carrying capacity.

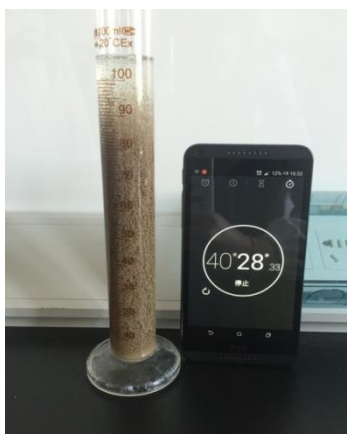


**FIG. 1 SAND SETTLING TEST OF NEW NOVEL BORATE-CROSSLINKED GUAR GEL CONTAINED 20 WT% OF 20/40 SAND AT ROOM TEMPERATURE. A 0.3WT% GUAR LOADING IN FRESH WATER WAS ADDED INTO 0.4ML NaOH (10%) AND CROSSLINKED WITH 0.4 ML NOVEL CROSSLINKER.**

### 3.3 Rheology

The compounds were evaluated as crosslinkers in guar fluids on HAAKE RS6000 rotary rheometer, by placing 50 ml of gel in the Fann 50 cup and positioning the cup on the rheometer. The sample was sheared at a preconditioned and constant shear rate of 170 sec<sup>-1</sup> for 65 minutes. The fluid was heated to the experimental temperature at the rate less than 3.2 °C/min. When the final viscosity of the liquid is larger than 50 mPa·s, the crosslinker is eligible at this temperature and guar loading. The influence of NaOH and guar loading on the thermal endurance was evaluated in the experiments. The rheology profile of the liquid with 0.2wt% and 0.3wt% guar loading are shown in fig.2 to fig.3, respectively, with the same loading of 0.4wt% NaOH solution, 0.4 wt% crosslinker. Illustrated in fig.2 is the rheology profiles of borate-crosslinked gel at the temperature of 40, 60, 80□, respectively, with 0.2wt% guar loading. It can be seen that the final viscosity of the liquid with new crosslinker is 155 and 78 mPa·s at the temperature of 40 and 60 □, respectively, and is larger than 50 mPa·s for 40 min. Illustrated in fig. 3 are the rheology profiles of borate-crosslinked gel at the temperature of 100, 120□, respectively, with 0.3wt% guar loading. It can be seen that the final viscosity of the liquid with new crosslinker is 100 and 65 mPa·s at the temperature of 100 and 120 □, respectively. With the new novel crosslinker, the guar loading can be reduced by 30% than conventional crosslinker, while the cost of crosslinker does not increase.



During the gel was injected into the oil reservoir, the gel would go through the pump and the shot hole, the gel will endure intense shear, so the gel need good rehaul gel ability to transport proppant after shearing. In this work, the rehaul ability of the gen crosslinked with novel crosslinker is measured. The cup is filled with gel and the sample was sheared at 170 sec-1, the rate of temperature increase is controlled in  $3.0 \pm 0.2$  until the experimental temperature ( $\pm 0.2$ ), and keep this temperature in the whole experimental progress. The changed shear rate experiment was started when the temperature kept for 20 minutes. The progress includes two stages, firstly shear rate decrease from 170 sec-1 to 0 sec-1, and then increase from 0 sec-1 to 170 sec-1. Each stage was kept for 15 sec. Illustrated in fig. 3 are the rheology profiles of gel at the temperature of 120, with 0.4wt% guar loading in fresh water and added into 0.4ml NaOH (10%) and crosslinked with 0.4 ml novel crosslinker. It can be seen from the fig. 4 that the viscosity of the gel can maintain the primary viscosity after the shear rate return to the 170 sec-1, which means the gel crosslinked with new crosslinker has good shear rehaul ability.

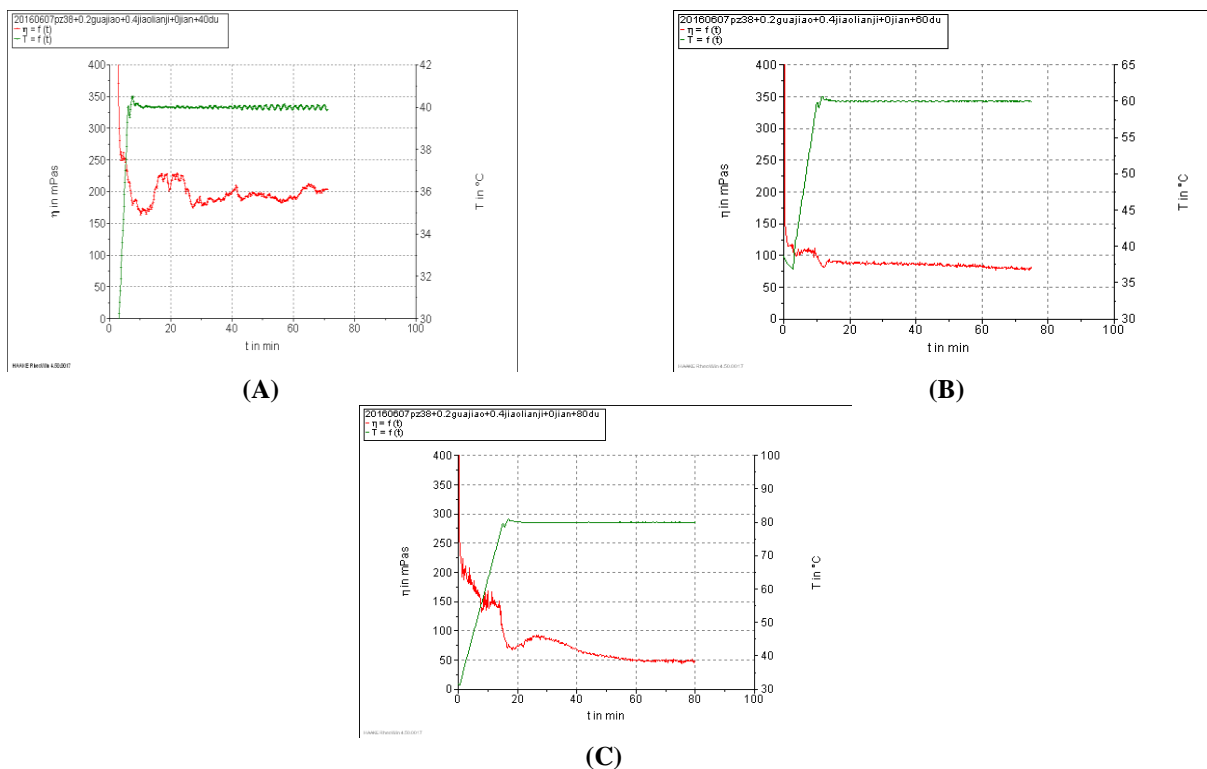


**FIG. 2 RHEOLOGY PROFILE OF THREE SAMPLE OF NEW NOVEL BORATE-CROSSLINKED FLUID AT DIFFERENT TEMPERATURE OF 40 °C (a), 60 °C (b) and 80 °C (c), RESPECTIVELY. A 0.2wt% GUAR LOADING IN FRESH WATER WAS ADDED INTO 0.4ML NaOH (10%) AND CROSSLINKED WITH 0.4 ml NOVEL CROSSLINKER.**

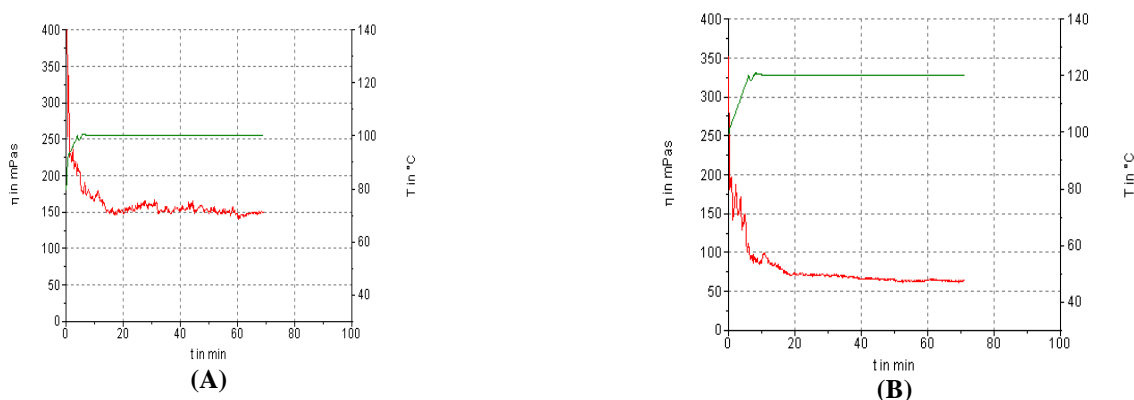


**FIG. 3 RHEOLOGY PROFILE OF THREE SAMPLE OF NEW NOVEL BORATE-CROSSLINKED FLUID AT DIFFERENT TEMPERATURE OF 100 °C (a), 120 °C (b), RESPECTIVELY. A 0.3wt% GUAR LOADING IN FRESH WATER WAS ADDED INTO 0.4ml NaOH (10%) AND CROSSLINKED WITH 0.4 ml NOVEL CROSSLINKER.**

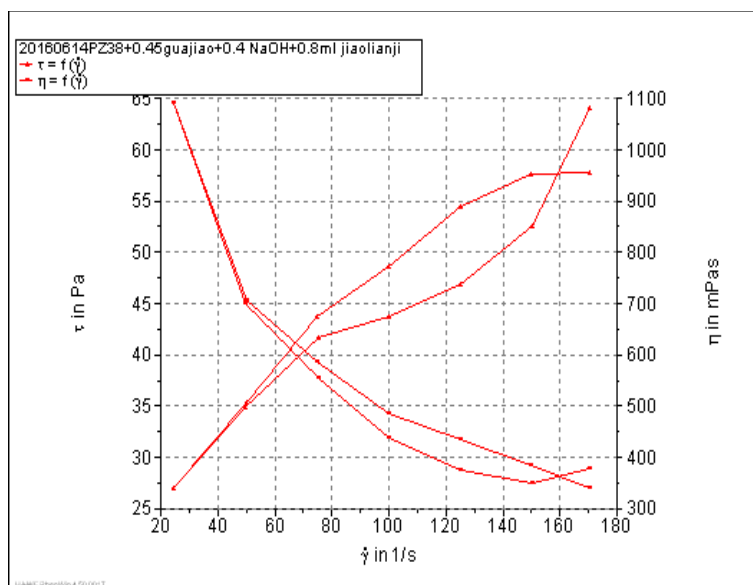


**FIG. 4 RHEOLOGY PROFILE OF A SAMPLE WITH CHANGED SHARE RATE FROM 170 sec-1 to 0 sec-1 AND THEN FROM 0 sec-1 to 170 sec-1. A 0.4wt% GUAR LOADING IN FRESH WATER WAS ADDED INTO 0.4ml NaOH (10%) and CROSSLINKED WITH 0.4 ml NOVEL CROSSLINKER.**

### 3.4 Gel breaking and residue of the gel residual

0.3 wt% guar loading in fresh water was stirring for 20 min to make sure that the guar was swelled absolutely, which is called base fluid. While the fluid is stirring, the crosslinker and gel breaker are added into the base fluid until the gel can be picked up and avoid forming bubbles. The fracturing liquid is filled into closed container and putted into the thermostatic waterbath of 60°C for 4 h. After the gel breaks, the viscosity of supernatant liquor is measured. The breaking gel is filtered by the filter paper, and measured the residual of the breaking gel. Fig. 5 shows the sample pictures of fracture liquid after breaking with different ammonium persulphate loading of 0.02 wt%, 0.03wt%, 0.04wt% and 0.05wt%, respectively. It can be seen from fig. 5 that the gel can break at the four breaker loading. The viscosity of supernatant liquor is less than 5 mPa.s. The residual of the gel is 170 mg/L.



**FIG. 5 SAMPLE PICTURES OF FRACTURE LIQUID AFTER BREAKING WITH DIFFERENT AMMONIUM PERSULPHATE LOADING OF 0.02 wt%, 0.03wt%, 0.04wt% and 0.05wt%, RESPECTIVELY.**

### 3.5 Liquid loss

Two pieces of filter paper and the sample were filled into the filter cartridge, respectively. The measure cup was putted into the heating jacket. The filter cartridge was pressured with the initial pressure and heated to the experimental temperature in 30 min. After that, the filter liquor will filter out under the differential pressure of 3.5 MPa. The amount of filter liquor within 36 min is collected and measured. The experiment results is shown in table 2, it can be seen that the filtration property of the new liquid system is very similar to the conventional liquid system, and much lower than the standard value in the criterion. The results indicate the formation of a good filter cake by new crosslinked fluid, minimizing potential fluid loss to the formation.

**TABLE 2**  
**EXPERIMENTAL FILTRATION PROPERTY RESULTS OF DIFFERENT FRACTURE LIQUID SYSTEM**

	Fracture fluid with new crosslinker (0.28% guar gram)	Conventional fluid system (0.45% guar gram)	Standard value in the criterion
Filtrate loss coefficient, $m^3/m^2$	$0.5 \times 10^{-4}$	$0.46 \times 10^{-4}$	$6 \times 10^{-4}$
Spurt loss amount, $m^3/m$	$0.35 \times 10^{-3}$	$0.35 \times 10^{-3}$	$1 \times 10^{-3}$
filtration rate, $m/min$	$0.085 \times 10^{-4}$	$0.076 \times 10^{-4}$	$1 \times 10^{-4}$

### 3.6 Field Application

The new crosslinker was used in a vertical well in Sulige gas field of Ordos Basin. The geothermal gradient of this well is  $3.06^\circ/100m$ , and the temperature of target stratum is  $108^\circ$ . The formula of the fracturing system is composed of 0.28% Hydroxypropylguar gum, 0.3% antishwelling agent, 0.5% cleanup additive, 1.0% potassium chloride, 0.35% sodium carbonate and water. The dosage of the crosslinker is 0.3% of the fracturing liquid system. The closure stress of stratum is 50 MPa, so the proppant with medium volume density of  $1.75g/cm^3$  is selected, which diameter is between 0.425 mm and 0.85mm.

The well depth of the target stratum is between 3649.3-3652.4m, the operating pressure is 37.7-42.1MPa, the cracking pressure is 39.1MPa, the injection rate of fracture liquid is 3.5-3.9m<sup>3</sup>/min, the volume of liquid nitrogen is 6 m<sup>3</sup>, the volume of sand is 15 m<sup>3</sup>, the largest sand proportion is 18.5%. The total volume of injection liquid is 205 m<sup>3</sup>. The operation curve is shown in fig 6. With the new novel crosslinker large-scale applications, the dosage of the guar gram decreased from 0.45% to 0.28%, which will protect reservoir and induce huge economic benefit.

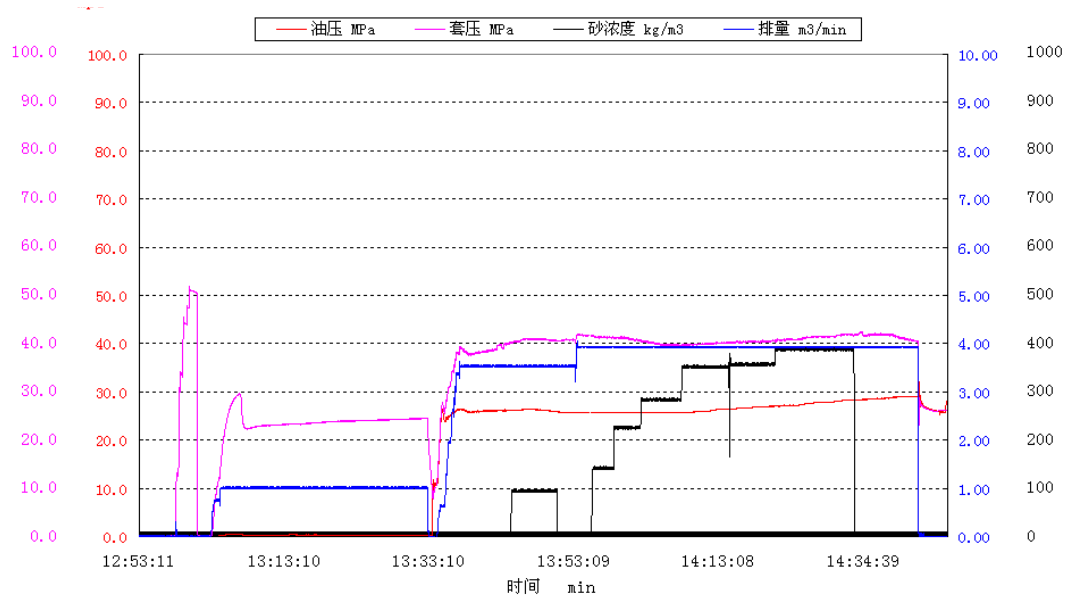


**FIG 6 THE OPERATION PRESSURE CURVE IN A VERTICAL WELL IN SULIGE GAS FIELD OF ORDOS BASIN WITH NEW CROSSLINKER FRACTURE FLUID.**

## IV. CONCLUSION

A new chemistry was developed on the basis of the condensation reaction of boric acid with a polyamine scaffold of tripolycyanamide to yield a polyaminoboronate crosslinker with multiple boron sites. The molecular size of new crosslinker enables crosslinking guar or its derivatives at lower concentration, thus reducing the loading of polymer required. New chemistry was developed in which glucose was incorporated into the crosslinker to delay the crosslink rate at the boronate sites. The NaOH has a great influence on the crosslink rate and thermal endurance, at the same time, the pick-up time increase with the increase of crosslinker loading. With the new chemistry, the fracturing gel can endure  $120^\circ C$  with 0.3wt%

guar loading, which is lower than conventional guar loading by 30%. The new novel crosslinker also has good performance of gel breaking, gel residuals and fluid loss.

### REFERENCES

- [1] Sun, H. and Qu, Q. 2011. High-Efficiency Boron Crosslinkers for Low-Polymer Fracturing Fluids. Paper SPE 140817 presented at the 2011 International Symposium on Oilfield Chemistry, The Woodlands, Texas, 11-13 April. <http://dx.doi.org/10.2118/140817-MS>.
- [2] Dawson, J.C., Le, H.V., and Kesavan, S. 2000. Polymer Expansion for Oil and Gas Recovery. US Patent No. 6,017,855.
- [3] Lei, C. and Clark, P.E. 2004. Crosslinking of Guar and Guar Derivatives. Paper SPE 90840 first presented at the 2004 SPE Annual Technical Conference and Exhibition, Houston, Texas, 26\_29 September, and peer-approved 31 May 2007. <http://dx.doi.org/10.2118/90840-MS>.
- [4] Dawson, J.C., Cramer, D.C., Le, H.V. (2004) Reduced Polymer Based Fracturing Fluid: Is Less Really More?, paper SPE 90851 presented at the Annual Technical conference and Exhibition held in Houston, Texas, 26-29 September, 2004.
- [5] Cramer, D.D., and Woo, G.T. (2004) Development and Implementation of a Low-Polymer-Crosslinked Fracturing Fluid for Low-Temperature Applications, paper SPE 91418 presented at the Eastern Regional Meeting held in Charleston, WV, 15-17 September, 2004.
- [6] Magnus Legemah, Frances Debenedictis, Nigatu Workenh, David Smith, Hoang Le, Hong Sun, Qu Qi, Baker Hughes, Mickey Moulton, 2014. Successful Treatment of a Green River Sandstone Formation Using a Novel Low-Polymer Crosslinked Fluid. SPE 168186.
- [7] Lu Yongjun, Wang Liwei, Cheng Xingsheng, Guan Baoshan, Liu Ping, Cui Weixiang, Cui Mingyue, Liu Yuting, Zhai Wen. Crosslinker used in ultra low hydroxypropylguar gum loading fracturing liquid and corresponding fracturing liquid. China Patent No. 102732244 A.
- [8] Xue Xiaojia, Mu Lijun, Zhao Zhenfeng, Li Xianwen, Liu Jing, Zhao Wen, Ding Li, Tang Meirong, Lv Haiyan, Lv Baoqiang, Wu Jing, Bi Weiyu, Fan Huabo. High efficiency crosslinker to decrease guar loadings and its preparation method. China Patent NO. 102775979.
- [9] Sui Mingwei. Preparation of low-concentration guar gum fracturing fluid crosslinker and study on their laboratory evaluation. 2012, Shanxi University of Science and Technology, Master Thesis.
- [10] Du Biao, Yang Haiyan, Zhao Wen, Ding Li, Wan Hua, Yang Jigang, Zhao Yanhong, Lv Junhua, Ye Zhi, Hu Pengfei, Dou Miao, Li Peng, Lv Baoqiang, Guo Jun, An HengWen, Cheng Fang. Ultra-low polymer loading fracturing liquid and its preparation method. China Patent No. 102329602 A.

# ECC-based User Authentication Scheme for Wireless Sensor Networks

Imanbaev Temirlan<sup>1</sup>, Yue Li<sup>2</sup>

School of Computer Science and Technology, Donghua University, No. 2999 North Renmin Road, Songjiang, Shanghai 201620, China

**Abstract**— In 2016, Akansha S. et al. proposed an upgraded user authentication protocol. According to the implemented cryptanalysis on their scheme, some vulnerabilities have been found in registration and authentication part. In registration part, the gateway uses generated value as secrecy and sends it to sensor node, which doesn't have information about received secret value and cannot verify its identity. In authentication part, user is unable to check legitimacy of received session key generated by sensor node. Mainly, the protocol has been implemented using only one way hash function, XOR and concatenation operations, which is not adequate to provide authentication and confidentiality. In this paper, we suggest ECC-based user authentication scheme for WSNs, which eliminates the drawbacks of the previous scheme. The protocol decreases the high cost public-key operations of the sensor node and substitutes them with symmetric-key based operations.

**Keywords**— Authentication, Cryptography, Key agreement, Network security, WSN.

## I. INTRODUCTION

Nowadays, the Wireless Sensor Networks becomes a rich sphere of active research containing programming models, distributed algorithms, routing protocols, signal processing, system design, data management and security. For most of the WSN's applications, security is a major concern. Therefore, the resource constraint and computational limitations compels security solutions in WSNs to be differ from standard networks [1]. Sensor nodes are limited in terms of consuming power, energy levels and memory size. Thus, comparing with wired sensors, the nodes in WSNs have a vulnerability to various passive and active attacks. It makes security to be an essential factor for WSNs, where data integrity is the most important requirement. Authentication has three major classes based on the primary cryptographic methods such as asymmetric cryptography, symmetric cryptography and hybrid methods [2]. Initially, it was estimated that WSNs would compose only of equal sensor nodes. But nowadays we are discussing heterogeneous WSNs since sensor networks can be constructed with different kind of nodes, some of them equipped with better computational power comparing with others (e.g. gateway nodes) [3]. The main security requirements for WSNs are authentication, confidentiality, integrity, authorization, non-repudiation, availability and freshness. User identification can be performed using three factors such as physical attributes (for instance fingerprint, retinal pattern etc.), documents and credentials (like smart card, id card etc.), personal information or password [4].

In our work, we clearly show that Akansha S. et al.'s [5] user authentication scheme has some drawbacks, which does not provide resistance against some attacks and is not enough secure. Also, we demonstrate that their scheme can be made much efficient by using ECC and removing some unnecessary steps. To eliminate the weaknesses and improve previous work, we suggest ECC-based user authentication scheme for wireless sensor networks which is more secure as compared to previous work.

The remainder of this paper is arranged as follows. Section 2 describes related works. Section 3 contains a brief review of Akansha et al.'s scheme. The weaknesses of Akansha et al.'s scheme are described in Section 4. In Section 5, some preliminaries and network model are reviewed. Section 6 represents our key agreement protocol. The security of the proposed protocol is discussed in Section 7. We provide our research conclusions in Section 8.

## II. RELATED WORK

In this section, we have analyzed some of the related schemes which are proposed in the literature. In 2006, Wong et al. [6] presented his lightweight authentication scheme. But, it has been discovered that their scheme has several weaknesses against such attacks as forgery, replay and stolen-verifier attack. In 2009, Das et al. [7] improved Wong et al.'s scheme and proposed a two-factor secure authentication protocol for WSNs. Later Das et al.'s scheme was upgraded by some researchers. He et al. [8] proved that Das et al. protocol has some security pitfalls of impersonation attack since it doesn't provide easy password update facility. They offered an improved two-factor hash function protocol, which requires just three message

exchanges for user authentication. Chen et al. [9] also highlighted that Das et al. pro-tocol is not provided by mutual authentication between the gateway and sensor node. In 2010, Khan and Alghathbar [10] offered some enhancements in Das et al.'s scheme. They used password's hash value to get a high password security and pulled out a new idea of pre-shared keys between sensor nodes and the gateway. In 2011, Yeh et al. [11] mentioned that Chen et al.'s scheme doesn't provide easy password update phase, has no resistance against insider attack and suggested an ECC-based user authentication scheme.

In 2013 Shi et al. [12] presented a new user authentication protocol, which eliminates the vulnerability of Yeh et al.'s protocol and which is more efficient in terms of communication, security and computation cost. In 2014, Choi et al. [13] highlighted that Shi et al.'s scheme is sensitive to some security flaws such as stolen smart card attacks, sensor node energy exhausting attack and session key attack. Later, Anup K.M. et al. [4] pointed out several weaknesses in Choi et al.'s scheme. During the analysis, they discovered that the proposed scheme is vulnerable against stolen smart card attack, insecure to sensor node energy exhausting attack and doesn't provide resistance against node capture attack. Afterward, Turkanovic et al. [3] suggested a scheme for mutual authentication, which was discovered as non-secure protocol with many issues by Akansha S. et al.'s. They mentioned that the proposed scheme is not secure against session key recovery attack, reply attack, impersonate attack and offline password guessing attack.

### III. REVIEW OF AKANSHA S. ET AL.'S SCHEME

In this section, we did a short review for the Akansha S. et al.'s user authentication protocol. Their scheme contains three entities: the user, the sensor node and the gateway. For Akansha S. et al.'s scheme, there are three phases: registration phase, login phase, authentication and password changing phase.

**TABLE 1**  
**NOTATIONS**

Symbol	Definition
$U_i$	User
SC	Smart card
$S_j$	$j_{th}$ Sensor Node
$ID_i$	$i_{th}$ User's identity
$ID_{s_j}$	$j_{th}$ Sensor node's identity
$PW_i$	$i_{th}$ User's password
$PW_{s_j}$	$j_{th}$ Sensor node's password
GW	Gateway
$K_{GW}$	Secure password known only to Gateway Node
$K_{GW-u}$	Gateway's secret password key shared with the user $U_i$
$K_{GW-s}$	Gateway's secret password key shared with the sensor node j
T	Timestamp
SK	Separately computed session key with private information of both user and sensor node
$\oplus,   , h(.)$	XOR, concatenation, lightweight one way hash function

Initially, each user and sensor node has their own identities ( $ID_i, ID_{s_j}$ ) and secret passwords ( $PW_i, PW_{s_j}$ ). The gateway has both entities' identity and password. From the beginning, gateway creates a random key  $K_{GW-u}$  and  $K_{GW-s}$  to establish secrecy with user and sensor node.

### 3.1 Registration Phase

#### 3.1.1 Registration between $U_i$ and GW

The user  $U_i$  computes  $P_i = h(r_i \parallel h(PW_i))$  with generated random number  $r_i$  and sends message  $\{P_i, ID_i, T_{s1}\}$  to the GW, which checks the validity of timestamp  $|T_{s1} - T_c| < ||\Delta T$  and computes:  $a_i = h(K_{GW-U} \parallel ID_i)$ ,  $b_i = a_i \oplus h(P_i \parallel h(PW_i))$ ,  $c_i = h(a_i \parallel h(PW_i) \parallel ID_i)$ . The GW personalizes SC with values  $\{h(\cdot), b_i, c_i, ID_i\}$  and sends through secure channel to  $U_i$ , who computes an additional value  $d_i = r_i \oplus h(ID_i \parallel PW_i)$  and inputs value  $\{h(\cdot), b_i, c_i, d_i, ID_i\}$  into SC.

#### 3.1.2 Registration between GW and $S_j$

The sensor node  $S_j$  computes  $P_{sj} = h(ID_{sj} \parallel h(PW_{sj}) \parallel T_{s2})$  and sends message  $\{P_{sj}, ID_{sj}, T_{s2}\}$  to the GW, which checks the validity of timestamp  $|T_{s2} - T_c| < ||\Delta T$  and checks a satisfaction of computed  $P_{sj}^*$  with  $P_{sj}$ . If it satisfies the condition, then GW computes the next values using  $K_{GW-S}$ :  $\beta_j = h(K_{GW-S} \parallel ID_{sj})$ ,  $b_{sj} = \beta_j \oplus h(ID_{sj} \parallel h(PW_{sj}))$ ,  $c_{sj} = h(\beta_j \parallel h(PW_{sj}) \parallel ID_{sj} \parallel T_{s3})$ . The GW sends message  $\{b_{sj}, c_{sj}, T_{s3}\}$  through public channel to  $S_j$ , which verifies validity of received timestamp  $|T_{s3} - T_c| < ||\Delta T$ , extracts  $\beta_j$  from  $b_{sj}$  and computes new value  $c_{sj}^*$ .  $S_j$  checks the satisfaction of  $c_{sj}^*$  with  $c_{sj}$  and stores value  $\beta_j$ .

### 3.2 Login Phase

$U_i$  inserts SC into terminal and inputs the new  $ID_i^*$  and  $PW_i^*$ . SC calculates  $r_i^* = d_i \oplus h(ID_i^* \parallel PW_i^*)$ ,  $MP_i^* = h(PW_i^*)$ ,  $P_i = h(r_i^* \parallel MP_i^*)$ ,  $a_i^* = b_i \oplus h(P_i \parallel MP_i^*)$ ,  $c_i^* = h(a_i^* \parallel MP_i^* \parallel ID_i^*)$  and checks satisfaction of  $c_i^*$  with  $c_i$ .  $U_i$  creates random value  $k_i$ , calculates  $M_1 = k_i \oplus h(a_i \parallel MP_i)$ ,  $M_2 = h(a_i \parallel MP_i \parallel k_i \parallel T_1)$  and sends message  $\{M_1, M_2, ID_i, T_1\}$  to the GW through public channel.

### 3.3 Authentication Phase

The GW checks timestamp  $|T_1 - T_c| < ||\Delta T$  of received message from  $U_i$ , computes  $k_i^* = M_1 \oplus h(a_i \parallel h(PW_i))$ ,  $M_2^* = h(a_i \parallel h(PW_i) \parallel k_i^* \parallel T_1)$  and checks satisfaction with received values. GW calculates  $y_{ij} = h(a_i \parallel \beta_j \parallel ID_i \parallel ID_{sj})$ ,  $M_3 = a_i \oplus y_{ij}$ ,  $M_4 = h(y_{ij} \parallel M_3 \parallel ID_i \parallel T_2)$  and sends message  $\{M_4 \parallel M_3 \parallel ID_i \parallel T_2\}$ .  $U_i$  verifies validity of timestamp  $|T_2 - T_c| < ||\Delta T$ , computes  $y_{ij}^* = a_i \oplus M_3$ ,  $M_4^* = h(y_{ij} \parallel M_3 \parallel ID_i \parallel T_2)$  and checks satisfaction with received values. GW calculates  $M_5 = k_i \oplus h(\beta_j \parallel ID_{sj})$ ,  $M_6 = \beta_j \oplus y_{ij}$ ,  $M_7 = h(y_{ij} \parallel k_i \parallel ID_{sj} \parallel T_3)$  and sends message  $\{M_5 \parallel M_6 \parallel M_7 \parallel ID_{sj} \parallel ID_i \parallel T_3\}$  to  $S_j$ , which checks validity of timestamp  $|T_3 - T_c| < ||\Delta T$ , computes  $k_i^* = M_5 \oplus h(\beta_j \parallel ID_{sj})$ ,  $y_{ij} = \beta_j \oplus M_6$ ,  $M_7^* = h(y_{ij} \parallel k_i^* \parallel ID_{sj} \parallel T_3)$  and compares value  $M_7^*$  with received one.  $S_j$  chooses random nonce  $k_j$  and calculates  $M_8 = k_j \oplus y_{ij}$ ,  $M_9 = h(k_j \parallel ID_{sj} \parallel T_4)$ . Finally,  $S_j$  computes session key  $SK = h(k_i \oplus k_j)$  and sends message  $\{M_8 \parallel M_9 \parallel ID_i \parallel ID_{sj} \parallel T_4\}$  to  $U_i$ , who verifies validity of received timestamp  $|T_4 - T_c| < ||\Delta T$ , calculates  $k_j = M_8 \oplus y_{ij}$ ,  $M_9^* = h(k_j \parallel ID_{sj} \parallel T_4)$ , compares value  $M_9^*$  with received one and computes session key  $SK = h(k_i \oplus k_j)$ .

### 3.4 Password Changing Phase

$U_i$  inserts SC into terminal and inputs  $ID_i$  and  $PW_i^{OLD}$ . SC verifies values and asks  $U_i$  to choose new password.

## IV. SECURITY FLAWS IN AKANSHA S. ET AL.'S SCHEME

To Some weaknesses of Akansha S. et al.'s protocol is detected and analyzed as below:

- 1) In registration part between the GW and sensor node, GW creates secret value  $K_{GW-S_j}$  and hides it inside of  $\beta_j$ . Afterwards, the GW conceals value  $\beta_j$  inside of  $b_{sj}, c_{sj}$  and sends message  $\{b_{sj}, c_{sj}, T_{s3}\}$  to sensor node, which extracts  $\beta_j$  from  $b_{sj}$  computing  $\beta_j = b_{sj} \oplus h(ID_{sj} \parallel h(PW_{sj}))$ . Due to sensor node doesn't have information about  $K_{GW-S_j}$ , which is hidden inside of value  $\beta_j$ , sensor node  $S_j$  is not able to determine the identity of GW. So, if an adversary captures GW, then he can creates his own forged secret value  $K_{GW-S_j}$  and send to sensor node  $S_j$ .
- 2) In the last step of registration part, user  $U_i$  computes additional value  $d_i = r_i \oplus h(ID_i \parallel PW_i)$  and puts values  $h(\cdot), b_i, c_i, d_i, ID_i$  into smart card. SC already contains values  $d_i$  and  $ID_i$ . So, to extract value  $r_i$  from SC, an attacker only needs to guess value  $PW_i$ . Upon  $r_i$  is found, an adversary can obtain other values.
- 3) In authentication part, sensor node  $S_j$  calculates session key using generated random value  $k_j$ . The GW and user  $U_i$  don't know value of  $k_j$  or session key. If an adversary captures sensor node  $S_j$  and obtains stored value  $\beta_j$ , then he can extract values  $k_i$  and  $y_{ij}$  from received values sent by the GW. Afterwards, an adversary generates an arbitrary value

$k_j$  and computes session key. Upon user  $U_i$  received message from sensor node  $S_j$ , he cannot verify identity of  $k_j$  or session key value.

- 4) Generally, in this scheme only hash function, concatenation and XOR functions are employed. Maybe it is the right decision in term of less energy consumption and fast computational speed of sensor nodes. But, we must remember that the first requirement for authentication protocol is security. It is not enough secure to only use hash, concatenation or XOR functions against modern attacks. Because, there are some research works related to attacks on the concatenation and XOR hash combiners [14], [15] have been achieved, which points to their vulnerabilities.

## V. REFINED PROTOCOL DESIGN

The IEEE 802.15.4 determines parameters for low-range personal area networks, which was specially designed in terms of providing devices with low speed and low-cost communication. The encryption mechanism pointed in IEEE 802.15.4 standard mainly designed for symmetric key encryption. There are two kinds of devices: a Reduced Functional Device (RFD) and a Full Functional Device (FFD). While an RFD acts as a low-power sensor, an FFD acts as a gateway. We model symmetric key based wireless sensor network, which contains some sensor nodes, gateway and user. A gateway authenticates user, computes session key and distributes it to user and sensor node.

## VI. PROPOSED SCHEME

We proposed a new ECC-based user authentication scheme for Wireless Sensor Networks, which resolves all the identified weaknesses of Akansha S. et al.'s scheme and ensures high-level security. Our scheme reduces the sensor node's expenses of elliptic curve random point scalar multiplications. We replaced them with low expenses and effective symmetric-key based operations. In addition, to make our protocol more secure, we combined Elliptic Curve Digital Signature Algorithm (ECDSA) with Message Authentication Code (MAC) for the entities authentication.

TABLE 2  
NOTATIONS

Symbol	Definition
$U_i$	$i_{th}$ User
$S_j$	$j_{th}$ Sensor Node
SC	Smart card
$ID_i$	$i_{th}$ User's identity
$ID_j$	$j_{th}$ Sensor node's identity
$PW_i$	$i_{th}$ User's password
$PW_j$	$j_{th}$ Sensor node's password
GW	Gateway
$q$	a large prime
$p$	a large prime such that $p = 2q + 1$
$P$	a base point of large order $n$ chosen for an elliptic curve, which is known to all $U_i$
$Q_i, q_i$	Public and private key pair of a $U_i$
$Q_v, q_v$	Public and private key pair of the powerful node V
$Sign_u(m)$	The signing algorithm based on ECDSA protocols under $U_i$ 's private key $q_i$ and the signed message $m$
$MAC(M, k)$	The calculation of a MAC for a message $m$ using MAC key $k$
$N_i, N_k$	Nonces
$T$	Timestamp
$\oplus, \parallel, h(\cdot)$	XOR, concatenation and a lightweight one way hash function
$sk$	Session key



### 6.1 Registration Phase

The registration part contains two subparts. The first part is between user and gateway and the second part is between sensor node and the gateway.

#### 6.1.1 Registration between User and Gateway

- 1) The user  $U_i$  chooses his  $ID_i, PW_i$ , selects random integer  $b$  and computes  $pw = h(PW_i \oplus b) * P$
- 2)  $U_i$  creates the pairs of signing and verifying keys  $(Q_i, q_i)$  and sends message  $\{pw, ID_i, Q_i\}$  to the GW
- 3) GW stores value  $Q_i$ , sets the pair of private and public keys  $(Q_v, q_v)$
- 4) GW computes  $a = h(pw \parallel ID_i) * P$  and sends message  $\{a, q_v\}$  to  $U_i$
- 5) When  $U_i$  receives message stores values  $(a, q_v, b, P)$  in SC

#### 6.1.2 Registration between Gateway and Sensor Node

- 1)  $S_j$  selects its  $ID_j, h(PW_j)$  and generates random number  $y$
- 2)  $S_j$  computes  $c = h(ID_j \parallel y), j = h(ID_j \parallel c \parallel h(PW_j) \parallel T_1)$  and sends message  $\{j, ID_j, h(PW_j), c, T_1\}$  to the GW
- 3) GW checks timestamp  $T_1$  and compares received value  $j$  with new one.
- 4) GW calculates  $d = h(c \parallel ID_j) * P, g = d.x \oplus h(ID_j \parallel h(PW_j))$  where  $x$  is the coordinator of  $d$  and calculates  $f = h(g \parallel T_2)$
- 5) GW sends message  $\{f, g, T_2\}$  to  $S_j$
- 6)  $S_j$  checks timestamp  $T_2$ , compares received value  $d$  with new one and stores it.

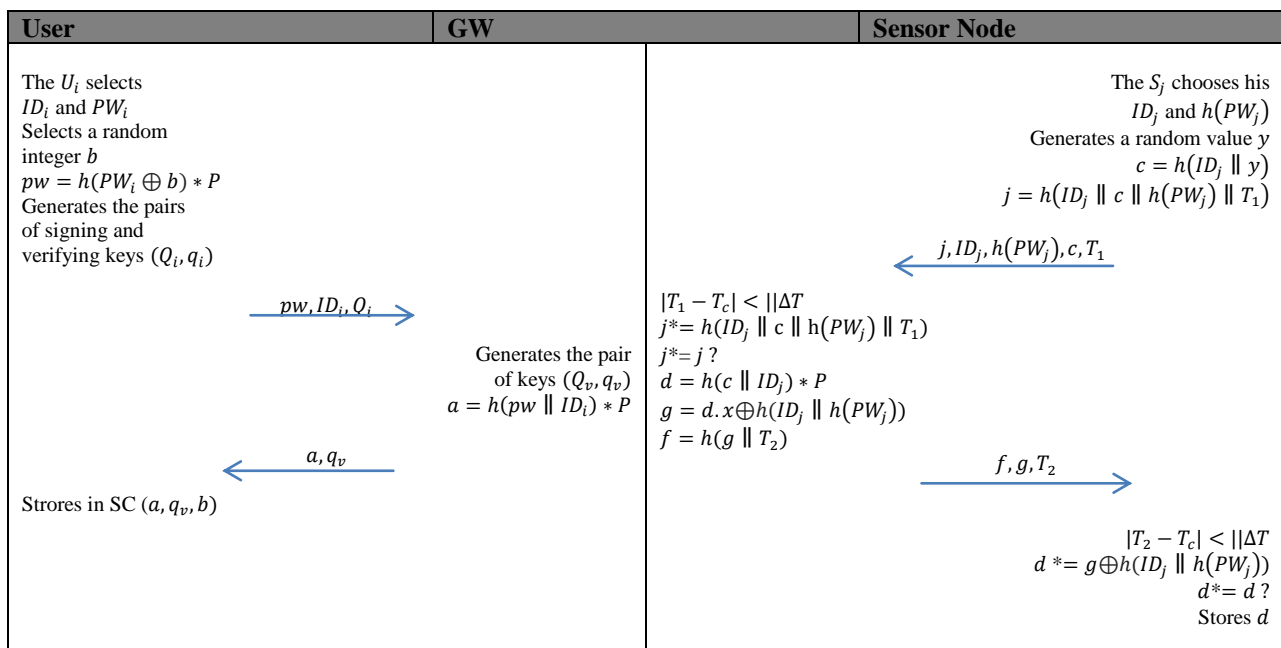


FIGURE 1 REGISTRATION PHASE

### 6.2 Login and Authentication Phase

After user passed registration phase, he can connect to sensor node via the gateway node.

#### 6.2.1 Login phase

- 1)  $U_i$  inserts SC into terminal, inputs  $ID_i$  and  $PW_i$
- 2) Computes new values  $a^* = h(pw \parallel ID_i) * P$  and compares with value taken from SC  $a^* = a ?$
- 3)  $U_i$  selects random nonce  $k$  and  $N_i$ , where  $k$  is a MAC key

- 4)  $U_i$  computes secret value  $R = a * q_v$  and cipher text  $w = (k \parallel N_i) \oplus R . x$
- 5) Generates an ECDSA signature  $s = Sig_u(a \parallel w)$  and sends message  $\{s, a, w\}$  to the GW

**6.2.2 Authentication phase**

- 1) When the GW receives message from  $U_i$  restores secret value  $R = h(pw \parallel ID_i) * Q_v$
- 2) Extracts  $k$  from value  $w$
- 3) Generates random value  $N_k$
- 4) Computes session key  $sk = h(N_k \parallel k)$  and cipher text  $e = sk \oplus R . x$
- 5) GW first sends message  $\{e, MAC(e, k)\}$  to  $U_i$ , which upon receiving, verifies MAC and calculates session key  $sk = e \oplus R . x$
- 6) GW computes  $Z = R . x \oplus d . x$  and forwards message  $\{pw, e, Z, w\}$  to  $S_j$
- 7)  $S_j$  extracts  $R$  from  $Z = R . x \oplus d . x$  and computes session key  $sk = e \oplus R . x$
- 8)  $S_j$  extracts  $k$  from  $w$  and sends message  $E(pw . x \parallel N_i, sk), MAC(E(pw . x \parallel N_i, sk), k)$  to  $U_i$
- 9)  $U_i$  verifies MAC, decrypts cipher text and checks satisfaction of received session key value with his own one  $sk^* = sk?$

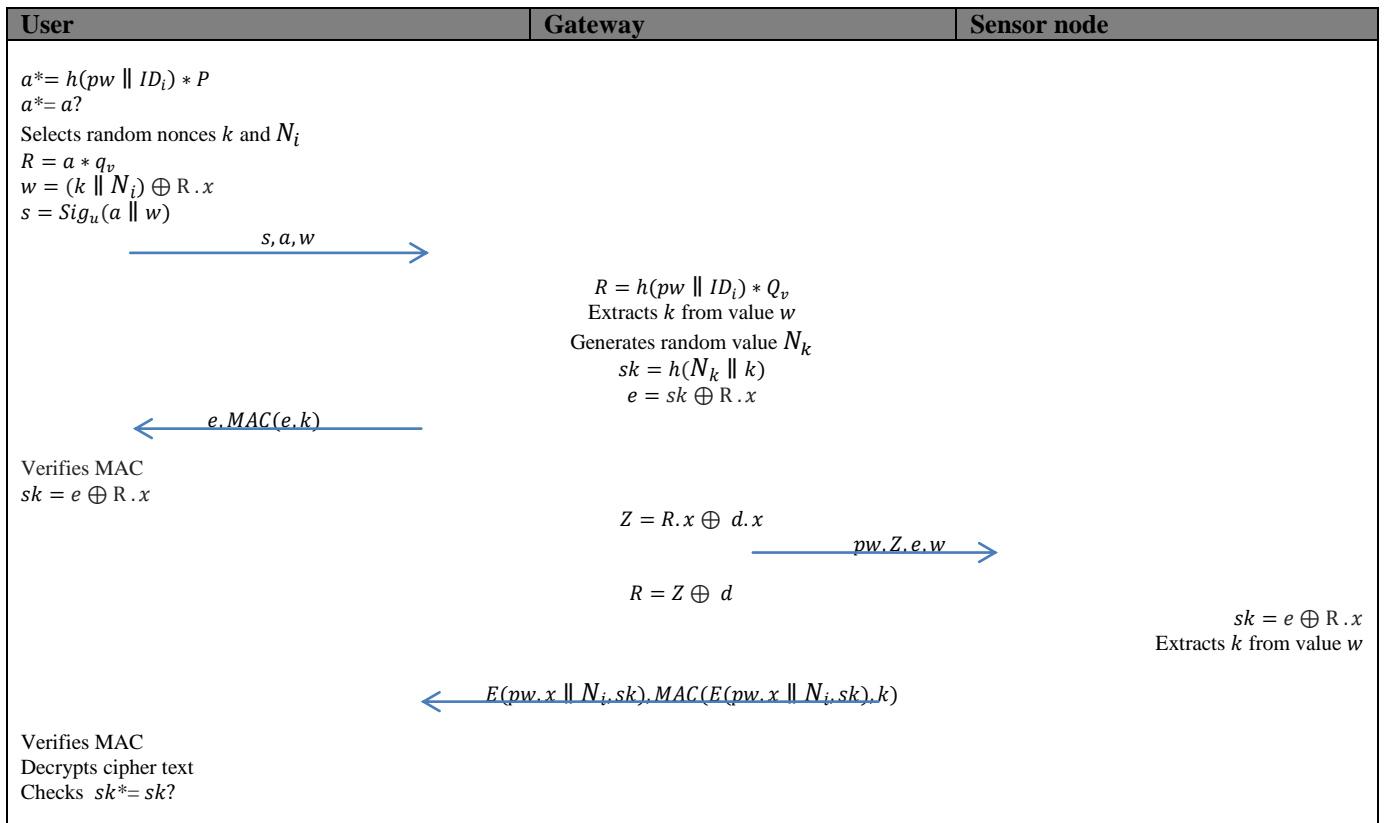


**FIGURE 2 LOGIN AND AUTHENTICATION PHASE**

**VII. SECURITY ANALYSIS**

This section provides a security analysis of our work and proves the proposed scheme has resistance to the several attacks and is able to provide a secure authentication.

**7.1 Sensor Node Replication Attack**

This type of attack, where an attacker generates his own low-cost sensor node called forge node and misinforms the network to affirm them as a legitimate one. To perform this attack, an attacker needs to physically capture one of the nodes and collect all secret values (ID, cryptographic keys and etc.). After that, an attacker duplicates the sensor node and creates one or more

copies of the node into the current network. In terms of avoiding replayed message attack in our protocol, we used a fresh nonce  $n$ , which sent by user  $U_i$ . If an attacker plans to replay the previously transferred message from user  $U_i$ , then he has to use the previously sent  $n$  nonce value. Thus, an adversary is not able to reply message, because the GW knows the last nonce value, which was created by user  $U_i$ .

## 7.2 Sybil Attack

Generating different accounts from various IP addresses an adversary pretends himself as multiple forge identities. In terms of resistance against such attack we used ECDSA to create and verify the signature of each user  $U_i$ . The attacker cannot pretend as user  $U_i$  and pass GW without the private key  $q_i$ . Even in worst case, the attacker expose user  $U_i$  but still is unable to claim a new identity of user  $U_i$  in the neighborhood of user  $U_j$  because the attacker only knows the private key of the exposed user  $U_i$  but not the private key of user  $U_j$ . In fine, due to using ECDSA on the gateway to authenticate the identity of user, the proposed protocol provides withstand the Sybil attack.

## 7.3 Insider Attack

An insider attack usually appears when the GW or system administrator can have access to a user's credentials and can impersonate user. In our scheme, for the insider of GW node is not possible to get user  $U_i$ 's password, because the GW only have a value  $pw$ , which contains a value  $b$  and  $PW_i$ . The value  $b$  is high entropy value, which is not revealed to the GW. Thus, it is not possible to guess both values of  $pw$ .

## 7.4 Man-in-the-Middle-Attack

An adversary catches the messages being exchanged between the entities and sends forge messages impersonating one of them. Regarding our scheme, the message exchanging between user  $U_i$  and GW, performed using signature and MAC key, which allow only to the legal entities authenticate each other.

## 7.5 Mutual Authentication

Mutual authentication is the main security property for the authentication protocol. In our case, the proposed scheme provides mutual authentication among 2 entities: user and gateway. The signature of the message sent from user  $U_i$  to GW provides an authentication of user  $U_i$ . Also, a Message Authentication Code will provide evidence of integrity for the message. Because, the MAC key  $k$  was generated and encrypted by user  $U_i$ . Thus, only GW with private key  $q_v$  can recover value  $k$ . When GW sends back message, it will use the same MAC key  $k$ .

## VIII. CONCLUSION

In this paper, Akansha S. et al.'s protocol has been reviewed and analysed. Based on the cryptanalysis of their scheme, have been found some drawbacks. In registration part, the gateway generates new secret value, which is not known to sensor node. Hence, sensor node is unable to check identity of received secret value. Also, there is possibility of smart card breach attack, because the adversary only needs to guess user's password to obtain values from the smart card. In authentication part, sensor node computes session key value and sends to user. It leads to the sensor impersonation attack since user doesn't know value of session key and cannot authenticate sensor node. The general vulnerability of Akansha S. et al.'s scheme is that they only used a hash function, XOR and concatenation. As mentioned above, these operations cannot provide enough security. Comparing to the Akansha S. et al.'s scheme, we have designed a protocol based on the IEEE 802.15.4 standard of network model using ECC. In our scheme, the signature algorithm ECDSA and the Message Authentication Code (MAC) have been implemented, which provides a mutual authentication. Also, in registration part, the scheme provides secure key agreement resistant to the smart card breach attack.

## REFERENCES

- [1] A. Joux, Multicollisions in iterated hash functions. Application to cascaded constructions, Annual International Cryptology Conference, Springer, 2004, pp. 306-316.
- [2] A.K. Maurya, V. Sastry, S.K. Udghata, Cryptanalysis and Improvement of ECC-Based Security Enhanced User Authentication Protocol for Wireless Sensor Networks, International Symposium on Security in Computing and Communication, Springer, 2015, pp. 134-145.
- [3] A. Singh, A.K. Awasthi, K. Singh, Cryptanalysis and Improvement in User Authentication and Key Agreement Scheme for Wireless Sensor Network, Wireless Personal Communications, 1-18.

- 
- [4] A. Tajeddine, A. Kayssi, A. Chehab, I. Elhajj, Authentication schemes for wireless sensor networks, MELECON 2014-2014 17th IEEE Mediterranean Electrotechnical Conference, IEEE, 2014, pp. 367-372.
- [5] D. He, Y. Gao, S. Chan, C. Chen, J. Bu, An Enhanced Two-factor User Authentication Scheme in Wireless Sensor Networks, Ad Hoc & Sensor Wireless Networks, 10 (2010) 361-371.
- [6] H.-L. Yeh, T.-H. Chen, P.-C. Liu, T.-H. Kim, H.-W. Wei, A secured authentication protocol for wireless sensor networks using elliptic curves cryptography, Sensors, 11 (2011) 4767-4779.
- [7] I. Dinur, New Attacks on the Concatenation and XOR Hash Combiners, Annual International Conference on the Theory and Applications of Cryptographic Techniques, Springer, 2016, pp. 484-508.
- [8] K.H. Wong, Y. Zheng, J. Cao, S. Wang, A dynamic user authentication scheme for wireless sensor networks, IEEE International Conference on Sensor Networks, Ubiquitous, and Trustworthy Computing (SUTC'06), IEEE, 2006, pp. 8 pp.
- [9] M.L. Das, Two-factor user authentication in wireless sensor networks, IEEE Transactions on Wireless Communications, 8 (2009) 1086-1090.
- [10] M.K. Khan, K. Alghathbar, Cryptanalysis and security improvements of 'two-factor user authentication in wireless sensor networks', Sensors, 10 (2010) 2450-2459.
- [11] M. Turkanović, B. Brumen, M. Hölbl, A novel user authentication and key agreement scheme for heterogeneous ad hoc wireless sensor networks, based on the Internet of Things notion, Ad Hoc Networks, 20 (2014) 96-112.
- [12] S. Bartariya, A. Rastogi, Security in Wireless Sensor Networks: Attacks and Solutions, environment, 5 (2016).
- [13] T.-H. Chen, W.-K. Shih, A robust mutual authentication protocol for wireless sensor networks, ETRI journal, 32 (2010) 704-712.
- [14] W. Shi, P. Gong, A new user authentication protocol for wireless sensor networks using elliptic curves cryptography, International Journal of Distributed Sensor Networks, 2013 (2013).
- [15] Y. Choi, D. Lee, J. Kim, J. Jung, J. Nam, D. Won, Security enhanced user authentication protocol for wireless sensor networks using elliptic curves cryptography, Sensors, 14 (2014) 10081-10106.

## Utilization of bottle caps in concrete

S.T. Rathod<sup>1</sup>, L.R.Bankar<sup>2</sup>, U.R.Hakepatil<sup>3</sup>, M.M.Vhanamane<sup>4</sup>, S.S.Warpe<sup>5</sup>

Department of Civil Engineering, Bharati Vidyapeeth's, College Of Engineering Lavale, Savitribai Phule Pune University, India

**Abstract**— Advances in technology enhance human comforts and in the same time damages the environment. Plastic used as cap for containers preserve liquids in the bottles very well, but the disposal of caps particularly bottle caps which harmful to environmental. Hence an attempt has been made in the present investigations to study the influence of addition of waste materials like soft drink bottle caps dosage of 0%, 5%, 10%, 15% & 20% of total weight of coarse aggregate as fibers. M25 grade of concrete was produced by replacing coarse aggregate by plastic bottle caps. In this investigation caps were cut into strips. Experimental investigation was carried out adding bottle caps in concrete and tests were carried out as per recommended procedures by relevant codes. Split tensile strength increases with increase of bottle caps. Split tensile and flexural strength of 5.0 % bottle cap fiber concrete increase up to 1.72% and 13.23 % more than plain concrete(without bottle cap plastic) respectively.

**Keywords**— plastic bottle caps, compressive strength, coarse aggregate, split tensile strength , flexural test.

### I. INTRODUCTION

Concrete has an extensive role to play in the construction and improvement of our civil engineering and infrastructure development. Its great strength, durability and veracity are the properties that are utilized in construction of Roads, Bridges, Airports, Railways, and Tunnels, Port, Harbors, and many other infrastructural projects. Plastic waste products deserve special attention on account of non-biodegradable property which is creating a lot of problems in the environment today the construction industry is in need of finding effective materials for increasing the strength of concrete structures with low cost, and with less environmental damages. Currently millions of tons of waste bottle caps are produced in the world. This will ultimately cause pollution and harmful to the ecosystem. . Therefore utilizing waste bottle caps in concrete production not only solves the problem of disposing this ultra-light solid waste but also helps preserve natural resources. A project was taken up to use plastic bottle caps in concrete with following objectives.

### II. OBJECTIVE

- To assess the fresh properties of concrete when coarse aggregates are partially replaced with Waste Bottle Caps (WBC).
- To produce lighter weight polymer concrete for its multidimensional use.
- Optimize the amount of recycle fiber bottle caps in concrete.
- Test demonstration concrete product.
- Develop suitable mix design.
- Provide knowledge/data that will be used for development of concrete work.

### III. METHODOLOGY

The following figure shows the methodology involved in the entire project work.

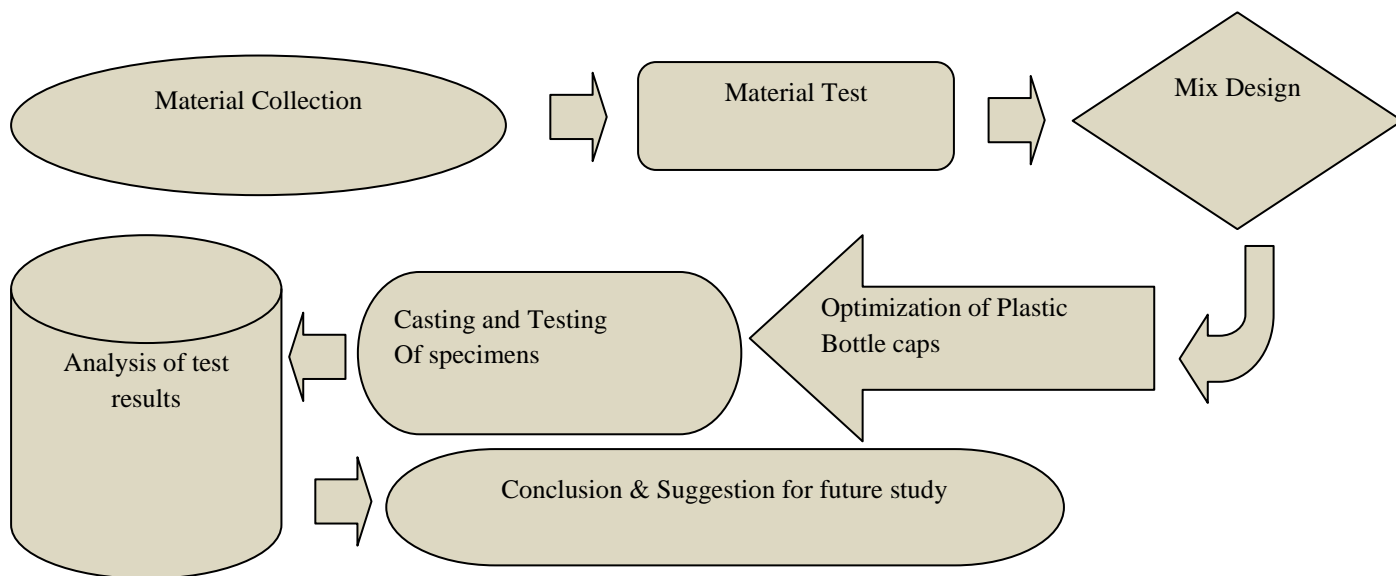


FIG. 1 SHOWS THE ALGORITHM CHART FOR METHODOLOGY

TABLE 1  
PHYSICAL PROPERTIES OF FINE AND COARSE AGGREGATE

Sr. No	Property	Fine Aggregate	Coarse Aggregate
		Results	
1.	Particle Shape, Size	Round, Below 4.75mm	Angular, 20mm
2.	Fineness Modulus	4.175	7.424
3.	Silt content	3%	Nil
4.	Specific Gravity	2.652	2.664

IV. M-25 CONCRETE MIX DESIGN

The M25 concrete mix is designed As per IS- 10262:2009 which gives a mix proportion of 1:1:2 with water cement ratio of 0.40. The concrete used in this research work was made using Binder, Sand and Gravel.

TABLE 2  
MIX PROPORTIONS FOR 1 CUM OF CONCRETE

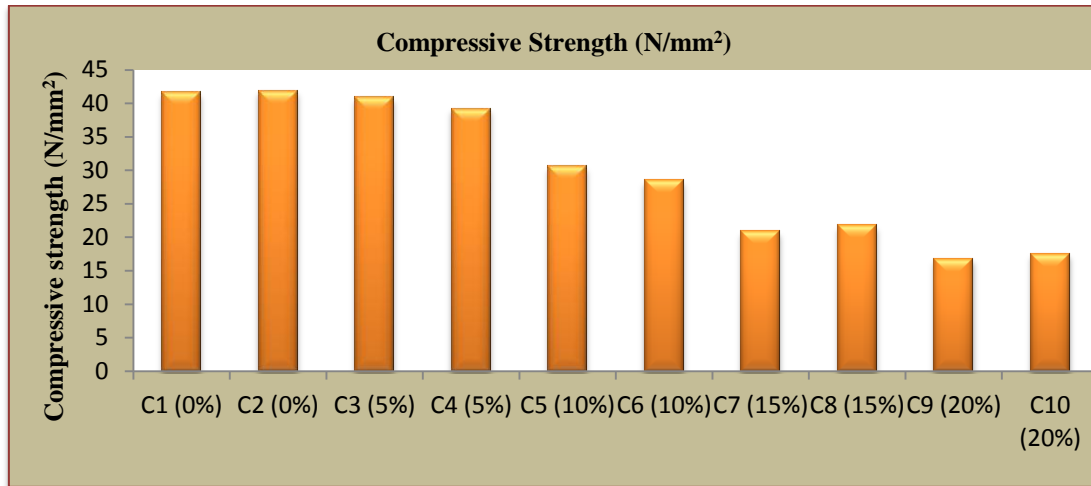
Sr. No.	Descriptions	Quantity
1	Mass of Cement in kg/m <sup>3</sup>	384 kg/m <sup>3</sup> .
2	Mass of Water in kg/m <sup>3</sup>	191.6 kg /m <sup>3</sup>
3	Mass of Fine Aggregate in kg/m <sup>3</sup>	752.71 kg/m <sup>3</sup>
4	Mass of Coarse Aggregate in kg/m <sup>3</sup>	1064.65 kg/m <sup>3</sup>
5	Mass of 20 mm in kg/m <sup>3</sup>	1064.65 kg/m <sup>3</sup>
6	Water Cement Ratio	0.44

TABLE 3  
PARTIAL REPLACEMENT OF BOTTLE CAPS

Sr. No.	Materials	Replacement in % (per Block)				
		1	2	3	4	5
1.	Bottle caps	0%	5%	10%	15%	20%
2.	Coarse agg.	100%	95%	90%	85%	80%

**V. TESTING OF CONCRETE RESULTS**

1. Compressive Strength
2. Split tensile Strength
3. Flexural Strength



**CHART. 1. COMPRESSIVE STRENGTH**

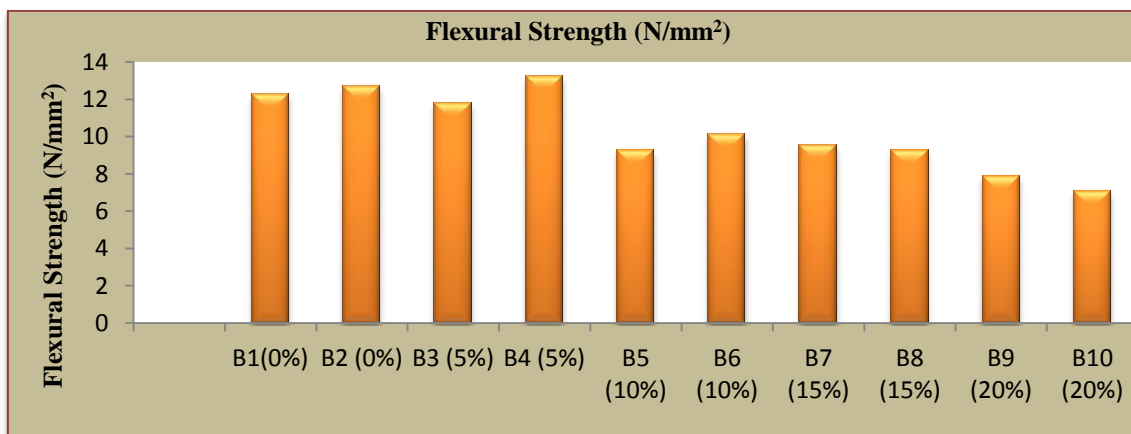


**CHART. 2. FLEXURAL STRENGTH**

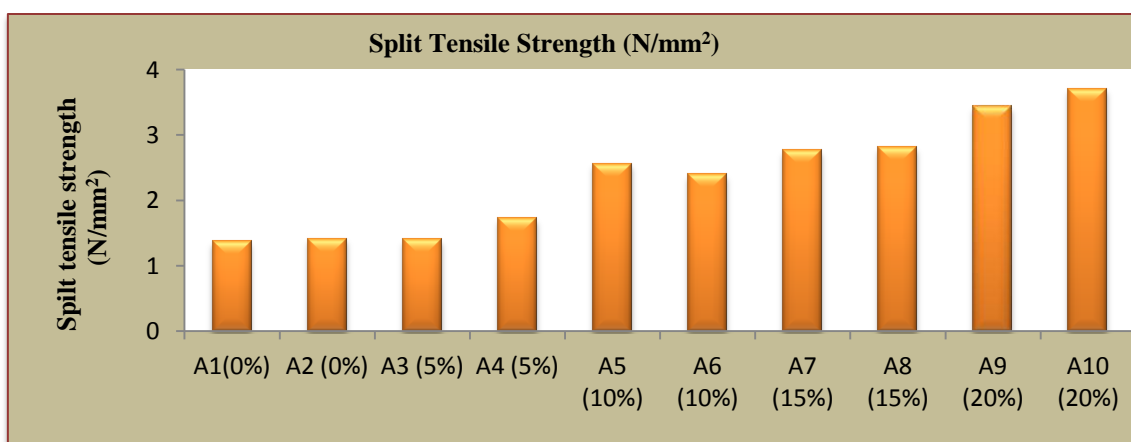


**CHART. 3. SPLIT TENSILE STRENGTH**

## VI. CONCLUSION

Conclusion of our project is as follows:

1. Compressive strength decreases with increase in percentage by 5%, 10%, 15% and 20% of bottle cap fibers.
2. Split tensile strength increases with increase in 5%, 10%, 15% and 20% of fiber.
3. Flexural strength decreases is more prominent with increase in percentage of bottle cap fiber.
4. It is used for the construction of partition walls for multistoried building.
5. It is used for the construction of compound wall & panel.
6. Plastic building material is strong, flexible, water- and heat - resistant.
7. Waste reduction, Conservation of energy.
8. Save money, Generate revenues. Etc.

Hence this concept of mixing is good for strength and workability of concrete. The possibilities of using waste bottle caps (WBC) as partial replacement of coarse aggregate have been explored.

## REFERENCES

- [1] G.C. Behera, R.K. Behera, "Increase in Strength of Concrete by Using Bottle Caps", PP 1937.
- [2] A. Ishaya, I. M. Oyemogum, A. Arinze, "Properties of Concrete Produced with Waste Bottle Caps (WBC) as a Partial Replacement of Coarse Aggregate and Orange Leave Powder as Plasticizer", [Vol.8, No.7, 2016], pp. 91- 92.
- [3] A.A. Jadhav1, V.P. Kulkarni, "Effect on Torsional and Flexural Behavior RC Concrete Beam made with Plastic Waste Bags (PWB) Granules", [Volume 5 Issue 7, July 2016], pp-823.
- [4] Dr. Muhammad Maqbool Sadiq, Muhammad Rafique Khattak. "Literature Review on Different Plastic Waste Materials Use in Concrete", [June 2015, Volume 2, Issue 6].
- [5] M.S.Setty, "Concrete Technology, S.Chand and Company Ltd, Third Edition, pp 608, 1982.
- [6] M.S.Shetty book of concrete technology theory and practice.
- [7] IS 10262- 2009 for mix design of concrete.
- [8] IS- 456:2000 plain & reinforcement concrete



# Haze Removal Using Color Attenuation Prior With Varying Scattering Coefficients

Anandhu Balakrishnan<sup>1</sup>, Shine P James<sup>2</sup>

<sup>1</sup>M.tech-student, College of Engineering Poonjar, Kerala, India

<sup>2</sup>Department of Electronics & Communication, College of Engineering Poonjar, Kerala, India

**Abstract**— This paper deals with removal of haze using color attenuation prior. It will help for dehazing single image. For dehazing linear model is used. It is based on atmospheric scattering model. In this technique saturation and brightness values of an image is considered. It is less time consuming algorithm and also it has greater dehazing effects. Also varying scattering coefficient is used for dehazing purpose. With the depth map of the hazy image, we can smoothly surmise the transmission and give back the scene radiance via the atmospheric scattering model, and thus effectively remove the haze from a single image. It can implement very easily.

**Keywords**— Color attenuation prior, Scattering model, Linear model, Varying Scattering Matrix.

## I. INTRODUCTION

Outdoor images taken in bad weather (e.g., foggy or hazy) usually lose contrast and color fidelity, resulting from the fact that light is absorbed and scattered by the turbid medium such as particles and water droplets in the atmosphere during the process of propagation. Moreover, most automatic systems, which strongly depend on the definition of the input images, fail to work normally caused by the degraded images. Therefore, improving the technique of image haze removal will benefit many image understanding and computer vision applications such as aerial imagery, image classification, image/video retrieval, remote sensing and video analysis and recognition. Since concentration of the haze is different from place to place and it is hard to detect in a hazy image, image dehazing is thus a challenging task.

In almost every practical scenario the light reflected from a surface is scattered in the atmosphere before it reaches the camera. This is due to the presence of aerosols such as dust, mist, and fumes which deflect light from its original course of propagation. In long distance photography or foggy scenes, this process has a substantial effect on the image in which contrasts are reduced and surface colors become faint. Such degraded photographs often lack visual vividness and appeal, and moreover, they offer a poor visibility of the scene contents. This effect may be an annoyance to amateur, commercial, and artistic photographers as well as undermine the quality of underwater and aerial photography. This may also be the case for satellite imaging which is used for many purposes including cartography and web mapping, land-use planning, archeology, and environmental studies.

Early researchers use the traditional techniques of image processing to remove the haze from a single image (for instance, histogram-based dehazing methods ([4], [5])). However, the dehazing effect is limited, because a single hazy image can hardly provide much information. Later, researchers try to improve the dehazing performance with multiple images. In [4] and [7], polarization based methods are used for dehazing with multiple images which are taken with different degrees of polarization. It is based on the fact that usually airlight scattered by atmospheric particles is partially polarized. Polarization filtering alone cannot remove the haze effects, except in restricted situations. Our method, however, works under a wide range of atmospheric and viewing conditions. We analyze the image formation process, taking into account polarization effects of atmospheric scattering.

In Chromatic Framework method [8], propose haze removal approaches with multiple images of the same scene under different weather conditions. In this develop a general chromatic framework for the analysis of images taken under poor weather conditions. The wide spectrum of atmospheric particles makes a general study of vision in bad weather hard. So, we limit ourselves to weather conditions that result from fog and haze. We begin by describing the key mechanisms of scattering. Next, we analyze the dichromatic model proposed, and experimentally verify it for fog and haze. Then, we derive several useful geometric constraints on scene color changes due to different but unknown atmospheric conditions.

In Dark Channel Prior method [9], proposes a simple but effective image prior dark channel prior to remove haze from a single input image. The dark channel prior is a kind of statistics of outdoor haze-free images. It is based on a key observation most local patches in outdoor haze-free images contain some pixels whose intensity is very low in at least one color channel.

Using this prior with the haze imaging model, we can directly estimate the thickness of the haze and recover a high-quality haze-free image. Results on a variety of hazy images demonstrate the power of the proposed prior. Moreover, a high-quality depth map can also be obtained as a byproduct of haze removal. The dark channel prior is based on the statistics of outdoor haze-free images.

In method proposed by T. Tan [10], It is automated method. This method is based on two basic observations: first, images with enhanced visibility (or clear-day images) have more contrast than images plagued by bad weather; second, airlight whose variation mainly depends on the distance of objects to the viewer tends to be smooth. Relying on these two observations, we develop a cost function in the framework of Markov random fields, which can be efficiently optimized by various techniques, such as graph-cuts or belief propagation.

In this paper, we propose a novel color attenuation prior for single image dehazing. This simple and powerful prior can help to create a linear model for the scene depth of the hazy image. By learning the parameters of the linear model with a supervised learning method, the bridge between the hazy image and its corresponding depth map is built effectively. With the recovered depth information, we can easily remove the haze from a single hazy image. The efficiency of this dehazing method is dramatically high and the dehazing effectiveness is also superior to that of prevailing dehazing algorithms

## II. METHODOLOGY

### a. Atmospheric Scattering Model

To describe the formation of a hazy image, the atmospheric scattering model, which is widely used in computer vision and image processing? The model can be expressed as follows:

$$\mathbf{I}(x) = \mathbf{J}(x)t(x) + \mathbf{A}(1 - t(x)) \quad (2.1)$$

$$t(x) = e^{-\beta d(x)} \quad (2.2)$$

Where  $x$  is the position of the pixel within the image,  $\mathbf{I}$  is the hazy image,  $\mathbf{J}$  is the scene radiance representing the haze-free image,  $\mathbf{A}$  is the atmospheric light,  $t$  is the medium transmission,  $\beta$  is the scattering coefficient of the atmosphere and  $d$  is the depth of scene.  $\mathbf{I}$ ,  $\mathbf{J}$  and  $\mathbf{A}$  are all three-dimensional vectors in RGB space. Since  $\mathbf{I}$  is known, the goal of dehazing is to estimate  $\mathbf{A}$  and  $t$ , then restore  $\mathbf{J}$  according to Equation 2.1. It is worth noting that the depth of the scene  $d$  is the most important information. Since the scattering coefficient  $\beta$  can be regarded as a constant in homogeneous atmosphere condition, the medium transmission  $t$  can be estimated easily according to Equation 3.2 if the depth of the scene is given. Moreover, in the ideal case, the range of  $d(\mathbf{x})$  is  $[0, +\infty)$  as the scenery objects that appear in the image can be very far from the observer, and we have:

$$\mathbf{I}(x) = \mathbf{A} \quad d(x) \rightarrow \infty \quad (2.3)$$

### b. Color Attenuation Prior

To detect or remove the haze from a single image is a challenging task in computer vision, because little information about the scene structure is available. In spite of this, the human brain can quickly identify the hazy area from the natural scenery without any additional information. This inspired us to conduct a large number of experiments on various hazy images to find the statistics and seek a new prior for single image dehazing. Interestingly, we find that the brightness and the saturation of pixels in a hazy image vary sharply along with the change of the haze concentration.

Fig. 2.1 gives an example with a natural scene to show how the brightness and the saturation of pixels vary within a hazy image. As illustrated in Fig. 2.1(d), in a haze-free region, the saturation of the scene is pretty high, the brightness is moderate and the difference between the brightness and the saturation is close to zero. But it is observed from Fig. 2.1(c) that the saturation of the patch decreases sharply while the color of the scene fades under the influence of the haze, and the brightness increases at the same time producing the high value of the difference. Furthermore, Fig. 2.1(b) shows that in a dense-haze region, it is more difficult for us to recognize the inherent color of the scene, and the difference is even higher than that in Fig. 2.1(c). It seems that the three properties (the brightness, the saturation and the difference) are prone to vary regularly in a single hazy image according to this observation.

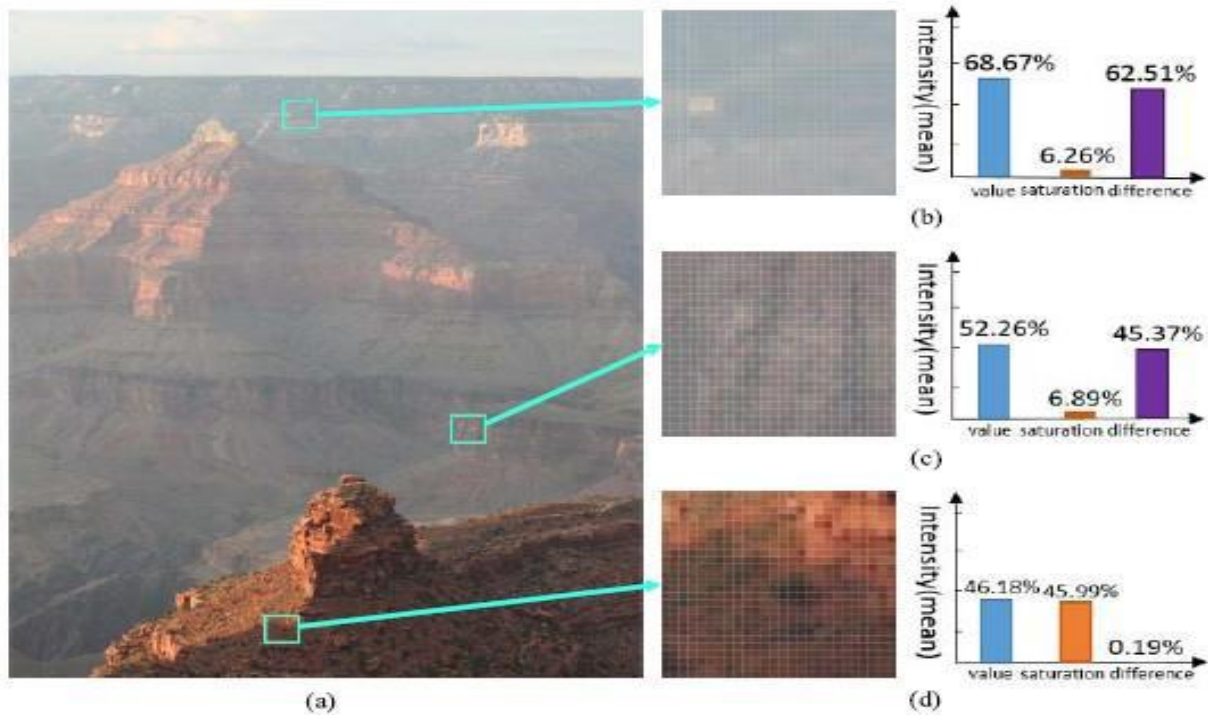


**FIGURE 2.1: THE CONCENTRATION OF THE HAZE IS POSITIVELY CORRELATED WITH THE DIFFERENCE BETWEEN THE BRIGHTNESS AND THE SATURATION. (A) A HAZY IMAGE. (B) THE CLOSE-UP PATCH OF A DENSE-HAZE REGION AND ITS HISTOGRAM. (C) THE CLOSE-UP PATCH OF A MODERATELY HAZY REGION AND ITS HISTOGRAM. (D) THE CLOSE-UP PATCH OF A HAZE-FREE REGION AND ITS HISTOGRAM.**

In the haze-free condition, the scene element reflects the energy that is from the illumination source (e.g., direct sunlight, diffuse skylight and light reflected by the ground), and little energy is lost when it reaches the imaging system. The imaging system collects the incoming energy reflected from the scene element and focuses it onto the image plane. Without the influence of the haze, outdoor images are usually with vivid color. In hazy weather, in contrast, the situation becomes more complex. There are two mechanisms (the direct attenuation and the airlight) in imaging under hazy weather.

On one hand, the direct attenuation caused by the reduction in reflected energy leads to low intensity of the brightness. To understand this, we review the atmospheric scattering model. The term  $J(x)t(x)$  in Equation 2.1 is used for describing the direct attenuation. It reveals the fact that the intensity of the pixels within the image will decrease in a multiplicative manner. So it turns out that the brightness tends to decrease under the influence of the direct attenuation. On the other hand, the white or gray airlight, which is formed by the scattering of the environmental illumination, enhances the brightness and reduces the saturation. We can also explain this by the atmospheric scatter model.

The rightmost term  $A(1 - t(x))$  in Equation 3.1 represents the effect of the airlight. It can be deduced from this term that the effect of the white or gray airlight on the observed values is additive. Thus, caused by the airlight, the brightness is increased while the saturation is decreased. Since the airlight plays a more important role in most cases, hazy regions in the image are characterized by high brightness and low saturation. Whats more, the denser the haze is, the stronger the influence of the airlight would be. This allows us to utilize the difference between the brightness and the saturation to estimate the concentration of the haze.

Since the concentration of the haze increases along with the change of the scene depth in general, we can make an assumption that the depth of the scene is positively correlated with the concentration of the haze and we have:

$$d(x)ac(x) = v(x) - s(x) \tag{2.4}$$

Where  $d$  is the scene depth,  $c$  is the concentration of the haze,  $v$  is the brightness of the scene and  $s$  is the saturation. We regard this statistics as color attenuation prior

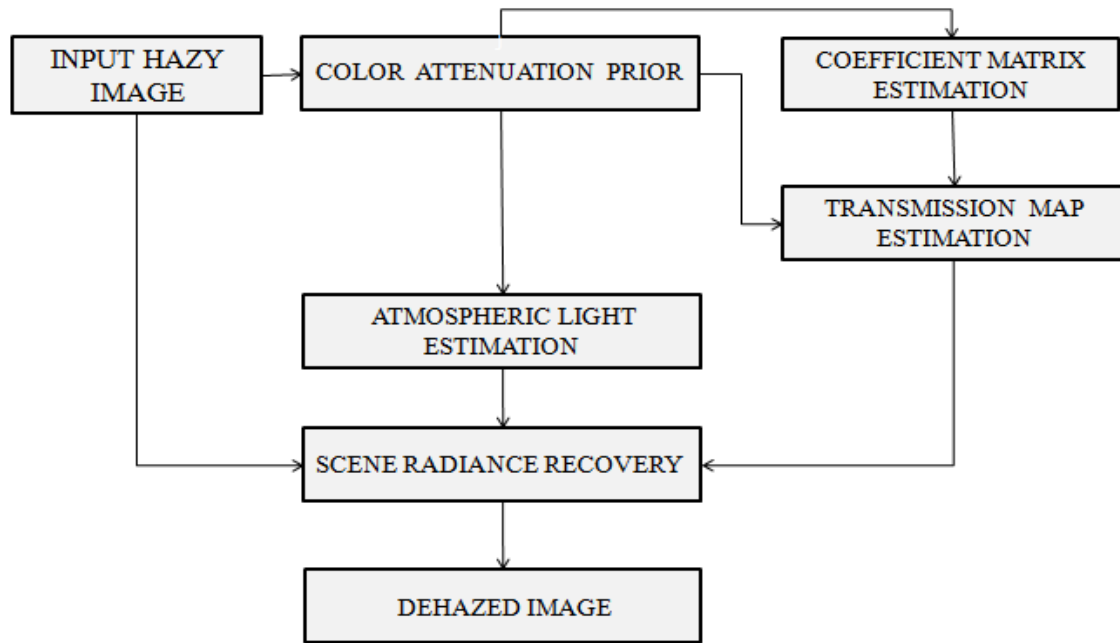


FIGURE 2.2: FLOWCHART OF PROPOSED METHOD

### c. Scene Depth Restoration

#### i. The Linear Model Definition

As the difference between the brightness and the saturation can approximately represent the concentration of the haze, we can create a linear model, i.e., a more accurate expression, as follows:

$$d(x) = \theta_0 + \theta_1 v(x) + \theta_2 s(x) + \varepsilon(x) \quad (2.5)$$

Where  $x$  is the position within the image,  $d$  is the scene depth,  $v$  is the brightness component of the hazy image,  $s$  is the saturation component,  $\theta_0, \theta_1, \theta_2$  are the unknown linear coefficients,  $\varepsilon(x)$  is a random variable representing the random error of the model, and  $\varepsilon$  can be regarded as a random image. Gaussian density for  $\varepsilon$  with zero mean and variable  $\sigma^2$ .

As for the linear coefficients  $\theta_0, \theta_1, \theta_2$  we use the gradient descent algorithm to estimate their values. By taking the partial derivatives of  $\ln L$  with respect to  $\theta_0, \theta_1, \theta_2$  respectively, The expression for updating the linear coefficients are also given below:

$$\frac{\partial \ln L}{\partial \theta_0} = \frac{1}{\sigma^2} \sum_{i=1}^n (dg_i - (\theta_0 + \theta_1 v(x) + \theta_2 s(x))) \quad (2.6)$$

$$\frac{\partial \ln L}{\partial \theta_1} = \frac{1}{\sigma^2} \sum_{i=1}^n v(x_i) (dg_i - (\theta_0 + \theta_1 v(x) + \theta_2 s(x))) \quad (2.7)$$

$$\frac{\partial \ln L}{\partial \theta_2} = \frac{1}{\sigma^2} \sum_{i=1}^n s(x_i) (dg_i - (\theta_0 + \theta_1 v(x) + \theta_2 s(x))) \quad (2.8)$$

$$\theta_i := \theta_i + \frac{\partial \ln L}{\partial \theta_i} \quad i = \{0, 1, 2\} \quad (2.9)$$

There are many epochs are used in our case, and the best learning result is that  $\theta_0 = 0.121779$ ,  $\theta_1 = 0.959710$ ,  $\theta_2 = 0.780245$ ,  $\sigma = 0.041337$ . Once the values of the coefficients have been determined, they can be used for any single hazy image. These parameters will be used for restoring the scene depths of the hazy images in this paper.

## ii. Estimation of the Depth Information

As the relationship among the scene depth  $d$ , the brightness  $v$  and the saturation  $s$  has been established and the coefficients have been estimated, we can restore the depth map of a given input hazy image according to Equation 2.5. However, this model may fail to work in some particular situations. For instance, the white objects in an image are usually with high values of the brightness and low values of the saturation. Therefore, the proposed model tends to consider the scene objects with white color as being distant. Unfortunately, this misclassification will result in inaccurate estimation of the depth in some cases.

To overcome this problem, we need to consider each pixel in the neighbourhood. Based on the assumption that the scene depth is locally constant, we process the raw depth map by:

$$d_r(x) = \text{median}_{y \in \Omega_r(x)} d(y) \quad (2.10)$$

Where  $\Omega_r(x)$  is an  $r \times r$  neighbourhood centered at  $x$ , and  $d_r$  is the depth map with scale  $r$ . The new depth map  $d_{15}$  can well handle the geese regions.

## iii. Guided Image Filtering

In some cases, the blocking artifacts appear in the image. To refine the depth map, we use the guided image filtering [2] to smooth the image. As can be seen, the blocking artifacts are suppressed effectively. haze-free images and their estimated depth maps. As can be seen, the restored depth maps have darker color in haze-free regions while having lighter color in dense-haze regions as expected. With the estimated depth map, the task of dehazing is no longer difficult. These filtering operations have good edge preserving property. The equation for the calculation of filtered output given as:

$$q_i = \bar{a}_i I_i + \bar{b}_i \quad (2.11)$$

Where  $q_i$  is filtered output,  $I_i$  is guidance image and  $\bar{a}_i$  and  $\bar{b}_i$  are linear coefficients. Linear coefficients values are calculated by using input image and guidance image by some sort of processing such as mean, variance, covariance values etc.

## d. Transmission Map Estimation

Transmission Map ( $t$ ) can be calculated by using the equation 3.2. In that equation  $\beta$  is atmospheric scattering coefficient value and  $d(x)$  is scene depth value after Guided Image Filtering. In the previous works constant  $\beta$  value is used. But in our method varying scattering coefficient matrix is used. It will create according to the haze concentration in the scene depth image. The transmission maps have effects on direct attenuation along with haze free image. The calculation of scattering coefficient matrix is given below.

## i. Scattering Coefficient Matrix Generation

Scattering coefficient matrix is created according to the haze concentration in the image. For the visible light spectrum, the relationship between the scattering coefficient  $\beta$ , and the wavelength  $\lambda$ , is given by the inverse power law.  $\beta$  does not change appreciably with wavelength (analogous to Rayleighs law for small air particles)[5]. Equation to calculate the scattering coefficient matrix is given below as:

$$\beta(\gamma) = \frac{K}{C^\gamma} \quad \gamma = \{0,1,2,3,4\} \quad (2.12)$$

$\gamma$  value is chosen according to the haze concentration scene depth image. If the pixel intensity value is high in the scene depth image, then the value of  $\gamma$  should be zero. If the intensity value is low, then the  $\gamma$  value is four.  $K$  and  $C$  are fixed values.

## e. Estimation Of Atmospheric Light

We have explained the main idea of estimating the atmospheric light in Section 2.1. In this section, we describe the method in more detail. As the depth map of the input hazy image has been recovered, the distribution of the scene depth is known. It shows the estimated depth map of a hazy image. Bright regions in the map stand for distant places. According to Equation given below as:

$$\mathbf{A} = \mathbf{I}(x), x \in \{x \mid d(y) \leq d(x)\} \quad (2.13)$$

From it, pick the top 0.1 percent brightest pixels in the depth map, and select the pixel with highest intensity in the corresponding hazy image  $\mathbf{I}$  among these brightest pixels as the atmospheric light  $\mathbf{A}$ .

#### f. Scene Radiance Recovery

Now that the depth of the scene  $d$  and the atmospheric light  $\mathbf{A}$  are known, we can estimate the medium transmission  $t$  easily according to Equation 2.2 and recover the scene radiance  $\mathbf{J}$  in Equation 2.1. For convenience, we rewrite Equation 2.1 as follows:

$$\mathbf{J}(x) = \frac{\mathbf{I}(x) - \mathbf{A}}{t(x)} + \mathbf{A} = \frac{\mathbf{I}(x) - \mathbf{A}}{e^{-\beta d(x)}} + \mathbf{A} \quad (2.14)$$

Where  $\mathbf{J}$  is the haze-free image we want. For avoiding producing too much noise, we restrict the value of the transmission  $t(x)$  between 0.1 and 0.9. So the final function used for restoring the scene radiance  $\mathbf{J}$  in the proposed method can be expressed by:

$$\mathbf{J}(x) = \frac{\mathbf{I}(x) - \mathbf{A}}{\min(\max(e^{-\beta d(x)}, 0.1), 0.9)} + \mathbf{A} \quad (2.15)$$

### III. EXPERIMENTAL RESULTS

This algorithm is mainly based on the concept of color attenuation prior; in this technique difference between saturation and brightness values of a given image is considered. According to the equation 3.1 haze removal is possible only when if we know the values  $\mathbf{I}$ ,  $\mathbf{A}$  and  $t$ . Value of  $\mathbf{I}$  is already given, it is hazy input image. Other parameters are calculated by using color attenuation prior technique.

First of all we have to calculate the value of  $t$  according to the equation 3.2. In that equation scene depth  $d(x)$  is calculated by using color attenuation prior.  $\beta$  is scattering coefficient value which is constant for homogeneous condition. In order to calculate the value of  $d(x)$ .

Here considered a linear model given in the equation 3.5. Linear model calculates the scene depth image using the linear coefficients and random error. In linear model saturation and brightness values are considered. To obtain saturation and brightness values convert RGB hazy image into HSV color space. Then saturation and brightness values are obtained. Using this values scene depth is calculated using linear model. This model has some parameters, these values learned by using supervised learning method. For the calculation of linear model more than hundred images are considered.

Depth obtained using linear model should be modified for further processing. Firstly, modify the raw depth image using median filtering operation to avoid misclassification results due to white objects. This resulted image further used for the calculation atmospheric light calculation. This same raw depth image then smoothed using Guided Image Filtering (GIM) [2]. This guided image filtering not only smoothens the raw depth image but also avoids blocking artifacts in image. Filtering output is linear transform of guidance image. For the calculation of guided image filtering two images are used one is input image and guidance image. Here input image is scene depth image and guidance image is another version of input image. That is input hazy image in this case is taken as guidance image.

Next aim is to calculate the value of atmospheric light. For that considers modified raw depth image. In that, finds the location in modified raw depth image that have 0.1 percent brightest pixel values. Then finds corresponding locations in the input hazy RGB image. From these locations finds the brightest pixel values in each color channel. For doing this inbuilt function sort is used. Three values corresponding to each color channels. These three values is consider as the atmospheric light values.

Now we have to calculate transmission map  $t$  by using the smoothed depth valued  $d(x)$  and  $\beta$  value. Calculation of smoothed depth value is already discussed. scattering coefficient matrix is generated according to the concentration of haze in the scene depth image. Calculation of the scattering coefficient matrix is based on the equation 3.11. In that equation  $C = 1.44$  is the fixed value and the constant value is 1.2. Finally, scene radiance is recovered by using the values of  $\mathbf{I}$ ,  $\mathbf{A}$  and  $t$ . These values are given to equation 3.13 to get haze free images. We can also use the equation 3.14. This equation more effectively remove noise from the image.

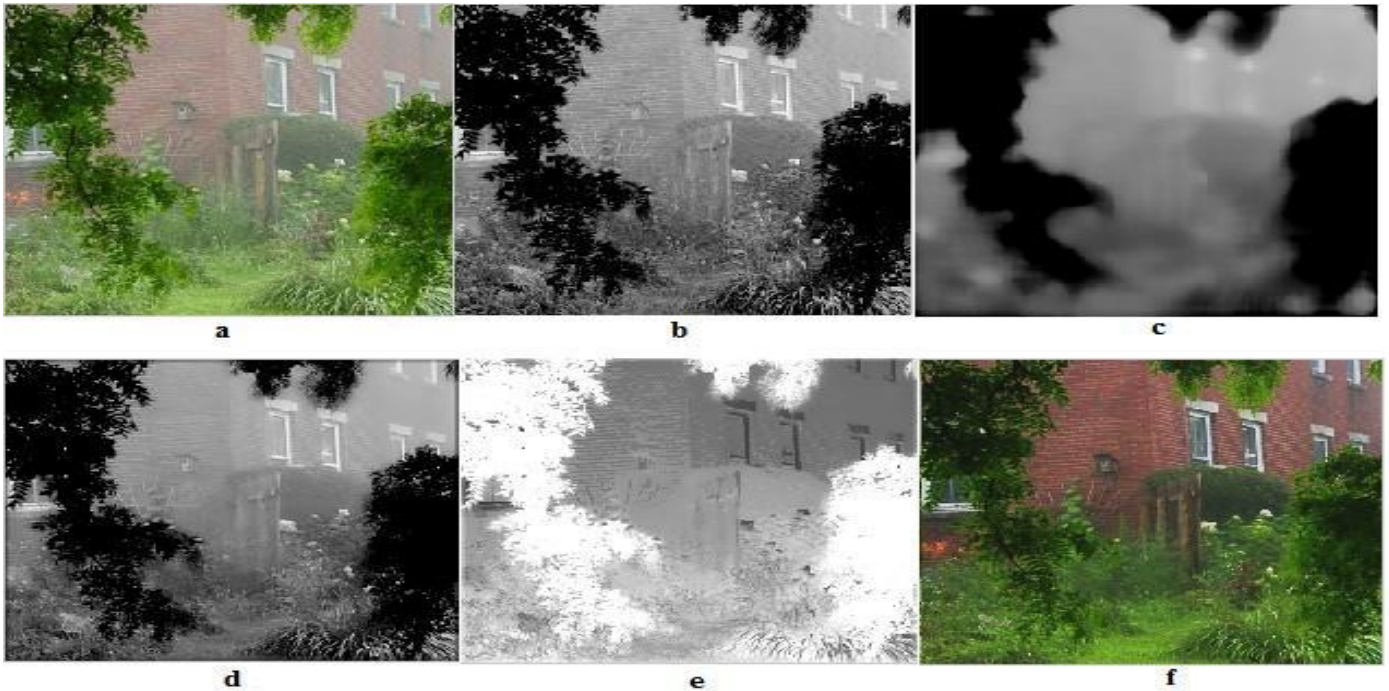


**FIGURE 3.1: RESULTS OF WORK:(A)INPUT HAZY IMAGE (B)RAW DEPTH IMAGE (C)MODIFIED RAW DEPTH IMAGE (D)SMOOTHENED DEPTH IMAGE (E) TRANSMISSION MAP (F) HAZE-FREE IMAGE**

#### IV. PERFORMANCE EVALUATION

In order to verify the effectiveness of the proposed dehazing method, we test it on various hazy images and compare with He et al.s [9], Tarel et al.s [19], Nishino et al.s [21] and quingsong [1] methods. All the algorithms are implemented in the MatlabR2013a environment on a I3 -3.30GHz PC with 4GB RAM. The parameters used in the proposed method are initialized as follows:  $r = 15$ ,  $\theta_0 = 0.121779$ ,  $\theta_1 = 0.959710$ ,  $\theta_2 = -0.780245$  and  $\sigma = 0.041337$ .

In order to quantitatively assess and rate the algorithms, we calculate the mean squares error (MSE)[1], the structural similarity (SSIM) [20] and peak signal to noise ratio (PSNR) are considered. Let as consider each performance evaluation in detail. The MSE of each result can be calculated by the following equation:

$$e = \sqrt{\frac{1}{3N} \sum_{c\{r,b,g\}} \|\mathbf{J}^c - \mathbf{G}^c\|^2} \quad (4.1)$$

Where  $\mathbf{J}$  is the dehazed image,  $\mathbf{G}$  is the ground truth image,  $\mathbf{J}^c$  represents a color channel of  $\mathbf{J}$ ,  $\mathbf{G}^c$  represents a color channel of  $\mathbf{G}$ ,  $N$  is the number of pixels within the image  $\mathbf{G}$ , and  $e$  is the MSE measuring the difference between the dehazed image  $\mathbf{J}$  and the ground truth image  $\mathbf{G}$ . Note that  $\mathbf{J}$  and  $\mathbf{G}$  have the same size since they are corresponding with the hazy image  $\mathbf{I}$ . Given  $\mathbf{J}$  and  $\mathbf{G}$ , a low MSE represents that the dehazed result is satisfying while a high MSE means that the dehazing effect is not acceptable.

The structural similarity (SSIM) image quality assessment index [] is introduced to evaluate the ability to preserve the structural information of the algorithms. A high SSIM represents high similarity between the dehazed image and the ground truth image, while a low SSIM conveys the opposite meaning. The luminance of the surface of an object being observed is the product of the illumination and the reflectance, but the structures of the objects in the scene are independent of the illumination. Consequently, to explore the structural information in an image, we wish to separate the influence of the illumination. We define the structural information in an image as those attributes that represent the structure of objects in the scene, independent of the average luminance and contrast. Since luminance and contrast can vary across a scene, we use the local luminance and contrast for our definition.

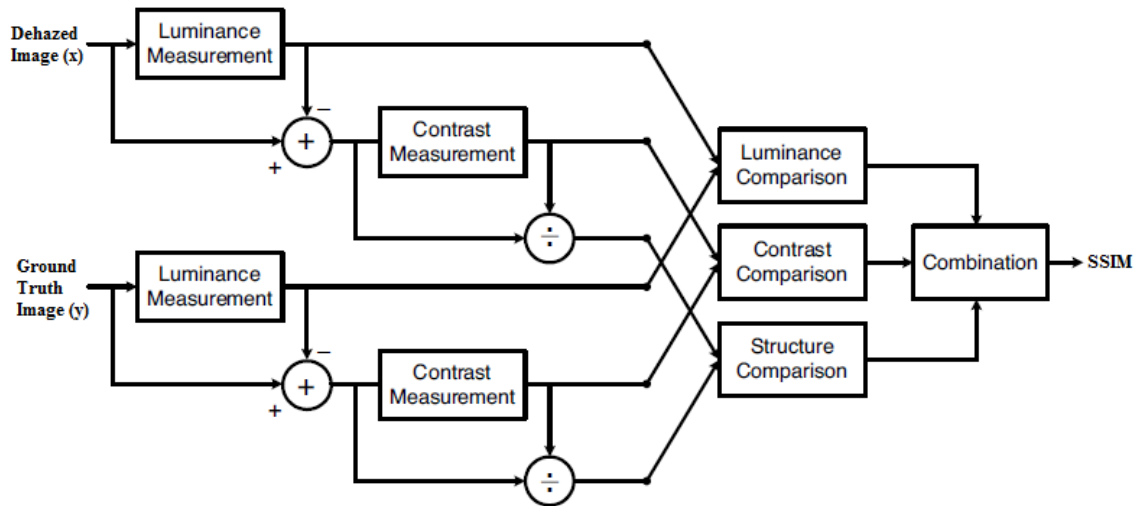


**FIGURE 4.1: DIAGRAM OF THE STRUCTURAL SIMILARITY (SSIM) MEASUREMENT SYSTEM.**

The system diagram of the proposed quality assessment system is shown in Fig.4.1. Suppose  $x$  and  $y$  are two nonnegative image signals, which have been aligned with each other (e.g., spatial patches extracted from each image). The system separates the task of similarity measurement into three comparisons: luminance, contrast and structure. Here we calculate structural similarity between dehazed image and ground truth image. The equation for the calculation of SSIM is given here as:

$$SSIM(x, y) = \frac{(2\mu_x\mu_y + C_1)(2\sigma_{xy} + C_2)}{(\mu_x^2 + \mu_y^2 + C_1)(\sigma_x^2 + \sigma_y^2 + C_2)} \tag{4.2}$$

If we consider one of the signals to have perfect quality, then the similarity measure can serve as a quantitative measurement of the quality of the second signal. In the above equation  $C_1$  and  $C_2$  are the constants. Its values are  $C_1=(0.01 * L)^2$  and  $C_2=(0.03 * L)^2$  (default values),  $L$  is dynamic range and its value is 255 (for 8-bit grayscale image).

The third quality assessment method is based on peak signal to noise ratio (PSNR). This value is calculated by using the results of MSE. If the PSNR value is high, then the dehazed image has close similarity with ground truth image. If its value is low, opposite effect is obtained. The equation for the calculation of PSNR value is given here as:

$$p = 10 * \log_{10} \left( \frac{256^2}{e} \right) \tag{4.3}$$

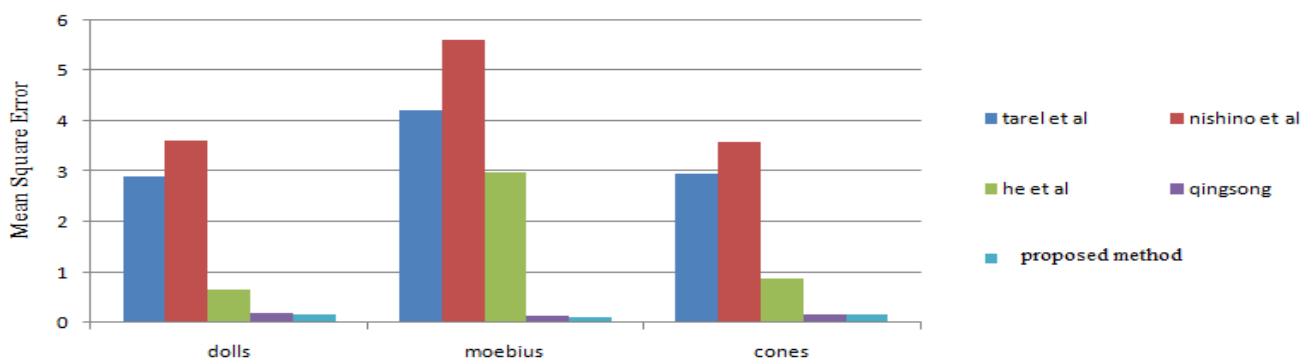


**FIGURE 4.2: MEAN SQUARED ERROR (MSE) OF DIFFERENT ALGORITHMS**

In the Fig. 4.2, we can see that a slight performance improvement in the cases of our method and previous method quingsong method. Both these method have MSE values less than one. Nishino et.al method have large MSE value, so it have less performance. He et.al method also have MSE value less one. It also shows better dehazing effects but its effect is less than our method according to MSE.



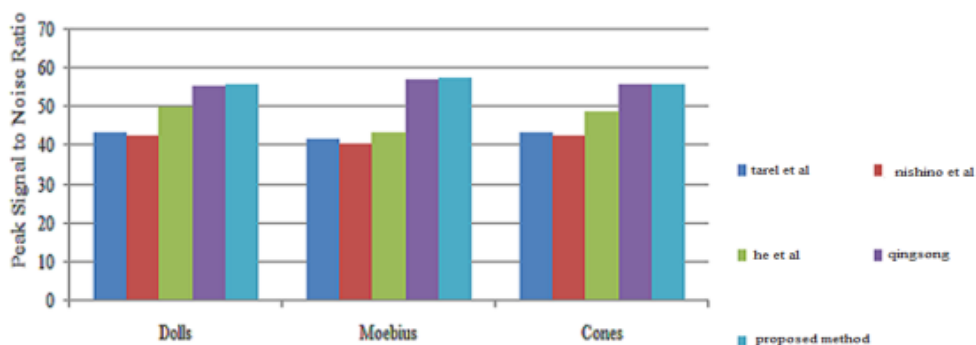


**FIGURE 4.3: PEAK SIGNAL TO NOISE RATIO (PSNR) OF DIFFERENT ALGORITHMS**

The Fig. 4.3 shows the comparison of different algorithm with our method based on PSNR values. From the figure, we can analyze that the PSNR values of our method and quingsong method are greater than fifty. But by close analysis we can find that our method is slightly better than quingsong method. Remaining methods have PSNR value less than our method.

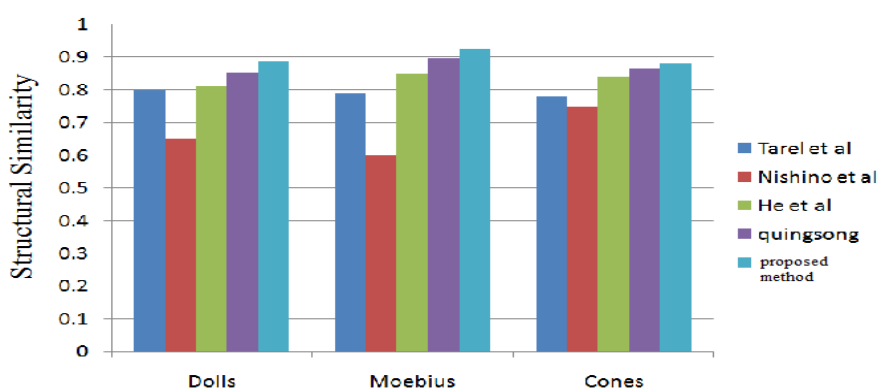


**FIGURE 4.4: STRUCTURAL SIMILARITY (SSIM) OF DIFFERENT ALGORITHMS**

The structural similarity also calculated for different algorithm with our algorithm in Fig. 4.4. By comparing the values three algorithms have SSIM values greater than 0.8. But our algorithm shows Structural Similarity values greater than 0.9. Nishino etal shows lower values for structural similarity. By comparing the values MSE, PSNR and SSIM values our algorithm shows better performance. In future, we can use this algorithm for removing haze from live video inputs. We can implement this algorithm in vehicles while travelling through the hazy hill stations.

Now we are going to qualitative comparison of different algorithm with our algorithm. This qualitative comparison also done on the basis of ground truth image. Fig. 4.5 shows the qualitative comparison different algorithms. From this figure we can say that 4.5 (d), 4.5 (e) and 4.5 (f) shows better performance which is very close to ground truth values.

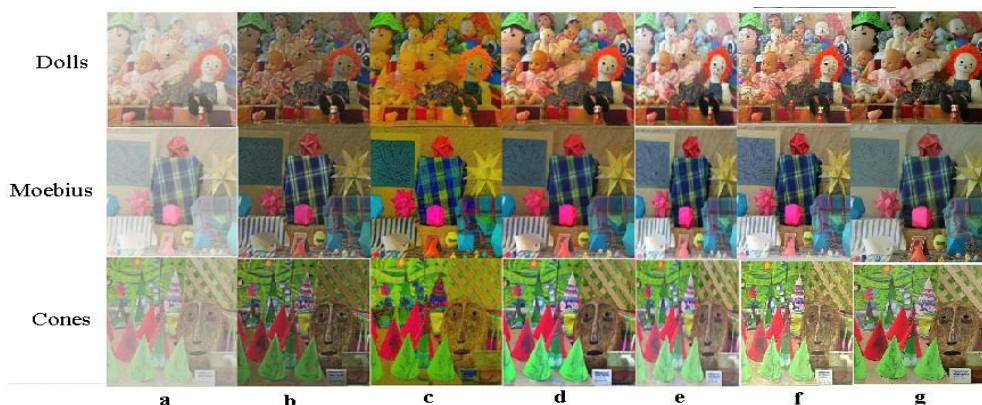


**FIGURE 4.5: QUALITATIVE COMPARISON: (a) Hazy images (b) Tarel et. al. s method. (c) Nishino et. al. s method. (d) He et al.s method. (e) quingsong method. (f) Proposed method. (g) Ground truth image.**

## V. CONCLUSION

In this paper, we have proposed a novel linear color attenuation prior, based on the difference between the brightness and the saturation of the pixels within the hazy image. By creating a linear model for the scene depth of the hazy image with this simple but powerful prior and learning the parameters of the model using a supervised learning method, the depth information can be well recovered. The scene radiance of the hazy image can be recovered easily. Very simple smoothing operations are required for getting modified scene depth image. Simple linear model equations are used for scene depth calculation and the required terms are recovered from the linear model and the scene recovery became easier. Equations for scene depth recovery are derived from the atmospheric scattering model. Instead of using fixed value scattering coefficient, a scattering coefficient matrix is generated. It can be used only for color images. Dense haze and fog cannot be removed by this method. This simple algorithm can be implemented effectively for outdoor images. Images used effectively. As a future work this algorithm can be extended to videos also and can also be used for vehicles travelling in foggy conditions.

## REFERENCES

- [1] Qingsong Zhu, Jiaming Mai, and Ling Shao, "A Fast Single Image Haze Removal Algorithm Using Color Attenuation Prior" IEEE Trans. On Image Processing, Vol. 24, no. 11, Nov 2015
- [2] K. He, J. Sun, and X. Tang, "Guided image filtering," IEEE Trans. Pattern Anal. Mach. Intell., vol. 35, no. 6, pp. 13971409, Jun. 2013.
- [3] K. Tang, J. Yang, and J. Wang, "Investigating haze-relevant features in a learning framework for image dehazing" in Proc. IEEE Conf. Comput. Vis. Pattern Recognit. (CVPR), Jun. 2014, pp. 29953002.
- [4] Y. Y. Schechner, S. G. Narasimhan, and S. K. Nayar, "Polarization-based vision through haze," Appl. Opt., vol. 42, no. 3, pp. 511525, 2003.
- [5] S. G. Narasimhan and S. K. Nayar, "Vision and the atmosphere," Int. J. Comput. Vis., vol. 48, no. 3, pp. 233254, Jul. 2002..
- [6] T. K. Kim, J. K. Paik, and B. S. Kang, "Contrast enhancement system using spatially adaptive histogram equalization with temporal filtering" IEEE Trans. Consum. Electron., vol. 44, no. 1, pp. 8287, Feb. 1998.
- [7] Y. Y. Schechner, S. G. Narasimhan, and S. K. Nayar, "Instant dehazing of images using polarization," in Proc. IEEE Conf. Comput. Vis. Pattern Recognit. (CVPR), 2001, pp. I-325I-332.
- [8] S. G. Narasimhan and S. K. Nayar, "Chromatic framework for vision in bad weather" in Proc. IEEE Conf. Comput. Vis. Pattern Recognit. (CVPR), Jun. 2000, pp. 598605.
- [9] K. He, J. Sun, and X. Tang, "Single image haze removal using dark channel prior" IEEE Trans. Pattern Anal. Mach. Intell., vol. 33, no. 12, pp. 23412353, Dec. 2011.
- [10] R. T. Tan, "Visibility in bad weather from a single image," in Proc. IEEE Conf. Comput. Vis. Pattern Recognit. (CVPR), Jun. 2008, pp. 18.
- [11] R. Fattal, "Single image dehazing" ACM Trans. Graph., vol. 27, no. 3, p. 72, Aug. 2008.
- [12] K. Tang, J. Yang, and J. Wang, "Investigating haze-relevant features in a learning framework for image dehazing," in Proc. IEEE Conf. Comput. Vis. Pattern Recognit. (CVPR), Jun. 2014, pp. 29953002.
- [13] L. Breiman, "Random forests," Mach. Learn., vol. 45, no. 1, pp. 532, Oct. 2001.
- [14] D. Scharstein and R. Szeliski, "A taxonomy and evaluation of dense two frame stereo correspondence algorithms," Int. J. Comput. Vis., vol. 47, nos. 13, pp. 742, Apr. 2002.
- [15] D. Scharstein and R. Szeliski, "High-accuracy stereo depth maps using structured light," in Proc. IEEE Conf. Comput. Vis. Pattern Recognit. (CVPR), Jun. 2003, pp. I-195I-202.
- [16] S. Shwartz, E. Namer, and Y. Y. Schechner, "Blind haze separation," in Proc. IEEE Conf. Comput. Vis. Pattern Recognit. (CVPR), vol. 2. 2006, pp. 19841991.
- [17] S. G. Narasimhan and S. K. Nayar, "Chromatic framework for vision in bad weather," in Proc. IEEE Conf. Comput. Vis. Pattern Recognit. (CVPR), Jun. 2000, pp. 598605.
- [18] S. K. Nayar and S. G. Narasimhan, "Vision in bad weather," in Proc IEEE Int. Conf. Comput. Vis. (ICCV), vol. 2. Sep. 1999, pp. 820827.
- [19] J.-P. Tarel, N. Hautire, L. Caraffa, A. Cord, H. Halmaoui, and D. Gruyer, "Vision enhancement in homogeneous and heterogeneous fog," IEEE Intell. Transp. Syst. Mag., vol. 4, no. 2, pp. 620, Apr. 2012.
- [20] Z. Wang, A. C. Bovik, H. R. Sheikh, and E. P. Simoncelli, "Image quality assessment: From error visibility to structural similarity," IEEE Trans. Image Process., vol. 13, no. 4, pp. 600612, Apr. 2004.
- [21] K. Nishino, L. Kratz, and S. Lombardi, "Bayesian defogging," Int. J. Comput. Vis., vol. 98, no. 3, pp. 263278, Jul. 2012.

# Switching System, a Zero Power Standby Solution

## Stefan Mozar FIEEE<sup>1</sup>, Nobuo Funabiki<sup>2</sup>

Department of Electrical and Communications Engineering, Okayama University, Japan

**Abstract**— *This paper describes a novel standby system. The actual power consumption in standby mode is zero Watts. In this standby system the appliance is completely disconnected from it mains supply during standby mode. In addition from saving on electricity costs, it also has the added benefit of preventing hazardous situations whilst in standby mode. This novel standby system will set a new goal for manufacturers of consumer products to achieve.*

**Keywords**— *Energy efficiency, energy harvesting, green design, standby, zero power.*

### I. INTRODUCTION

Standby power is a major concern for power companies, and for consumers. Consumers are becoming aware of how much it costs to have appliances in standby. Governments have introduced energy rating labels on products. Standby goals and guidelines are produced by minimum performance standards (MEPS) for a number of different products. The International Energy Agency (IEA) has started the "One Watt Initiative" which aims to reduce standby power to not more than 0.5W. In order to have a common way of measuring standby power, IEC standard 62301 was developed. The challenge is how to reduce standby power. A number of different techniques have been developed. This paper will describe a "standby" solution which achieves zero power consumption. With this new system, the appliance is completely disconnected from the mains supply, when switched off by remote control. Once switched off the remote control can be used to the appliance on again.

### II. BENEFITS OF THE NEW STANDBY SYSTEM

The obvious benefit of this system is that no power is drawn during what would be called "standby". In this mode the appliance is completely disconnected from the mains supply. Thus there is complete isolation from the mains supply. With current technology about 10% of household electricity is used for standby. That means 10% of a household energy bill is wasted. With increasing energy costs, that is a potential for saving. More importantly than saving is the environmental impact due to wasted standby energy. Thus reducing energy that is waste from standby has a big impact on society.

Having the appliance completely disconnected from the mains supply has another advantage. It is safety. An appliance that is in active or standby mode can through a fault condition become unsafe. Data collected on household fires shows that about 17% of domestic fires in Tokyo are due to faulty consumer products. In Germany the figure is 30% of household fires. In Germany top of the list appliances that contribute towards household fires are washing machines and dryers. Safety issues of consumer product are in the news frequently. The ability to isolate an appliance from the mains helps improve safety and reduces the electricity bill. A further benefit of the proposed system is the low cost to implement it. Cost is a critical factor in consumer electronics.

### III. REVIEW OF STANDBY INNOVATIONS

Many studies have been done on the energy wasted in households by standby. Mohanty [6] has done such a study, which highlights the wasted energy due to products being in standby mode. The studies not only show the energy waste in consumer households, but they also include standby energy consumption in offices.

In early consumer products, standby systems just disconnected high power loads from the power supply. In standby the product had to appear to be switched off. For example a TV set had a dark screen, and no sound. To indicate the set is in standby mode, some form of indication was used. Typically a LED was lit up. In these systems the main power supply was live in standby, with a reduced load. Flyback power supplies perform poorly under low load conditions and have very low efficiency. Typical standby power consumption has been 30W and upward, depending on the type of appliance and its total power rating.

Flyback power supplies are the most common topology used in consumer applications. This is because of their simplicity, and lower component count compared to other topologies, and they can have multiple isolated secondary supplies. The disadvantage of flyback supplies is their poor efficiency under low load conditions. For consumer products with higher power demands the inefficiency of the power supply is significant. In standby mode the only load are the microprocessor and the standby components. These draw very little power. The losses in such a supply can be higher than the prescribed newer

standby requirements. The solution was to use a second, smaller auxiliary power supply for standby. The smaller supply is more efficient than the main supply at low power. This solution resulted in a significant reduction in standby power, but it added extra cost which can only be justified in high end products. The power consumption of such circuits would go down to one or two Watts.

Burst mode, also known as pulse skipping technology was the next step in standby evolution. When the load is reduced as is the case with standby mode, the switching frequency of the power supply is changed. In normal operation the switching frequency is high and the switching transistor is on for most of the time. In standby mode, less energy needs to be supplied to the load, so the switching frequency is dropped, and the switching transistor is off for most of the time. The skipping of switching pulses (burst mode) reduces the switching losses and thus increase the low load efficiency. This is shown in the fig. 1 below.

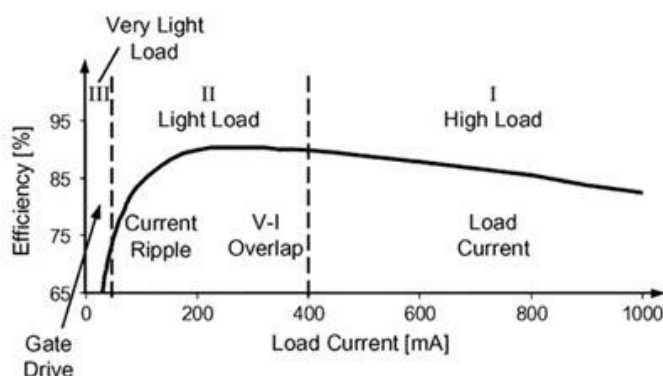


**FIG. 1. EFFICIENCY VERSUS LOAD CURRENT [12]**

During burst mode the losses are in the startup up circuit, the losses in the switching device, and power losses in the control IC circuit, and hysteresis losses in the transformer.

Lower the switching frequency requires a number of design tradeoffs. Reducing the switching frequency, reduces the losses in the switching device, but it may result in poor regulation of the output voltage. The low switching frequency may result in audible noise. The noise level can be reduced by limiting the peak switching current. This in turn reduces the supply efficiency. Thus the designer must find a balance between noise and efficiency.

As microprocessors became available with a sleep mode which would reduce the micro's energy consumption to micro Watts, new standby concepts were proposed [7]. Generally these were able to achieve very low power consumption levels. This led to the development of a variety of new approaches for standby mode. Many of these that were published by academic researchers had practical limitations. Many have proposed the use of solar panels as a standby supply, thus claiming zero power standbys. But these methods still consume power in standby. They don't draw current from the mains supply. Given the requirements of a product that consumers will buy, these solutions fall short, as they have many unsolved problems. For example what if there is no light, and then their standby system will not work. They also have not included solutions for safety, and interference issues. Thus their concept models are often not practical and too expensive.

#### IV. SWITCHING SYSTEM

The zero power solution to be described has the following advantages:

- It does not require any internal power source to operate.
- It disconnects the appliance from the mains supply
- It is safer in "Standby mode"
- It can help improve Electro Magnetic Interference (EMI)

This standby solution is actually an on-off switch; therefore the patent for this invention describes it as a switching device. This is a more accurate name, than standby. Standby has been used in this paper, as it makes it easier to understand the function of this system. The aim of this system is to use a remote control to switch an appliance, like a TV set, on or off. A

conventional standby system needs internal power to be able to receive the Infra-Red (IR) signal from the remote control transmitter. This new system does “energy harvesting” from an RF signal that is emitted from the remote control transmitter. The signal transmitted is in the unlicensed frequency band. A block diagram of the proposed system is shown in fig. 2.

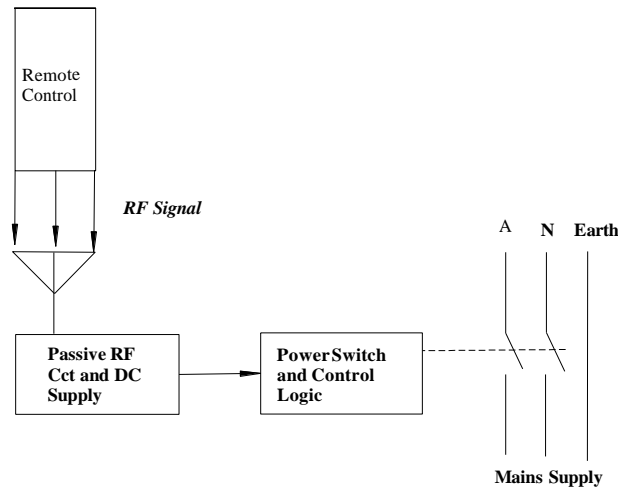


**FIG. 2. SWITCHING SYSTEM BLOCK DIAGRAM**

The system consists of an antenna which is connected to a passive RF module that rectifies and filters the received signal. The voltage obtained from this signal is then used to activate an electronic switch, which in turn connects the appliance to the mains supply. Thus this system does not have a standby mode. It only has two states, on or off. This is shown in the state diagram of figure 3 below. The conventional standby system has three states, compared to the two states of the switching system. This system also isolates the appliance from the mains supply in the off state, thus contributing to safer operation.

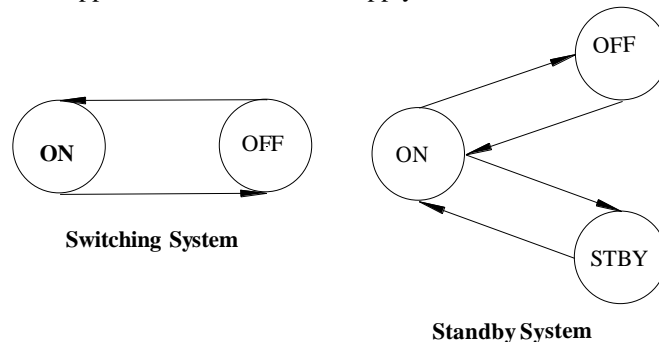


**FIG. 3. STATE DIAGRAM**

**V. SWITCHING CIRCUIT DESIGN CONSIDERATIONS**

This section provides an overview of some of the design considerations and issues.

**5.1 RF Frequency Selection**

The first consideration is the frequency selection. A frequency needs to be chosen that falls in the unlicensed bands. Choice of the frequency affects the antenna size. The size of the antenna is determined by equation (1).

$$\lambda = \frac{c}{f} \tag{1}$$

Where  $c$  = wave velocity ( $3 \times 10^8$  m/s)  
 $f$  = frequency in Hz  
 $\lambda$  = wavelength in m

The Frequency determines energy required to transmit the on/off signal to the appliance, which in our example is a TV receiver. The energy drops at the rate of the cube of the distance. The trade-offs in the frequency selection are:

**5.1.1 Frequency Selection**

A low frequency will require a larger antenna, and if data transmission is to be by RF, it may result in too slow data

transmission. If the frequency is higher it will require more energy for a given distance than a lower frequency.

**5.1.2 RF or IR**

In its simplest form the RF signal may only be used for the on-off function, and the other remote control functions may continue to be performed by an Infra-Red system (IR). For either choice the RC-6 or other existing protocols can be used.

**5.1.3 Passive RF Stage**

The switching system is not connected to any power, when switched off (or in “standby mode”). The only energy source is the transmitted RF signal from the remote control transmitter. It needs to be converted in to a DC voltage. Figure 4 show the basic circuit that will generate the DC voltage. The RF signal is rectified and its energy is stored in a capacitor. In order to get a large enough voltage to activate the switch, the following must be done.

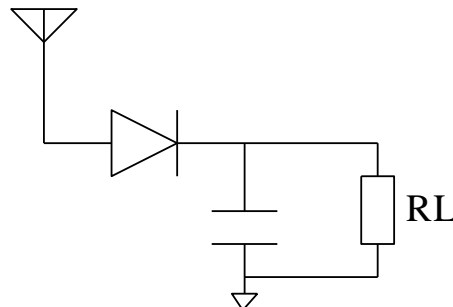


**FIG. 4. PASSIVE RF CIRCUIT**

**5.2 Voltage Magnification Factor**

There are number of tradeoffs to make in order to supply the switching circuit with an initial startup voltage. The proper selection of components allows the Q of the input circuit to produce a larger voltage to the input of the electronic switch.

$$Q = \frac{f}{BW} \tag{2}$$

From equation 2 we can see a relationship that can be used to determine the voltage multiplication factor of the input circuit. In our design we used 900 MHz, which is in the unlicensed band in most countries. The bandwidth in this band (860 MHz to 960 MHz) is 100 MHz. This gives a Q of about 9 to 10. At 900 MHz, the cycle time T is 1.1ns. The load resistance can be calculated based on the voltage we need to drive the switch and the current or power requirement. This resistance is the load (R<sub>Load</sub>). As a rule of thumb, the time constant τ to uphold the supply should be about 100 μs at this frequency. From this the filter capacitor can be calculated by equation 3.

$$C = \frac{\tau}{R_{Load}} \tag{3}$$

If the RF circuit is also to be used for data reception, then a second circuit is required. One path of the circuit will be required to supply DC voltage. Here a larger capacitor will be required to store the required energy for the switch to operate. The second path needs to be able cope with data signals. Therefore a separate circuit is used for the data path. Here a smaller filter capacitor is used. The concept of this circuit is shown in figure 5.

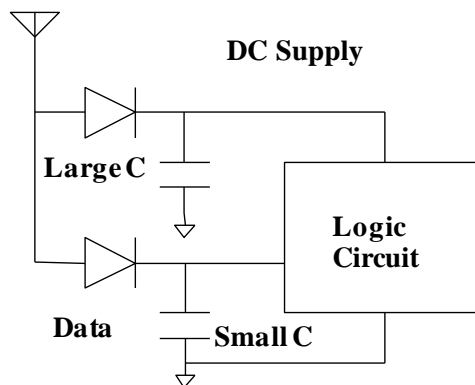


**FIG. 5. RF CIRCUIT FOR DC SUPPLY AND DATA RECEPTION**

### 5.3 The use of a Voltage Doubler

A voltage of about 1V is need to drive the switch. Although the input circuit Q factor will help, a charge pump, also known as voltage doubler, may be needed. Figure 6 shows the circuit of the doubler. The voltage can be scaled by adding one or more stages to the voltage doubler. It must be noted that we cannot just add n multipliers to obtain a desired voltage. The energy that can be extracted from the RF signal is limited by the signal strength. The signal must supply enough energy to overcome the diode voltage drops.

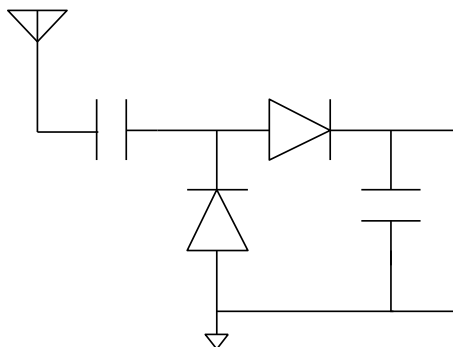


FIG. 6. VOLTAGE DOUBLER CIRCUIT

### 5.4 Switching System

#### 5.4.1 Mains Switch

The mains switch can be implemented with a variety of devices that are compliant to IEC 65. For appliances that consume 35 W or more, a mains switch must be used. Below 35 W, the switch is optional.

#### 5.4.2 Solid State Switch

The choice for a switch can be a solid state device such as a SCR or Triac. Using these devices extra components will be needed to meet the safety requirements. A further consideration is that devices will need to have noise suppression components so that false triggering won't occur. They will also contribute towards an increase in EMI. Very large noise spikes may also affect the performance of an electronic switch.

#### 5.4.3 Mechanical Switch

A mechanical switch can be used. In this application, a mechanical switch can be placed at a location in the receiver, where the mains cable layout will result in minimal EMI pickup. A relay may also be used as an electro mechanical switch. This is easy to control with a simple transistor that can handle the latching and holding currents. The circuit controlling the relay will need to be compliant with all safety standards as specified in IEC 65. This generally results in extra components to prevent safety issues under fault conditions. A relay has an advantage that the switching noise is audible. This noise can be good feedback that the appliance is changing state, i.e. from on to off or vice versa. An optical indicator of whether the appliance is drawing current from the mains supply needs to be included in the circuit.

### 5.5 Control Logic

The appliance needs to be able to distinguish between valid signals and keep track of several functions associated with switch control. As the signal is RF and disperses, it may be that a command is received from another appliance that is located close by. The circuit needs to be able detect if it is a valid signal that has arrived. These type of logic control functions can be implemented in hard or software.

### 5.6 Safety Issues

The switching system designed was for a TV receiver, thus IEC 65 was used as a reference for safety issues. As the circuit interfaces with high energy parts, safety tests will need to be done. The actual solutions to ensure a safe design, will depend on the method used to disconnect from the mains supply.

The switching device has a number of benefits regarding safety. In the OFF Mode, the appliance is completely disconnected from the mains supply. This is in contrast to current standby systems, where the appliances are always connected to the mains supply. Being disconnected makes the appliance safer.

## VI. CONCLUSION

The switching circuit has many advantages over current standby systems. Its greatest advantage is that it is an on-off system. Unlike other standby solutions, it is completely isolated from the mains supply when the appliance is not in use. The appliance can be switched on or off from the comfort of one's armchair, with the aid of a remote control unit. Other benefits are that no energy is consumed in the off state, and that some of the implementations, if designed correctly will result in better EMI performance, and it will make the appliance safer. A benefit of switching the appliance off is that the micro controllers and system busses get reset on power on. This standby solution is cost effective, reliable, and improves safety.

## ACKNOWLEDGEMENTS

The authors would like to acknowledge the support of their families. Without the support of our wives Choo and Naomi, and our children Christine, Mina, Yuya, and Ryoji we would not have been able to complete this project and many others.

## REFERENCES

- [1] Huang B.T., Lee K.Y., Lai Y.S., 2007, Design of a Two-Stage AC/DC Converter with Standby Power Losses Less than 1W, IEEE Power Conversion Conference, Nagoya, 2007, Pages 1630-1635.
- [2] Kang S., Park K., Shin S., Chang K., Kim H., 2011, Zero Standby Power Remote Control System using Light Power Transmission, IEEE Transactions on Consumer Electronics Vol.57, No. 4, November 2011, Pages 1622-1627.
- [3] Kim M.S. et al, 2013, Advanced Burst Mode of Control to Reduce Standby Power of Flyback Converter, Scientific Research, Engineering 2013, 5, pages 137-141.
- [4] Lee BH, Moon GW, 2013, Zero No-Load Power AC/DC Adapter for Electronic Equipment With Embedded Battery, IEEE Transactions on Power Electronics Vol.28, No.7, July 2013.
- [5] Madigan M., 2006, Green-Mode Power by the Milli-Watt, Texas Instruments Power Supply Design Seminar SEM1700, Topic 2, TI Literature Number: SLUP290.
- [6] Masswood A.I., Yoong Z.K., 2008, Switching Loss Reduction Through Digital Burst Technique in TV Power Supply, IEEE Industrial Electronics Magazine, September 2008.
- [7] Mohanty B, 2001, Standby Power Losses in Household Electrical Appliances and Office Equipment, The French Agency for the Environment and Energy Management (ADEME).
- [8] Mozar S. 2000, Intelligent Standby Concept, IEEE Transactions on Consumer Electronics, Volume: 46, Issue: 1, Feb 2000, Pages 179-182.
- [9] Mozar S, Switching System, US Patent 7911087, March 22, 2011.
- [10] Taranovich S., 2017, The Next Best Power Management Solution to Zero Power in Nano Power, EDN Network 2017 March 14.
- [11] Tsai C.H., et al, 2010, Design and Implementation of a Socket with Zero Standby Power using a Photovoltaic Array, IEEE Transaction on Consumer Electronics, Vol.56, No.4, November 2010, pages 2686-2693.
- [12] <http://electronics.stackexchange.com/questions/285029/the-meaning-of-burst-mode>.



# Kinetic modeling of Immobilized Yeast Batch Fermentation

Terkida Prifti (Vaso)<sup>1</sup>, Luljeta Pinguli<sup>2</sup>, Ilirjan Malollari<sup>3</sup>

Department of Industrial Chemistry, Faculty of Natural Sciences, University of Tirana, Tirana, Albania

**Abstract**— The main purpose of this study was to choose the best model that will be further refined and used for controlling batch fermentation process using immobilised yeast cell in order to increase its productivity. This study investigated the immobilized *Saccharomyces Carlsbergensis* growth kinetics, ethanol productivity and substrate consumption (glucose) using computer simulation for different kinetic models, Monod, Contois, Teisser and other models which present the substrate and product inhibition. Batch fermentations take place with different cell density comparing immobilized yeast fermentation performance with free yeast. For each batch were evaluated kinetic parameters and after mathematical models. We have used three linearization models for estimation of kinetic parameters. Conclusions about the influence of cell immobilization on the fermentation performance were drawn based on analysis of the obtained model parameters. It was found that in some fermentation Monod and Teisser models were the most appropriate. For substrate and product inhibition the most approximate models were exponential.

**Keywords**— Immobilization, inhibition, kinetic parameters, linearization, modeling.

## I. INTRODUCTION

The environmental problems caused by the use of fossil feedstock as an energy source and the rapid increase of the oil based fuels prices are the main reasons that have motivated the production of bio-fuels. Bio-ethanol, being a clean, safe and renewable resource, has been considered as a potential alternative to the ever decreasing fossil fuels. Ethanol production has increased dramatically during the last years, because it is considered as a renewable and environmentally friendly alternative. However, the economic feasibility of the ethanol industry is still questioned and much effort should be put into improving the process, especially resistance to the main inhibition factors.

To eliminate inhibition caused by high concentrations of substrate and product as well as to enhance yield, cell immobilization approaches have been applied in ethanol production. The advantages of immobilized cell over free cell systems have been extensively reported. Immobilized cell fermentation has been shown to be more effective than the free yeast process, mainly due to the enhanced fermentation productivity, feasibility for continuous processing, cell stability and lower costs of recovery and recycling and downstream processing. However, immobilized cells still have limited industrial application. The process of immobilization changes not only the environment, but also the physiological and morphological characteristic of cells, and the catalytic activity of enzymes. Therefore the fermentation conditions (kinetics) of the free yeast fermentation and of the immobilized cell process are different.

Simulation investigations are proven to be powerful tools for evaluating the fermentation processes alternatives that decrease spending of expenses on pilot experiments. The quality of the simulation itself depends on the quality of the underlying mathematical model used for prediction of the responses of a given system to changes in environmental and operating conditional. Hence the mathematical models should describe with sufficient accuracy the mechanisms of the processes under consideration. For the purpose of bioprocesses simulation, kinetic models based on mass balance of the main compounds in the bioreactor. Modeling batch fermentation process by the yeast *Saccharomyces Carlsbergensis* immobilized in Na-alginate gel beds were considered. They describe the main factors affecting the glucose concentration – substrate and product inhibition, but none of them can account simultaneously for all of these factors. However there is no model universal structure that could perfectly suit glucose fermentation by all possible kinds of strains since each particular strain has its specifics that require an individual approach to kinetics modeling.

The aim of our study was to carry out a comparative analysis of different mathematical structures known by far for modeling of batch alcoholic fermentation with free and immobilized cells of *Saccharomyces Carlsbergensis* using real experimental data. The two types of processes (with free and immobilized cells) were compared with respect to the main model parameters that determine the main interactions in the culture – inhibition and transformation of sugar to ethanol and biomass. Conclusions were drawn about the influence of cell immobilization on the batch process. The main purpose of this study was to choose the best model that will be further refined and used for control synthesis of the process in order to increase its productivity.

## II. MATERIALS AND METHODS

The equipment consists in eight conical bioreactors (vessels) 250ml, where was placed the immobilized yeast with the entrapment method and free yeast, in respective amount 1 and 2 g/l. For yeast cell immobilization solution of Na – alginate was used. It was prepared by dissolving alginate in distilled water at constraint stirring until a homogeneous solution was obtained. The immobilization has been carried out by cells inclusion into the alginate matrix, respecting the entrapment method. The following diameters of the biocatalyst spherical particles have been obtained: 4, 5.3 and 7 mm. The fermentations have been carried out until a constant amount of glucose was taken, at the ambient temperature.

On average, every four hours was carried out measurements for determining the amount of glucose consumed and the amount of yeast which released for each samples. Measurements were carried out through the refractometer and the spectrophotometer (in 550nm).

### 2.1 Mathematical models

We chose simplified mass balance mathematical models that reflect only the kinetic rates of the main process reactions: biomass growth, ethanol production and substrate consumption for biomass and product formation.

The fermentation process kinetics was described with the ordinary differential equation:

$$\begin{aligned}\frac{dX}{dt} &= \mu X \\ \frac{dP}{dt} &= qX \\ \frac{dS}{dt} &= - \frac{1}{Y_{X/S}} \frac{dX}{dt} = - \frac{1}{Y_{P/S}} \frac{dP}{dt}\end{aligned}\quad (1)$$

Where X was biomass concentration, P is ethanol concentration, S substrate concentration,  $Y_{X/S}$  and  $Y_{P/S}$  were yield coefficients,  $\mu$  and  $q$  were specific growth and product accumulation rates.

The main kinetic parameters are:

- Maximal specific growth rate  $\mu_{max}$ ,
- Monod constant,  $K_s$  value is the concentration of substrate when  $\mu$  is equivalent to half of  $\mu_{max}$
- The inhibitor constant,  $K_i$  is an indication of how potent an inhibitor is, it is the concentration required to produce half maximum inhibition.

In these researches are used these models:

- Monod

$$\mu = \mu_{max} \frac{S}{S + K_s} \quad (2a)$$

- Contois

$$\mu = \mu_{max} \frac{S}{K_s * X + S} \quad (2b)$$

- Teisser

$$\mu = \mu_{max} \left( 1 - \exp\left(- \frac{S}{K_s}\right) \right) \quad (2c)$$

- Substrate inhibition

$$\mu = \mu_{max} \frac{S}{S + K_s} \exp\left(-\frac{S}{K_i}\right) \tag{2d}$$

- Product inhibition (Aiba)

$$\mu = \mu_{max} \frac{S}{S + K_s} \exp(-K_i * p) \tag{2e}$$

Three linearization methods were used to determine  $\mu_{max}$  and  $K_s$ , which are:

- Lineweaver – Burk

$$\frac{1}{\mu} = \frac{K_s}{\mu_{max}} \frac{1}{S} + \frac{1}{\mu_{max}} \tag{3a}$$

- Hans Woolf

$$\frac{S}{\mu} = \frac{1}{\mu_{max}} S + \frac{K_s}{\mu_{max}} \tag{3b}$$

- Eadie Hofslee

$$\mu = -K_s \frac{\mu}{S} + \mu_{max} \tag{3c}$$

And the one with the highest correlation coefficient was chosen, and  $K_i$  was determined by the mathematical method trial and error.

### III. RESULTS AND DISCUSSION

The system differential equations (1) are a classic description of various biotechnological processes. We tested 12 mathematical models obtained by different authors and applied for different biotechnological processes. The careful analysis of that work and our experimental results restricted our choice to 5 of these 12 mathematical models. For some of the discarded models unusual and unexplained constant values, even from a biological point of view, were obtained, while in other models it was impossible to identify the parameters. The mathematical models chosen as a result of the pre-selection are listed: equation (2a) – (2e). The obtained parameters kinetic for all the investigated models are given in Table 1.

**TABLE 1**  
**IDENTIFIED MODEL PARAMETERS**

	Immobilized cell	$\mu_{max}$ 1/ore	$K_s$ °Brix	$K_i$ °Brix	$Y_x/s$ -	$Y_p/s$ -	$R$ %
Fermentation 1	4mm	0.593	12.01	-	0.0011	0.5	97.6
	7mm	0.385	10		0.0023	0.5	66.3
	Free cell	0.711	14.413		0.0988	0.5	89.3
Fermentation2	4mm	0.471	20.94	104.7	0.0117	0.5	93.8
	7mm	0.406	22.94	114.7	0.0127	0.5	97.4
	Free cell	0.384	24.894	124.47	0.0669	0.5	91.6
Fermentation 3	4mm	0.321	22.794	113.965	0.010099	0.5	95.17
	7mm	0.412	27.629	138.145	0.013409	0.5	87.58
	Free cell	0.208	23.637	118.19	0.062401	0.5	95
Fermentation 4	4mm	0.135	14.79	0.1	0.0143	0.5	98.3
	7mm	0.167	0.613	0.006	0.0217	0.5	80.7
	Free cell	0.11	18.84	0.18	0.1148	0.5	97.1
Fermentation 5	4mm	0.009	12.37	0.12	0.0059	0.5	99.9
	7mm	0.011	12.51	0.12	0.0064	0.5	99.6
	Free cell	0.00008	12.3	0.12	0.1975	0.5	99

Figure 1. shows the model simulation result comparison with experimental data for the specific growth rate modeling equation. As seen, all the identified models describe with relatively good accuracy the batch fermentation process in the both cases (with and without cell immobilization). In order to choose the best model, it is important to consider how well it fit experimental data with Monod model.

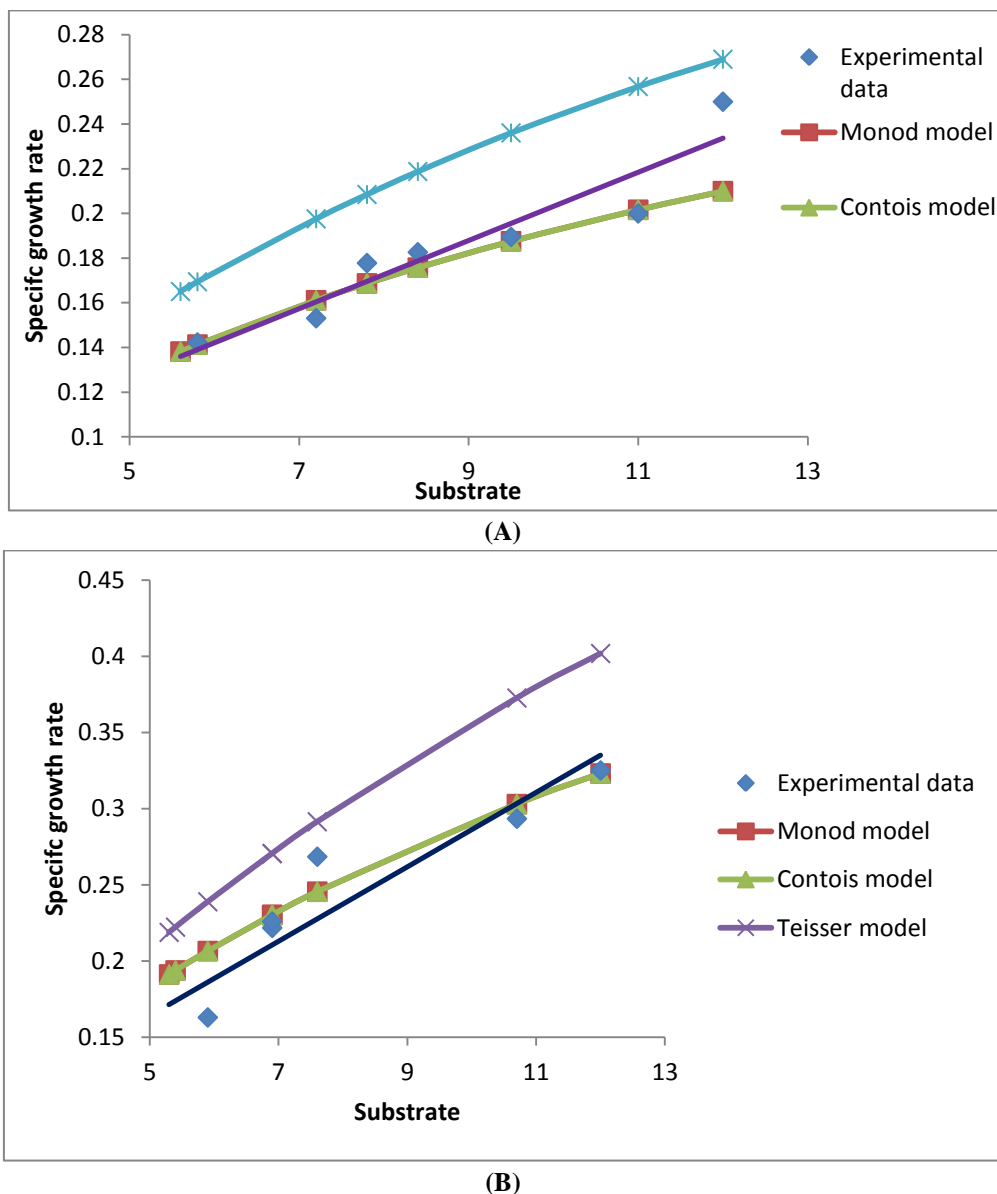


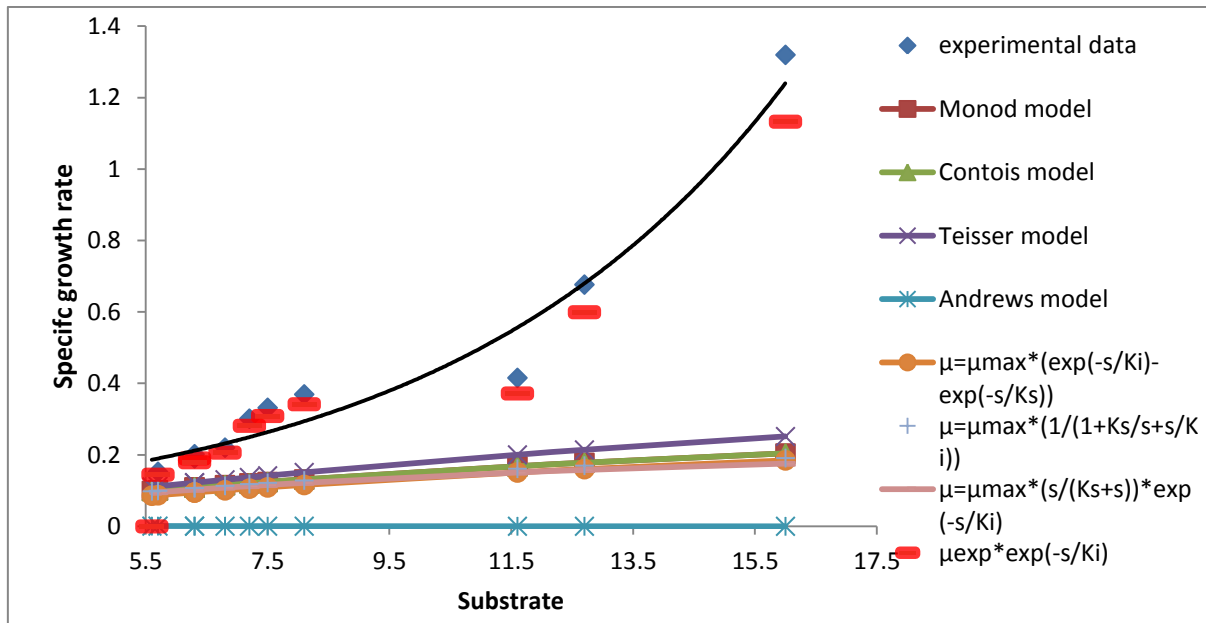
**FIG. 1. COMPARISON OF MATHEMATICAL MODELS FOR SPECIFIC GROWTH RATE IN THE CASES OF IMMobilized CELL (4 mm) (A) AND FREE CELLS (B), IN THE FIRST FERMENTATION.**

Looking at Fig. (1b) we can conclude that in the case of free cell fermentation the model of Teisser do not fit in comparison to the rest of the rest of the models. In the case of the free cell fermentation, we have high values of the parameters  $K_s$  and  $Y_{X/S}$ . In low cell density Monod and Contois model fit well with experimental data, whereas in high cell density experimental data do not fit with any models.

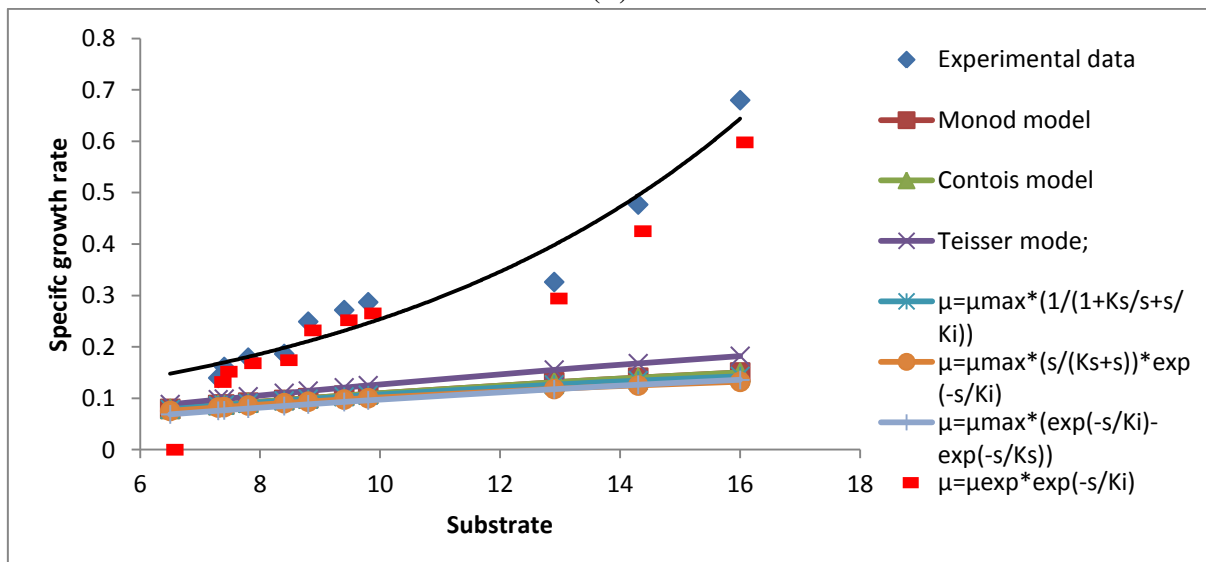
A similar analysis can be done for the models of the second case of immobilized cell fermentation, Fig. 1a. Since immobilized cells growth inside beads pearls, they are restricted by diffusion resistances and have a lower maximum specific growth rate. The decreasing of the specific growth rate is due to the internal diffusion resistances rather than due to the external ones because the process is carried out with intensive stirring and hence the main resistance is due to the substrate diffusion through the alginate pores. In that case the models have lower value of  $K_s$  in comparison with those for the free cell fermentation. This could be explained with higher concentration of viable yeasts cells in the bioreactor working volume.

In Fig. 2. are given comparison of the mathematical models, in case of substrate inhibition.

Fig. (2a) shows cell immobilized (4mm) and we see that Monod, Contois and Teisser models do not fit at all with experimental data. From the results obtained fit the equation (2d), which has an exponential dependence. In this case we have the impact of the inhibition constant  $K_i$ , that reduces the maximum specific growth rate and increases the semi saturation constant  $K_s$ . In the Fig. (2b) performance is shown for the free cell fermentation and it also has an exponential dependence, due to the substrate inhibition maximum specific growth rate decrease more and the semi saturation constant  $K_s$  and inhibition constant  $K_i$  increase even more.



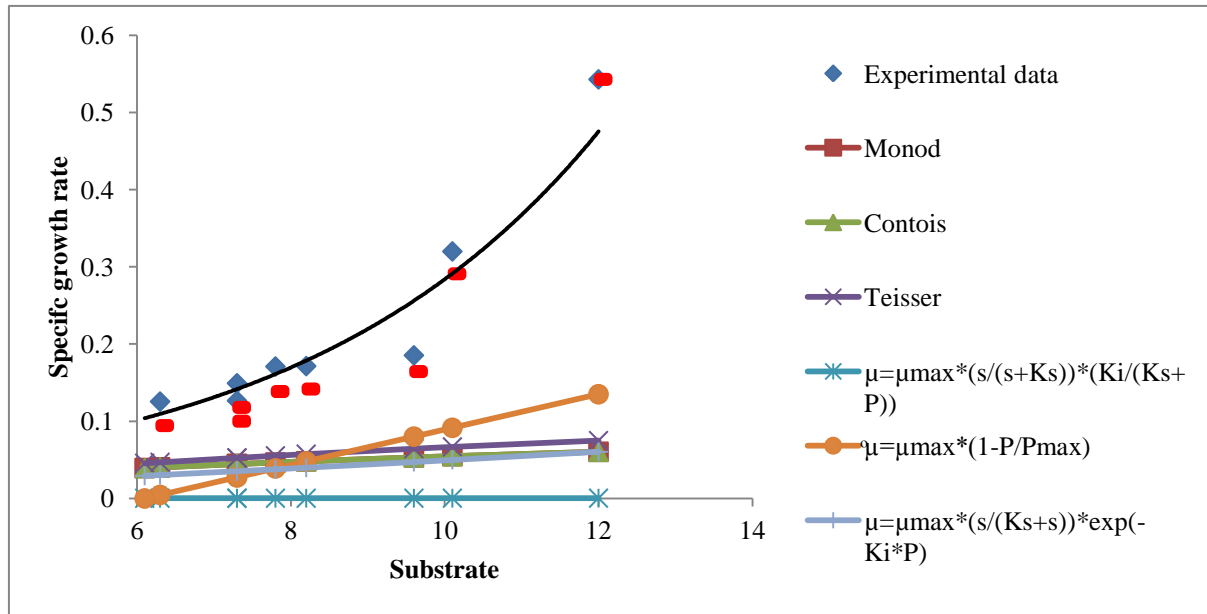
(A)



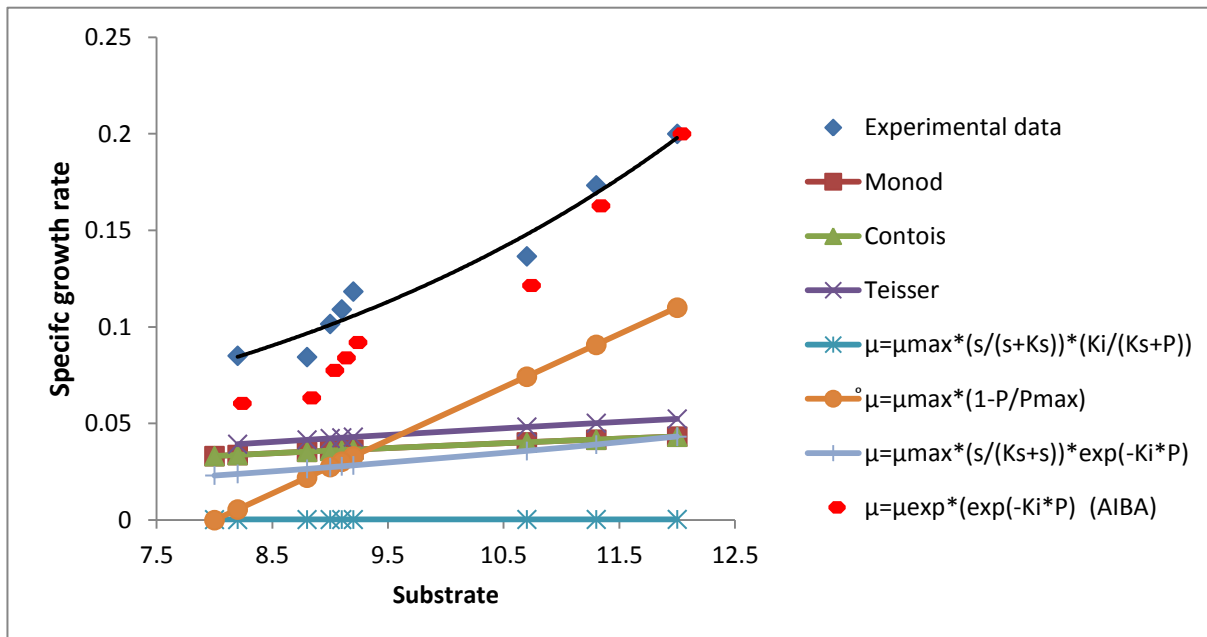
(B)

**FIG. 2. COMPARISON OF MATHEMATICAL MODELS FOR SPECIFIC GROWTH RATE IN THE CASES OF IMMOBILIZED CELL (4 mm) (A) AND FREE CELLS (B), IN THE SECOND FERMENTATION.**

In Fig. 3. are given comparison of the mathematical models, in case of product inhibition. Fig. (3a) shows cell immobilized (4mm) and Monod, Contois and Teisser models are far from experimental data during the exponential cell growth. From the results obtained fit the equation (2e), which has an exponential dependence. The values of  $K_I$  parameter are very low. This is because they obtained ethanol concentration is much lower than the concentration that causes complete cell growth inhibition for our experimental data. In the Fig. (3b) performance is shown for the free cell fermentation and it also has an exponential dependence.



(A)



(B)

**FIG. 3. COMPARISON OF MATHEMATICAL MODELS FOR SPECIFIC GROWTH RATE IN THE CASES OF IMMOBILIZED CELL (4 mm) (A) AND FREE CELLS (B), IN THE FOURTH FERMENTATION.**

In the case of the fourth fermentation, where we have the product inhibition, see an approximation of the values of the kinetic parameters. Since the alginate beads have relatively big pores (4, 7 mm), the diffusion through them is easy, i.e. the immobilizes grow in conditions similar to those of free fermentation. This can also explain the similar values of the maximum growth rate parameters  $\mu_{max}$  in both cases.

From the obtained results it is easy to choose a single best fitting model. Good approximation potential was shown by the models of Monod, Teisser, Aiba. The aim of this work was to make an selection of mathematical relationships, which begin the description of both the batch fermentation process with immobilized cells in the presence of diffusion resistances and continuous fermentation with immobilized cells. These relationships described the ethanol fermentation process very well and gave a clear idea of the process parameters influence on the kinetic characteristics. These models have the best approximating ability to describe the alcoholic fermentation with *Saccharomyces Carlsbergensis*.

#### IV. CONCLUSION

In the present investigation we considered modeling of batch fermentations with free and immobilized yeasts *Saccharomyces Carlsbergensis* in Na – alginate. Eleven of the most popular cultivation model structures were investigated. From the obtained results it is difficult to choose a single best fitting model. Good approximation potential was shown by the model of Monod, Teisser, Aiba. For substrate and product inhibition the most approximate models were exponential. Non-inhibitory fermentations fits with the Monod model, while product and substrate inhibition fermentation fits with exponential models.

As a conclusion immobilized cells in normal conditions ferment similarly to the free yeast. Based on the physical meaning of the obtained model parameters we compared the free and the immobilized cell fermentations. The results definitely proved the advantage of cell immobilization leading to higher production rates. Also immobilization based to kinetic parameters decrease the substrate and product inhibition phenomena compared to free yeast fermentation

#### REFERENCES

- [1] Arellano-Plaza M, Herrera-López EJ, Díaz-Montaña DM, Moran A, Ramírez-Córdova JJ (2007). *Unstructured Kinetic Model for Tequila Batch Fermentation*. Int. J. Math Comput. Simul, Vol. 1, Num. 1.
- [2] Bailey JE, Ollis DF (1986). *Biochemical Engineering Fundamentals*, Second Edition. USA: McGraw-Hill Book Company.
- [3] Aiba S, Shoda M, Nagatani M. *Kinetic of product inhibition in alcohol fermentation*. Biotechnol Bioeng 2000; 67:671-90.
- [4] Luljeta Xhagolli, Ilirjan Malollari. *Inxhinieria e proceseve biokimike*. 2009.

# Water Chemistry Management toward Corrosion for Secondary Cooling Piping of Multi Purpose Reactor GA Siwabessy Indonesia

Geni Rina Sunaryo<sup>1</sup>, Herry Sander<sup>2</sup>, Djarot S. Wisnubroto<sup>3</sup>

<sup>1,2</sup>BATAN, PTKRN, Bldg. 80, Puspiptek Area, Serpong, Tangerang, 15310, Indonesia

<sup>3</sup>BATAN, Headquarter Office, Kuningan Barat, Jakarta, Indonesia

**Abstract**— *The experimental of inhibitor, oxy and non oxy biocide effectiveness on suppressing the carbon steel by using the secondary water cooling system of RSG GAS was done. The observed parameter are corrosion rate, dissolved oxygen concentration, pH and conductivity. The variation concentration of inhibitor, oxy and non oxy biocide was applied. The corrosion rate and dissolved oxygen are measured by using Gamry electrochemical instrument, pH-meter and oxygenmeter, respectively. Whole experiment was carried out at room temperature. Speciment test is carbon steel with diameter of 16 mm and thickness of 8 mm, with the exposed are of 1cm<sup>2</sup>, polished by grid 220 up to 2000. The variation concentration was applied for all chemicals up to 60 ppm. From the experiment it is known that the rate corrosion is suppressed by the addition of inhibitor, higher concentration inhibitor will suppress much more. This phenomenon is strongly understandable by the experimental data that shows dissolved oxygen decrease due to the presence of inhibitor. The higher concentration of inhibitor cause the lower dissolved oxygen concentration. No pH change observed which means that the inhibitor does not give any contribution on releasing H<sup>+</sup> or OH<sup>-</sup> that causing pH changing. The addition of oxy biocide suppress corrosion rate from 0.7±0.02 mils/yr to 0.5± 0.02 mils/yr. However, non oxy biocide addition does not give any significant effect.*

**Keywords**— *rate corrosion, inhibitor, oxy biocide, non oxy biocide.*

## I. INTRODUCTION

Indonesia has three research reactor located in Bandung, Yogyakarta and Serpong. The biggest one with 30 MW is namely GA SIWABESSY. This is a multipurpose reactor, main domains for fundamental and applied science, industry, human health care and environmental studies, as well as nuclear energy applications and the development of nuclear science and technology related human resources. This research reactor has two cooling systems, primary and secondary. Primary cooling system is a close system and secondary is an open air system but semi close. In the purpose to maintaining the primary structure integrity as long as the designed life and suppressing the unexpected radioactive material produced by neutron irradiation coming from the core, the mineralized water is used for primary cooling water. Differ with this, the secondary system apply raw water which is coming from the PUSPIPTEK tap water. The pre treatment is applied for reducing the insoluble particles by depositing method in the water basin for few days. The following treatment is based on how to prevent either delay the metallic induced corrosion, scaling and microbe induced corrosion problem, therefore inhibitor and biocides chemicals are added up into the secondary water periodically with a certain concentration that is suggested by the company and as mentioned in Safety Analyses Report (SAR). In fact, how far the effectiveness of recommended concentration by company is not yet known. The prices of those chemicals are not cheap one. Therefore, it becomes a significant parameter that contributes a lot toward the annual maintenance budget. Less concentration will suppress the maintenance operating budget.

A continue operation of RSG GAS has to be carefully assessed, especially from the material structure point of view[1-3], in 30 years operation. The basic consideration for designing this facility for long life operation is based on material selection and strategy to managing the whole facility including the operating environment. Stainless Steel and aluminum are the main material used in the primary system, and carbon steel is the most material used for secondary system. One mechanism that hold as a key role for these materials in RSG GAS is corrosion problems. Lots of corrosion study towards those materials have to be understood well and are published elsewhere.[4-13] Specific publications about carbon steel corrosion also have been reported elsewhere.[14-17] However, different environment identic with different contaminant and may cause different accelerated corrosion. Therefore, understanding well about corrosion problem towards carbon steel under RSG GAS secondary environment has to be carried out in the purpose of gaining long life operation more than 30 years. the experiment related with the secondary water cooling of RSG GAS should be carried out.



One of the experiment for understanding those secondary water management effectiveness was done by implementing coupon corrosion surveillance and have been reported on the previous conference.[2,3] The visual result shows significant accelerated corrosion on the carbon steel coupons. The passive layer formation on the carbon steel to prevent further oxidation is known and highly exploited in industrial applications. Beside, inhibitor, the biocide chemicals also being added to control microorganism as a living substance that make inevitable environment. It induces biofilms formation as well and corrode the surfaces and give an extreme significant deterioration.[14] The effectiveness of those is considered to be the important parameter that should be understood well. The effect of the present biocides towards suppressing the microbial growth was done and reported elsewhere.[1]

Corrosion process is a redox reaction, which is both reactions (reduction and oxidation reactions) have a similar rate. Passivating the cathode by forming hardly dissolved metal hydroxide (MOH) will suppress the further corrosion process. Finally, the anode's rate reaction might be suppressed as well, then slowing the whole corrosion process. Therefore, the corrosion rate of carbon steel is the important parameter that should be determined under the inhibitor added and biocide as well. Dissolved oxygen is playing as a key parameter on the rate of oxidation process. Hence, the effect of inhibitor and biocide addition toward the concentration of oxygen has to be determined as well. .

The objective of the present experiment is to determine the corrosion rate of carbon steel under the inhibitor and biocide used at RGS GAS. These data will be added up as RSG GAS secondary cooling water data base, as a reference for the further safety analyses report evaluation.

Methodologies applied for determining corrosion rate is based on electrochemical, and the determining the concentration of dissolved oxygen is measured by using oxygenmeter detector. The concentration of inhibitor and biocide in this experiment is varied adjusted by the concentration range applied at RSG GAS.

## II. METHODOLOGY

### 2.1 Equipment

Experiments were conducted at room temperature and atmospheric pressure in a electrochemical glass (Fig. 1). A three-electrode setup and one hole for sample were used. A small magnetic stirrer with a speed control unit (0 rpm to 5,000 rpm) was used. A varied concentration of inhibitor, up to 150 ppm, in tap water as a solvent was used for the solutions.

The pH was monitored with an electrode immersed in the electrolyte. The expected pH is neutral. Oxygen concentration was monitored using an Oxygen meter. Electrochemical measurements were made using a Gamry Instruments.

### 2.2 Sample

Carbon steel materials from pipes are tested by using X-Met. Chemical compositions are given in Table 1. The material was machined from the parent material into a coin shape of 8 mm in thickness and 16 mm in diameter. Then, polished by using sandpaper of grid 220, 400, 800, 1000 up to 2000. The exposed area of the specimen was 1 cm<sup>2</sup>.

### 2.3 Procedure

The glass cells were filled with 500 ml of inhibitor solutions with a certain concentration. Monitoring of pH was done on line. The O<sub>2</sub> concentration was measured to judge when the solution was in equilibrium. The temperature was maintained constant at room temperature in all experiments. Before each experiment, the sample surface was polished using 500-grit silicon carbide (SiC) paper, washed with alcohol, rinsed with distilled water and then mounted on the specimen holders, and immersed into the inhibitor solutions.

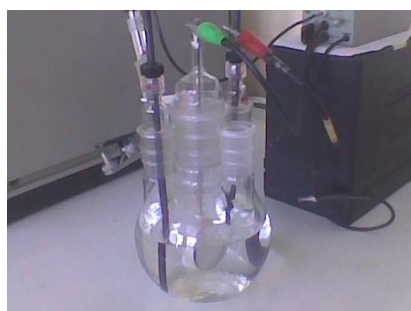


FIGURE 1. GLASS CELL FOR MEASURING CORROSION RATE

### III. RESULTS AND DISCUSSIONS

The carbon steel used as pipes at RGS GAS has chemical composition as shown in Table 1. The hardness of carbon steel is adjusted by the carbon content, but the corrosion behavior is mainly triggered by the environment.

**TABLE 1**  
**CHEMICAL COMPOSITION OF SAMPLE**

	%
C	0.2
Mn	0.4
Si	0.1
P	0.03
S	0.03

The effect of inhibitor at variant concentration at room temperature is shown in Fig.2. The experimental deviation is not more than 20% at zero inhibitor concentration. From the spread data taken, it shows clearly that the corrosion rate decrease abruptly and nearly approaches half of initial value at the concentration of inhibitor of 75 ppm. Then, it continues flat as a constant value.

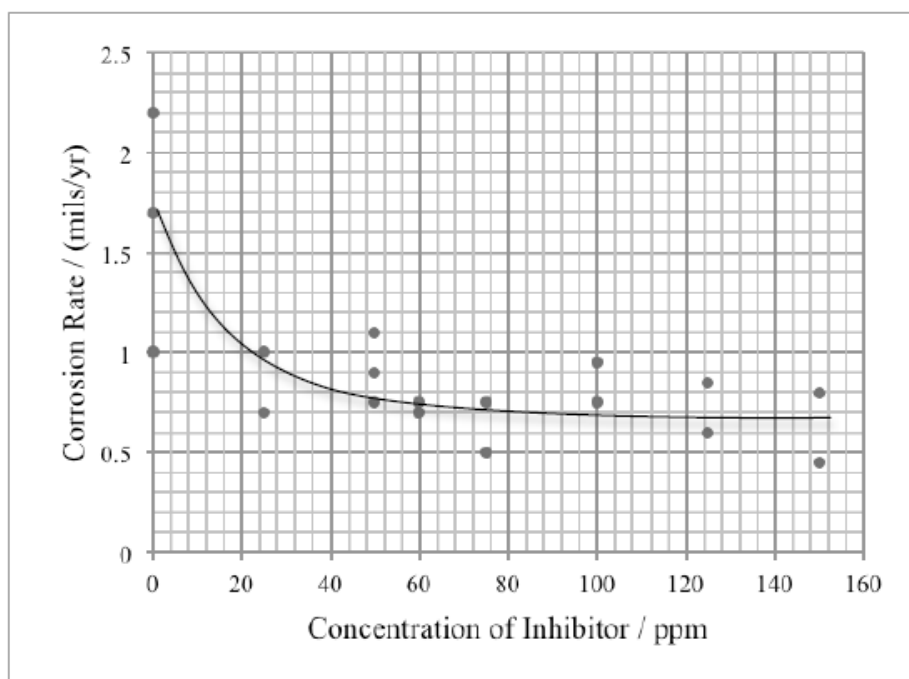
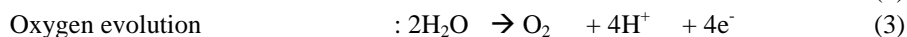
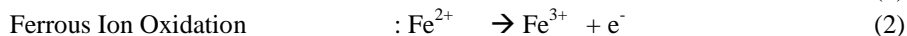


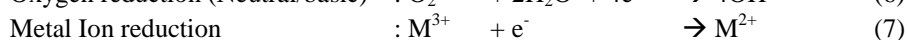
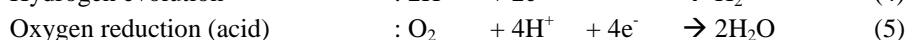
**FIGURE 2. THE CORROSION RATE DEPENDENCE ON CONCENTRATION OF INHIBITOR AT ROOM TEMPERATURE FOR CARBON STEEL MATERIAL.**

Corrosion mechanism process is based on electrochemical that involve electrons movement as results of redox. [7]

Anodic reaction:



Cathodic reaction:



Base on the above reactions, dissolved oxygen ( $O_2$ ) is a strong oxidator that induce the corrosion process at cathode and well understood. Therefore, how far the inhibitor effect to dissolved oxygen is has to be understood well. The experimental result for inhibitor effect towards dissolved oxygen concentration change is shown in Fig.3. The concentration of dissolved oxygen decrease with the increase of inhibitor. The dissolved oxygen concentration at the highest inhibitor concentration become one fifth of the none inhibitor. It shows clearly that the present of inhibitor suppress the dissolved oxygen concentration in the solutions, and may suppress a lot the both cathodic and anodic rate reactions. Finally, it may look that corrosion rate decrease (Fig.3.). Since the limited data gotten at one poin of concentration, the equilibrium effectiveness on inhibitor concentration on suppressing the dissolved oxygen is not appearing. It can be considered that the trend data should be consistent with that of corrosion rate (Fig.3).

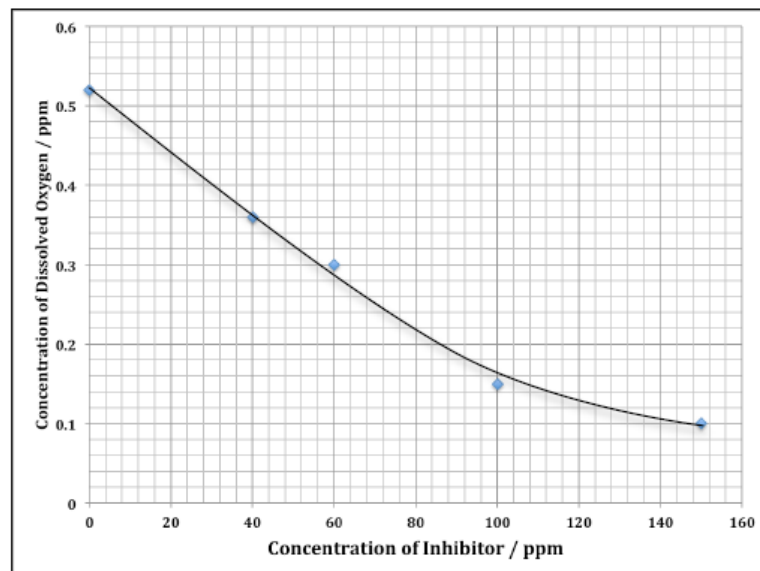


**FIGURE 3. THE EFFECT OF INHIBITOR ON SUPPRESSING THE DISSOLVED OXYGEN IN WATER AT ROOM TEMPERATURE.**

The inhibition efficiency is calculated by using the below equation [18];

$$\text{Inhibitor Efficiency (\%)} = 100 \times \{(CR_0 - CR_t) / CR_0\} \quad (9)$$

where :

$CR_0$  is the corrosion rate at zero inhibitor

$CR_t$  is the corrosion rate at certain concentration of inhibitor

Based on Fig 2, the relation between inhibitor concentration vs inhibition efficiency can be shown in Fig. 4.

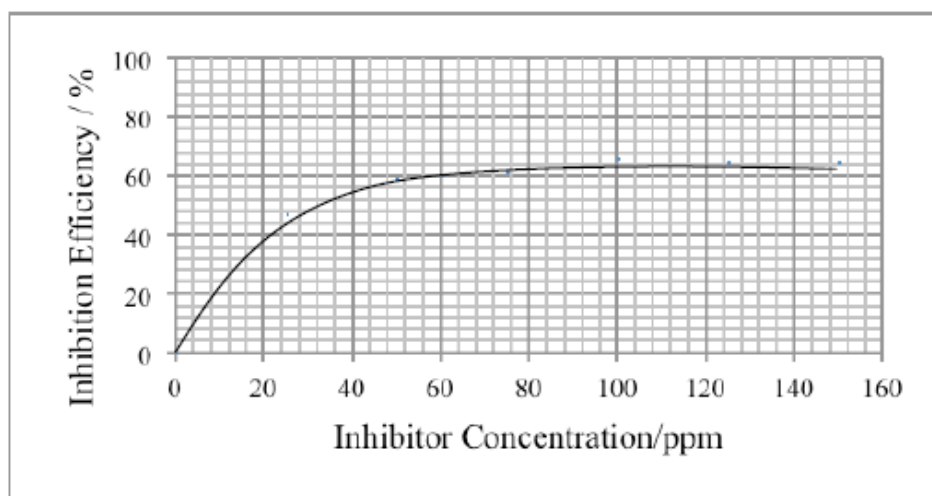


**FIGURE 4. INHIBITION EFFICIENCY VS INHIBITION CONCENTRATION AT ROOM TEMPERATURE.**

The inhibition efficiency increase abruptly at higher concentration of inhibitor up to 75ppm. Then it seems to be at constant value at approx 66%. It can be noted that there is optimal inhibition efficiency. The higher concentration used for inhibitor may not give any further higher inhibition efficiency.

In the real condition, both inhibitor and biocides are added at the same time, so the complex reaction should be occurred. Therefore, for the preliminary study, the effect of biocides on corrosion rate should be investigated separately and was implemented in this experiment. The active compound is orthoprosphate. There are two kind of biocide chemicals, ie. oxy and non oxy. Both are effective for a certain microbe that live needs oxygen and no oxygen, respectively. From the experimental result, it shows that non oxy biocide does not give any effect toward corrosion rate. However, oxy biocide may appear its contribution. It can be understood that, oxy biocide is dedicated to suppress the growing of microbe who need oxygen for their life. The experimental result of the effect of oxy biocide to corrosion rate is shown in Fig.5. The corrosion rate is suppressed abruptly by adding oxy biocide concentration up to 20 ppm. Then, no further decrease. Non oxy biocide does not give any effect toward corrosion rate of carbon steel.

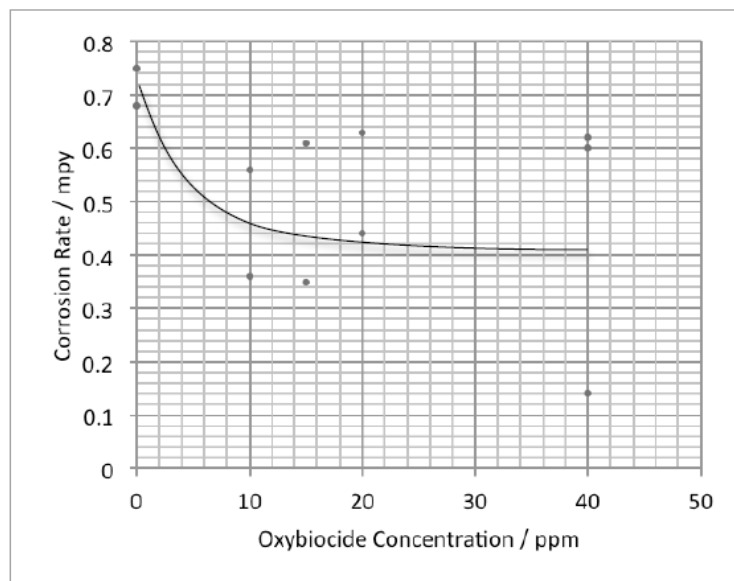


**FIGURE 5. THE CORROSION RATE DEPENDENCE ON CONCENTRATION OF OXY BIOCIDES AGENT FOR CARBON STEEL MATERIAL AT ROOM TEMPERATURE**

The experimental result of oxy and non oxy biocide effect to dissolved oxygen concentration is shown in Fig.6. Both oxy and non oxy biocide suppresses the dissolved oxygen concentration. Non oxy biocide gives a slight effect toward corrosion rate, therefore appear no effect toward corrosion rate. However, non oxy biocide suppresses the dissolved oxygen a lot. The concentration of dissolved oxygen decrease from originally become approx. one sixth at 30 ppm of oxy biocide.

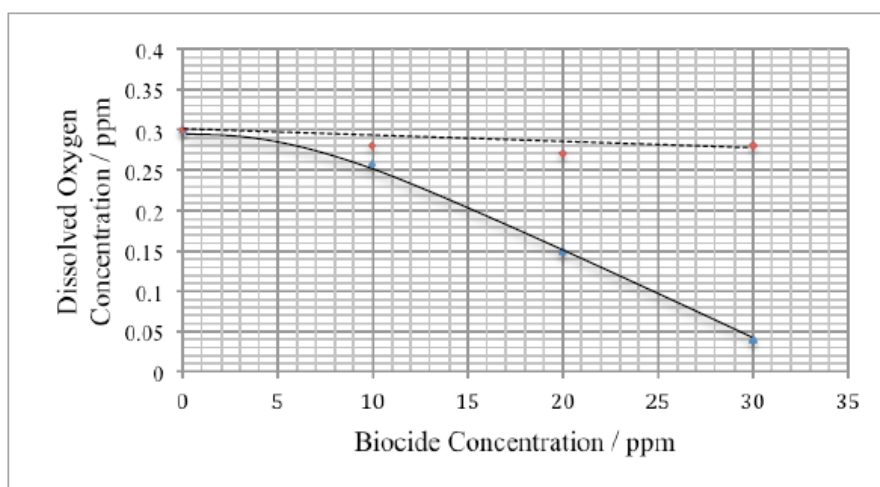


**FIGURE 6. THE DISSOLVED OXYGEN DEPENDENCE ON CONCENTRATION OF NON OXY BIOCIDES AGENT (---) AND OXY BIOCIDES AGENT (-) AT ROOM TEMPERATURE**

Base on the above experimental results above, the addition of oxy biocide should take into consideration toward the inhibition effect of the inhibitor added into the secondary cooling water of RSG GAS. The further work related with this basic mechanism should be clarified in the future work.

#### IV. CONCLUSION

The inhibitor added into the secondary cooling water of RGS GAS is effective to suppress the corrosion rate. The optimum inhibition efficiency is approx. 66%. The addition of biocide at the same time may give significant effect on inhibition efficiency and need to be clarified in the future work.

#### ACKNOWLEDGEMENTS

This experiment is supported by DIPA PTKRN BATAN. Highly appreciate to the colleagues from Center of PTKRN BATAN, PRSG BATAN and PSTBM BATAN for supporting this experiment as well.

#### REFERENCES

- [1]. Geni Rina Sunaryo, Febrianto, Dyah Erliana dan Budi Utomo, "Analisis kandungan mikroba di Pendingin Sekunder RSG-GAS 30MW", Prosiding Pertemuan Ilmiah Penelitian Dasar Ilmu Pengetahuan dan Teknologi Nuklir, Yogyakarta, 19 Juli 2011, p. 223-229.
- [2]. Geni Rina Sunaryo, Aplikasi Program Corrosion Surveillance untuk kolam penyimpan reaktor RSG-GAS, TKPFN-seminar, Surabaya 2010.
- [3]. Geni Rina Sunaryo, Sriyono, Diyah Erliana, "Water Chemistry Surveillance for Multi Purpose Reactor 30 MW GA Siwabessy, Indonesia". International Conference on Research Reactors: Safe Management and Effective Utilization Proceeding, Sydney, Australia, 5-9 November 2007.
- [4]. Engr Dr A.C Uzorh, "Corrosion Properties of Plain Carbon Steels", The International Journal Of Engineering And Science (IJES), Vol 2, Issue 11, Pages 18-24, 2013. ISSN (e): 2319 – 1813 ISSN (p): 2319 – 1805
- [5]. Osarolube, E., Owate, I. O. and Oforka, N. C "Corrosion behaviour of mild and high carbon steels in various acidic media", Scientific Research and Essay Vol.3 (6), pp. 224-228, June 2008 Available online at <http://www.academicjournals.org/SRE> ISSN 1992-2248 © 2008 Academic Journals
- [6]. C. Cuevas Arteaga, J. Porcayo Calderón, C. F. Campos Sedano, J. A. Rodríguez, "Comparison of Corrosion Resistance of Carbon Steel and Some Stainless Steels Exposed to LiBr-H<sub>2</sub>O Solution at low Temperatures", Int. J. Electrochem. Sci., 7 (2012) 445 – 470.
- [7]. EPRI Carbon Steel Handbook, Final Report, March 2007.
- [8]. IAEA, TRS 418, "Corrosion of Research Reactor Aluminum Clad Spent Fuel in Water", 2010
- [9]. Kim, Y.S., Hofman, G.L., Robinson, A.B., Snelgrove, J.L., Hanan, N., "Oxidation of aluminum alloy cladding for research and test reactor fuel", Nuclear Material. 378, page 220–228, 2012
- [10]. VS Raja, Bharat S. Padekar., "Role of chlorides on pitting and hydrogen embrittlement of Mg–Mn wrought alloy", Corrosion Science, Vol. 75, October 2013, pp 176-183
- [11]. Bhandari Jyoti, Faisal Khan, et.al., "Modelling of pitting corrosion in marine offshore steel structures-A technical review", Journal of Loss Prevention in the Process Industries 37, 2015, pp 39-62.
- [12]. Nugraha Luhur, Subiharto, Suhadi, Irwan, "Post Irradiation Material Control Implementation in RSG GA Siwabessy", Nuclear Reactor Management Bulletin, Vol. XI, No.1, April 2014 (in Indonesia)
- [13]. Keith A.Lichti et.al., "Galvanic corrosion study of carbon steel to arsenic and antimony couples", Geo-thermics 58, 2015, pp 15-21
- [14]. Biljana S. Maluckov, "Corrosion of Steels Induced by Microorganisms", Metall. Mater. Eng. Vol 18 (3) 2012 p. 223-231.
- [15]. Nardy Kip and Johannes A van Veen, "The dual role of microbes in corrosion", The ISME Journal (2015) 9, 542–551; doi:10.1038/ismej.2014.169; published online 26 September 2014
- [16]. Najoua Labjar, Mounim Lebrini, Fouad Bentiss, Nour-Eddine Chihib, Souad El Hajjaji, Charafeddine Jama, Corrosion inhibition of carbon steel and antibacterial properties of aminotris (methylenephosphonic) acid, Materials Chemistry and Physics, Volume 119, Issues 1–2, 15 January 2010, Pages 330-336.
- [17]. S. Malarvizhi and Shyamala R. Krishnamurthy, "Microbiologically Influenced Corrosion of Carbon Steel Exposed to Biodiesel", International Journal of Corrosion, Volume 2016 (2016), Article ID 4308487, 4 pages, <http://dx.doi.org/10.1155/2016/4308487>
- [18]. T. Sethi, A. Chaturvedi, R.K. Upadhyay and S.P. Mathur, "Corrosion Inhibitory Effects of some Schiff's Bases on Mild Steel in Acid Media", J. Chil. Chem. Soc. v.52 n.3 Concepción sep. 2007, <http://dx.doi.org/10.4067/S0717-97072007000300003>.

# Additive Manufacturing of PE/Fluorouracil Waffles for Implantable Drug Delivery in Bone Cancer Treatment

G. V. Salmoria<sup>1\*</sup>, F. E. Vieira<sup>2</sup>, G. B. Ghizoni<sup>3</sup>, I. M. Gindri<sup>4</sup>, L. A. Kanis<sup>5</sup>

<sup>1,2,3</sup>NIMMA, Department of Mechanical Engineering, Federal University of Santa Catarina, 88040-900, Florianópolis, SC, Brazil

<sup>1,4</sup>Biomechanics Engineering Laboratory, University Hospital (HU), Federal University of Santa Catarina, 88040-900, Florianópolis, SC, Brazil

<sup>5</sup>Grupo de Desenvolvimento em Tecnologia Farmacêutica, Universidade do Sul de Santa Catarina, 88504-900, Tubarão – SC – Brazil

**Abstract**— *In this study, implantable polyethylene/fluorouracil waffles were additively manufactured by selective laser sintering using different laser energy densities. SEM-EDS revealed a porous morphology for both PE and PE/FU waffles. High dispersion of fluorouracil particles were observed in samples prepared under different conditions. The PE/FU waffles manufactured at 5W had the highest flexural modulus, probably due to better PE particle coalescence, higher sinter degree and the dispersion of FU particles in the co-continuous porous PE matrix. The PE/FU waffles showed an initial burst as well as a rapid drug released, which are desirable characteristics for cancer treatment. This profile provides a high initial concentration of the drug in the cancer cells and a subsequent controlled release sustaining levels of the chemotherapeutic agent in the region of the bone tumor.*

**Keywords**— *Polyethylene/fluorouracil, Implantable drug delivery, Cancer treatment, Selective laser sintering.*

## I. INTRODUCTION

Additive Manufacturing, also known as 3D printing, enables the fast processing of three-dimensional devices from different materials and blends. This technology is also known for overcoming geometry limitations that are characteristic of conventional manufacturing techniques and it is able to produce more complex architectures. Selective laser sintering (SLS) is a type of Additive Manufacturing that creates objects, layer by layer, through the processing of powder materials using infrared laser beams. [1-3]. The microstructures of samples prepared via SLS depend on the process parameters (laser power, scan speed and spot diameter of the laser beam, and bed temperature) and the properties of the powder. For example, the particle shape and size distribution influence the powder packing density, while the melting flow behavior and the thermal stability determine the laser power and scan speed [4-10]. In recent years, SLS has demonstrated its potential in the biomedical field, for applications in bone tissue engineering, and for manufacturing drug delivery devices (DDD) [5-10].

Cancer is a public health concern worldwide and causes more than 600,000 deaths per year, only in the United States. The conventional approach to treat this disease includes tumor removal followed by chemotherapy or radiotherapy. However, resection surgery is not always an alternative, as observed in some cases of colon cancer metastases in which only 3.5-6.4% of the patients are eligible for tumor removal. Furthermore, current drugs used in the systemic treatments are not specific to cancer cells and end up causing toxicity to healthy cells and tissues [11-13]. Under this scenario, intratumoral drug delivery devices have emerged as a powerful strategy for localized treatment of solid tumors, promising to substantially improve the therapeutic outcomes for several kinds of cancer. This technology allows for controlled and sustained release of the drug into the solid tumors or in the resection cavities, which results in a safer and more effective strategy [14-16].

Bone cancer usually occurs in mature/old people, except osteosarcoma, which is typically diagnosed in young people (10–20 years old) and rarely in old people [17], in the extremity of the long bones, especially in the femur [18]. There are 45 main types of primary bone tumor, the most important being osteosarcoma (35.1% of the primary bone tumors), followed by chondrosarcoma, Ewing's sarcoma, and chondroma. By sex, males are more exposed to bone cancer (4% incidence in males compared to 3% in females)[18]. The implantation of drug delivery systems at the tumor site led to a reduction in dose of the antitumor agent, and consequently the risk of systemic toxicity decreased drastically compared with conventional systemic administration. Itokazu et al developed some drug-delivery systems and proved that porosity and pore size influenced the release rate of both antitumor agents [19]. The improved contact of antitumor agents with tumoral cells is expected to reduce the recurrence and metastasis of cancer [20].

5-Fluorouracil (5-Fluoro-1H, 3H-pyrimidine-2,4-dione, 5-FU) is a traditional drug used in the treatment of many cancers. Its mechanism of action is based on the inhibition of the enzyme denominated thymidylate synthase (TS), which works in the

synthesis of the nucleotides required for DNA and RNA replication. 5-FU is used as a systemic drug for chemotherapy as well as in the formulation of drug delivery systems where good outcomes have been observed [21-24]. On the other hand, polyethylene (PE) is a bio-inert olefin approved by FDA for use in the human body as a medical device. Drug delivery systems using PE have been proposed due to its biocompatibility and resistance to the biological environment [25, 26]. The drug can be physically mixed with this polymer and then delivered to the surrounding environment via diffusion.

In this study, polyethylene/fluorouracil (PE/FU) waffles were prepared by SLS using different laser energy densities. The morphological characteristics, mechanical properties and drug release of the waffles were evaluated and correlated with the processing conditions. The particle size and shape, along with the laser power, were used to tune the porosity of polyethylene matrix manufactured by SLS and, consequently, to control the properties for potential biomedical applications.

## II. EXPERIMENTAL

### 2.1 Materials

The polymeric powder used in this study was commercial polyethylene (HD 7555, Ipiranga S.A.) with an average molecular weight of 140,000 to 250,000 g/mol, melting temperature ( $T_m$ ) of 133 °C, melt flow index of 2.65 g/10 min, and density of 0.89 g/cm<sup>3</sup> at 25 °C. The particle size range used in this study was from 125 to 212 µm. The fluorouracil (FU) was obtained from Hubei Gedian Pharmaceutical Co with a melting temperature of 282 °C. The powder blend was prepared by mechanical mixing in a Y-type rotator for 10 minutes at 30 rpm.

### 2.2 Waffles Manufactured by Selective Laser Sintering

The pure PE and PE/FU waffles (35×5×1.4 mm) were sintered in a selective laser sintering system with a 9 W power CO<sub>2</sub> laser and laser beam diameter of 250 µm. This study was performed in the open air and the powder bed temperature was 45 °C. The laser scanning speed was maintained at 350 mm/s. The building layer thickness used was 250 µm and the spacing between the laser scans was 125 µm. The laser density energies to manufacture the waffles are shown in Table 1.

**TABLE 1**  
**PURE PE AND PE/FU WAFFLES MANUFACTURED WITH DIFFERENT LASER ENERGY.**

Waffle	Fluorouracil content (%)	Laser power (W)
PE	0	3.0
PE	0	5.0
PE/FU	10	3.0
PE/FU	10	5.0

### 2.3 Infrared and Near-Infrared Spectroscopy

Infrared spectra of pure and processed materials were obtained using a Perkin-Elmer Frontier MIR/NIR spectrophotometer in the attenuated total reflectance (ATR) mode. For each sample 20 scans at a resolution of 4 cm<sup>-1</sup> were obtained. Near infrared was also performed using a NIR Analyzer in the reflectance mode from 1000–2500 nm. 20 scans were obtained for each sample.

### 2.4 Scanning Electron Microscopy (SEM)

The morphology of the waffles were examined by an XL 30 Phillips scanning electron microscopy (SEM). The specimens were coated with gold in a Bal-Tec Sputter Coater SCD005.

### 2.5 Differential Scanning Calorimetry (DSC)

Differential scanning calorimetry (DSC) curves were obtained using a differential scanning calorimeter (Perkin Elmer) from 0 to 300 °C at a heating rate of 10 °C/min. The average sample size was 5 mg and the nitrogen flow-rate was 25 cm<sup>3</sup>/min.

### 2.6 Mechanical tests

A DMA Q800 system of TA instruments with a single cantilever clamp was used for the mechanical tests of the SLS waffles (35×5×1.4 mm). A ramp of 2 N/min from 0 to 18N was applied for the quasi-static flexural tests. The fatigue test was performed applying an oscillatory deformation. The amplitude used was 750 µm in both directions, under a frequency of 1 Hz, at 35 °C.

## 2.7 Drug release and Recovery of incorporated Fluorouracil

The dry specimens with known drug content and thickness were immersed in a 50-mL phosphate buffer solution (PBS, pH = 7.4) (to maintain sink conditions), and shaken horizontally in a Dubnoff bath (Quimis S.A, Brazil) at a rate of 60 rev/min to minimize the boundary effect, and  $37.0 \pm 0.5$  °C. The total receptor solution volume was removed periodically and replaced with fresh solutions. After suitable dilution with the buffer solution, the total drug release was obtained using a previously prepared calibration curve (five dilutions between 0.0020 and 0.0220 mg/mL) using a UV-Vis spectrophotometry at  $\lambda_{\max}$  of 265 nm, on a Hitachi 2010 double-beam UV-visible spectrophotometer.

For the recovery test, waffle segments obtained from three different portions of the total material produced under each condition were collected. Each piece was weighed and cut into smaller pieces to increase the surface area in contact with the solvent (10 mL of methanol; in triplicate). Samples were kept in an ultrasonic bath for 2 h and then analyzed by UV-vis spectrophotometry at  $\lambda_{\max}$  of 265 nm

## III. RESULTS AND DISCUSSION

PE and PE/FU waffles were prepared using additive manufacturing under two laser power conditions, 3 W and 5 W. The morphological characteristics of each sample, as well as the chemical composition, were investigated using SEM-EDS. Furthermore, the crystallinity, mechanical properties and drug delivery profiles of the samples were also evaluated to understand the effect of the processing parameters on the characteristics of the materials.

The images of PE and PE/FU waffles processed under different conditions are shown in Figure 1 (A-D). The waffles showed coalescence of particles, uniform morphology, and interconnected pores distributed within the PE matrix, all of which are important characteristics in materials to be used in implantable drug delivery devices. The PE waffles produced with the lower laser energy showed a lower degree of sintering with the formation of small necks between the particles (Figure 1, A). On the other hand, the PE/FU waffles, particularly those formed at 5 W, showed co-continuous phases and an extensive neck formation between the particles (Figure 1, D). PE/FU waffles also demonstrated greater particle coalescence probably due to the better laser absorption by the fluorouracil particles.

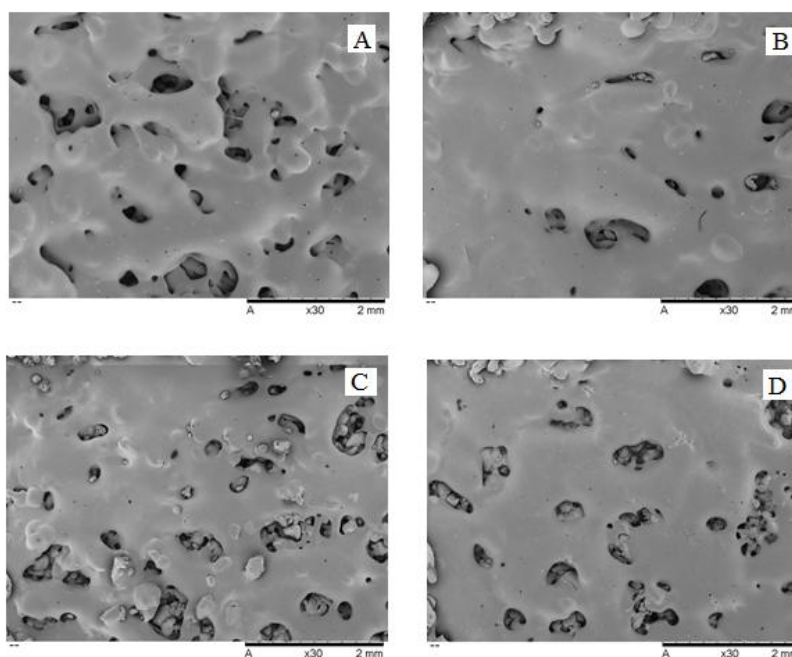


**FIGURE 1. SURFACE MICROGRAPHS OF PURE PE AND PE/FU WAFFLES SINTERED USING DIFFERENT POWER CONDITIONS: PE 3W (A), PE 5W (B), PE/FU 3W (C), and PE/FU 5W (D).**

The micrographs of PE/FU waffles, the EDS of nitrogen atom contrast, and nitrogen chart are shown in Figure 2. Small particles of fluorouracil were observed throughout the polyethylene matrix, demonstrating the good drug distribution for both processing conditions (Figure 2 A-D). The EDS analysis also revealed the ratio of carbon, oxygen, nitrogen and fluorine atoms present in the PE matrix as well as in the FU particles (Figure 2 E).



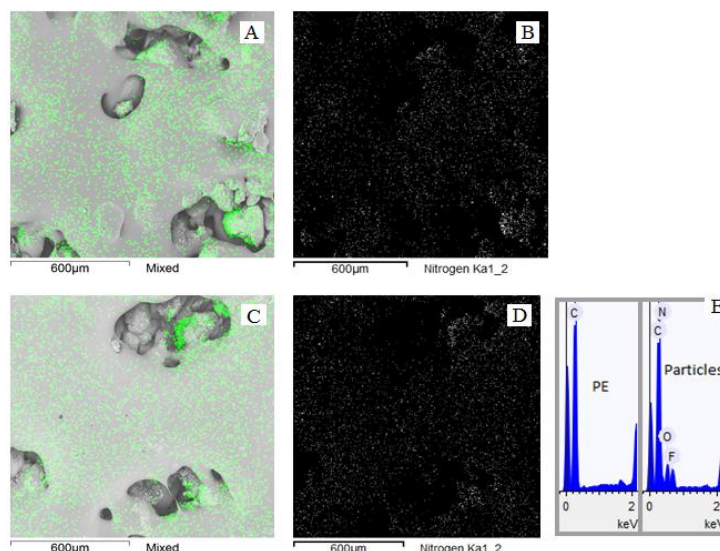


**FIGURE 2. SURFACE MICROGRAPHS PRESENTING THE EDS NITROGEN CONTRAST AND CHART OF PE/FU WAFFLES SINTERED UNDER DIFFERENT POWER CONDITIONS: PE/FU 3W (A AND B) , PE/FU 5W (C AND D), AND THE EDS COMPOSITION OF PE MATRIX AND FU PARTICLES IN THE WAFFLE (E).**

To confirm the chemical structure and evaluate the potential intermolecular interactions between the polymer and drug, pure FU, PE waffles and PE/FU waffles were investigated using FTIR (Figure 3). The FU spectrum demonstrated absorption peaks characteristic of this compound and in agreement with the literature [25]. The  $\text{=C-H}$  stretching of fluorouracil resulted in an absorption band in the  $3100\text{--}3000\text{ cm}^{-1}$  region. The peaks at  $2938\text{ cm}^{-1}$  and  $2831\text{ cm}^{-1}$  were ascribed to the  $\text{-CH}_2$  group. The stretching bands of  $\text{C=N}$  and  $\text{C=C}$  bonds in the ring were verified in the  $1580\text{--}1650\text{ cm}^{-1}$  region, while the vibration of  $\text{C=O}$  bond correspond to the absorption peak at  $1724\text{ cm}^{-1}$  [25]. Additional bands at  $1450\text{ cm}^{-1}$  and  $1350\text{ cm}^{-1}$  are characteristic of substituted pyrimidine compounds as well as the peaks at  $1180\text{ cm}^{-1}$  and  $1251\text{ cm}^{-1}$ , which were associated with  $\text{C-O}$  and  $\text{C-N}$  bond frequencies, respectively [25]. The fluorine bond ( $\text{C-F}$ ) also resulted in absorption at  $1230\text{ cm}^{-1}$  and in the  $820\text{--}550\text{ cm}^{-1}$  region [20]. The spectra of the PE waffles (Figure 3, B and C) also corroborated with previous results from the literature. Symmetric and asymmetric stretching of  $\text{C-H}$  in  $\text{CH}_2$  groups resulted in peaks at  $2950$  and  $2850\text{ cm}^{-1}$ . Moreover, the peak  $1350$  and  $1450\text{ cm}^{-1}$  is related to the bending movement of  $\text{CH}_2$ , whereas the rocking vibration of  $\text{CH}_2$  resulted in a peak at  $720\text{ cm}^{-1}$  [25, 26].

The main peaks in the FTIR spectra for the PE/FU waffles (Figure 3, D and F) correspond to the PE matrix, due to the increased proportion of the polymeric material (90 wt%) in comparison to the drug (10 wt%). The presence of the drug is confirmed by a shoulder band in the  $1580\text{--}1650\text{ cm}^{-1}$  region and the peaks around  $600\text{ cm}^{-1}$ , which were associated with  $\text{C=C}$  and  $\text{C=N}$  ring bonds and  $\text{C-F}$  bond in the fluorouracil structure. The peaks ascribed to PE were monitored in PE and PE/FU to investigate intermolecular interactions. No differences were observed in PE/FU in comparison to the PE waffles, suggesting the absence of intermolecular interactions between polymer and drug.

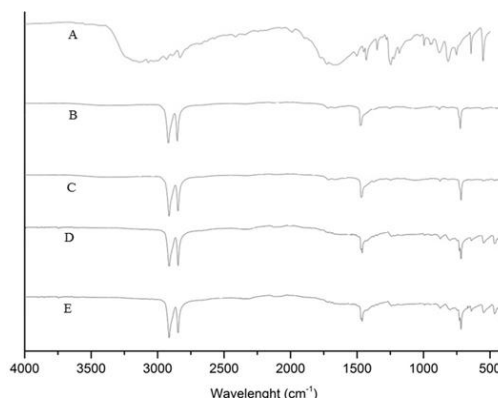


**FIGURE 3. FTIR-ATR SPECTRA FOR FLUOROURACIL (A), PURE PE AND PE/FU WAFFLES SINTERED USING DIFFERENT POWER CONDITIONS: PE 3W (B), PE 5W (C), PE/FU 3W (D), AND PE/FU 5W (E).**

The full near-infrared (NIR) spectrum ranges from 700 nm to 2500 nm ( $14285$  to  $4000\text{ cm}^{-1}$ ). The results obtained for the pure FU, PE and PE/FU waffles are summarized in Figure 4 (A-E). Absorption features between 800 to 1200 nm correspond to combinations associated with CH, OH, and NH bonds and higher-order overtones. The overtone of the CH and OH groups originated information in the first overtone range (1500 to 1900 nm). A combination of stretching and bending vibrations associated with CH, NH, and OH molecular groups provided information within the combination range from 2000 to 2500 nm [28, 29]. The FU spectrum revealed a broad absorption band centered at 2200 nm, which is related to the ring structure and the urea group. This region of the NIR spectrum is dominated by second-overtone carbonyl stretching bands and N-H combination bands. This band corresponds to the combination of the symmetric and asymmetric N-H stretching coupled with the N-H bending vibration. Systems containing aryl rings also show absorption in the 2130- to 2160 nm region [27]. The first overtones of the asymmetric and symmetric N-H stretches for fluorouracil were overlapped under the 1700 nm [30].

The NIR spectra of the PE waffles (Figure 4, B and C) showed a small peak at 1200 nm related to the second-overtone of C-H bonds in the methylene groups, and an intense peak at 1670-1780 nm associated with the first overtone of C-H. The combination bands from the C-H bonds in the methylene groups are present from 2250 to 2300 nm [27]. The NIR spectra of the PE/FU waffles presented (Figure 4, D and E) the same bands as the pure PE, the major component, with an additional peak at 2330 nm relative to the fluorouracil presence which was 10 %.

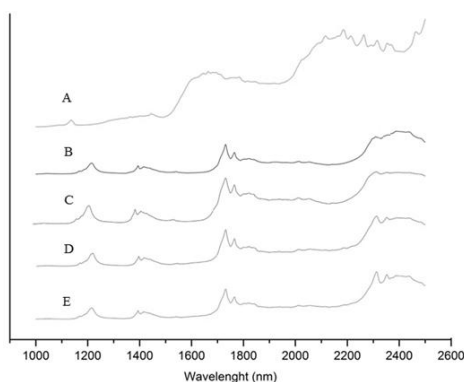


**FIGURE 4. NIR SPECTRA FOR FLUOROURACIL (A), PURE PE AND PE/FU WAFFLES SINTERED USING DIFFERENT POWER CONDITIONS: PE 3W (B), PE 5W (C), PE/FU 3W (D), AND PE/FU 5W (E).**

The thermal behavior of the starting materials and waffles as well as their interaction after processing was investigated using DSC. The DSC curves for the pure fluorouracil, PE and PE/FU waffles are shown in Figure 5. The FU and PE melting points were observed at 284 °C and 134 °C, respectively. Thermal parameters obtained from the DSC curves, such as melting temperature, melting enthalpy and crystallinity are summarized in Table 2. There was no significant variation in the melting temperature among the waffles, regardless of the processing condition. Higher laser power seems to cause an increase in the crystallinity of the PE waffles, probably due to the slower cooling rate of the waffles, but the crystallinity values for the PE/FU waffles were the same for both temperatures. This phenomenon suggests the inexistence of a chemical interaction between fluorouracil and the PE matrix.

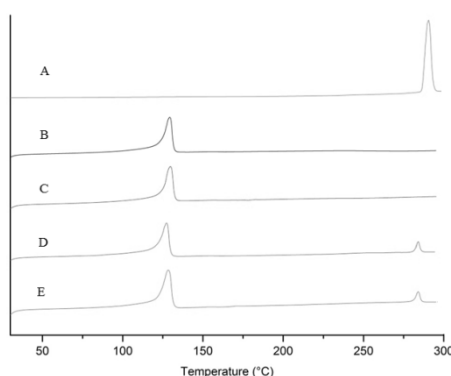


**FIGURE 5. DSC THERMOGRAMS FOR PURE FLUOROURACIL (A), PE 3W (B), PE 5 (C), PE/FU 3W (D) AND PE/FU 5W (E) WAFFLES.**

**TABLE 2**  
**MELTING ENTHALPY, MELTING TEMPERATURE AND DSC CRYSTALLINITY OF THE PURE FLUOROURACIL, PE AND PE/FU WAFFLES PREPARED USING DIFFERENT LASER ENERGY.**

Specimen	$\Delta H_{PE}$ (J/g)	$T_m$ ( $^{\circ}C$ )	PE Crystallinity (%)	$\Delta H_{FU}$ (J/g)	$T_m$ ( $^{\circ}C$ )	FU content (%)
Pure FU	-	-	-	$214 \pm 0.6$	$285 \pm 0.3$	100
PE 3W	$158 \pm 2.2$	$129 \pm 0.6$	$53 \pm 2.0$	-	-	-
PE 5W	$135 \pm 2.4$	$128 \pm 0.4$	$46 \pm 3.0$	-	-	-
PE/FU 3W	$158 \pm 2.4$	$129 \pm 0.4$	$53 \pm 2.0$	$22 \pm 0.3$	$287 \pm 0.4$	$10 \pm 1$
PE/FU 5W	$112 \pm 2.1$	$128 \pm 0.7$	$39 \pm 3.0$	$24 \pm 0.3$	$285 \pm 0.3$	$11 \pm 1$

*\*Crystallinity values are based on the enthalpy of melting of 100% crystalline PE, 288 J/g [31]. For the PE/FU waffles, only 90 % of the weight was considered in the PE crystallinity calculus, because 10 % was FU.*

Besides evaluating the morphological and thermal properties of PE and PE/FU waffles, the mechanical behavior was also investigated. Flexion test curves for PE and PE/FU waffles are shown in Figure 6 and mechanical parameters are summarized in Table 3. The PE and PE/FU waffles manufactured at 3W (A) showed a lower value for flexural modulus than those manufactured using a higher laser power. Moreover, the PE/FU waffles had lower flexural modulus values than the pure PE waffles processed under the same conditions. This behavior is explained based on the presence of FU particles dispersed throughout the polymeric matrix, which decreases its mechanical properties. The higher flexural modulus of the PE/FU waffles manufactured at 5 W (D) demonstrated that the stiffness of the PE waffles increased for samples processed with higher laser energy. This processing condition apparently yielded an increased polymer flow, greater neck formation of the particles and lower porosity.

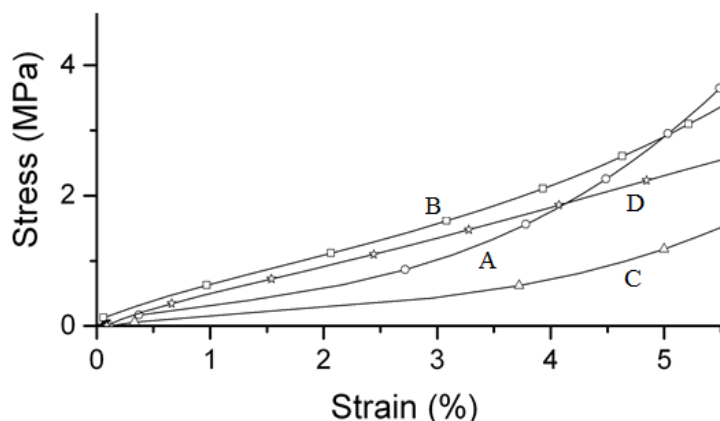


**FIGURE 6. FLEXURAL TEST CURVES OF THE PURE PE AND PE/FU WAFFLES SINTERED USING DIFFERENT POWER CONDITIONS: PE 3W (A), PE 5W (B), PE/FU 3W (C), AND PE/FU 5W (D).**

**TABLE 3**  
**FLEXURAL MODULUS AND STRENGTH OF THE PURE PE AND PE/FU WAFFLES PREPARED WITH DIFFERENT LASER SINTERING POWER.**

Specimen	Flexural Modulus (MPa)	Strength at 5% strain (MPa)
PE 3W	$44 \pm 3$	$2.7 \pm 0.7$
PE 5W	$68 \pm 6$	$2.8 \pm 0.8$
PE/FU 3W	$15 \pm 2$	$2.1 \pm 0.6$
PE/FU 5W	$46 \pm 6$	$1.3 \pm 0.6$

The fatigue curves of PE and PE/FU waffles showing stress resistance as a function of the cycle number are shown in Figure 7. The laser energy was also observed to affect the fatigue resistance of the processed samples. The PE and PE/FU waffles prepared at 5 W (Figure A and C, respectively) showed higher fatigue strength (i.e. smaller stress variations) than the PE and PE/FU waffles manufactured at 3 W. The fatigue curve for PE and PE/FU waffles showed lower stress variations and higher fatigue resistance up to 1000 cycles. This increased flexibility may be associated with the lower sinter degree and stiffness of samples processed under these conditions.

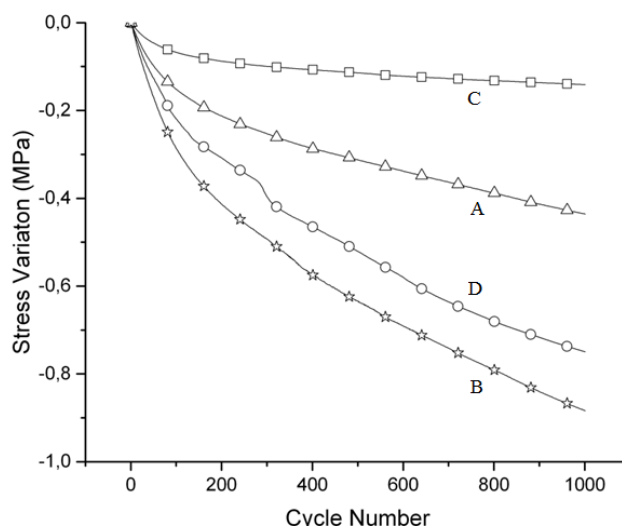


**FIGURE 7. FATIGUE TEST CURVES OF THE PURE PE AND PE/FU WAFFLES SINTERED USING DIFFERENT POWER CONDITIONS: PE 3W (A), PE 5W (B), PE/FU 3W (C), AND PE/FU 5W (D).**

Finally, the effect of processing conditions on the drug release profile was evaluated using UV-Vis. The drug release profiles of the PE/FU waffles are shown in Figure 8. Overall, a rapid drug release was observed for the waffles manufactured using both 3 W and 5 W and the total release was accomplished after 2 days. The initial burst, with cumulative values of around 50 mg/g of the drug was detected in the first 4 hours. This behavior may be attributed to the hydrophilicity of FU (12.5 mg/ml) as well as the high porosity of the PE/FU waffles, which facilitates the drug dissolution in the aqueous medium. Then the release rate became slow and constant until the end of the experiment for both formulations (Figure 8A and B). The PE/FU waffles manufactured at 3W presented greater drug release, which may be associated to the higher porosity of this material.

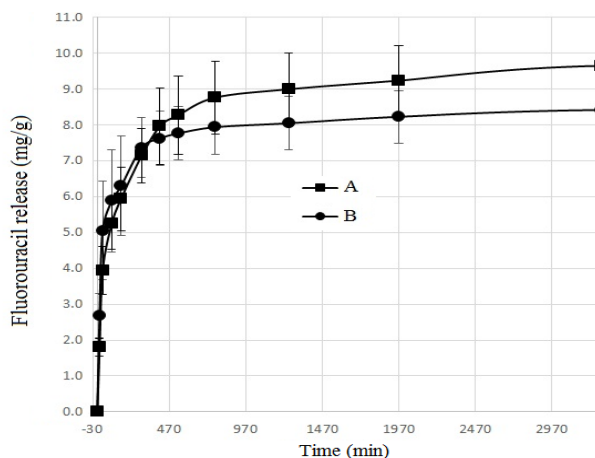


**FIGURE 9. FLUOROURACIL RELEASE AS A FUNCTION OF TIME FOR PE/FU WAFFLES MANUFACTURED USING 3W (A) AND 5W (B) OF LASER POWER.**

The drug release pattern observed in this work is characteristic of drug delivery systems loaded with FU [32-34]. The initial concentration of FU released from the PE/FU waffles may provide a high initial concentration of the drug locally in the cancer cells following implantation. The subsequent controlled release allows for sustained levels of the chemotherapeutic agent at the cancer site [35, 36]. These results demonstrate the potential use of PE/FU tables for treating cancer cells since FU molecules and aggregates have affinity for cancer cells and may accumulate preferentially within tumors through the delivery of the implanted waffle.

#### IV. CONCLUSION

This study demonstrated additive manufacturing of PE/FU waffles through SLS with great efficiency. SEM-EDS revealed the presence of small fluorouracil particles dispersed over the surface and throughout the porous PE matrix for the PE/FU waffles processed under 3W and 5W. The main peaks in the FTIR and NIR spectra for the PE/FU waffles were the same as those observed in the spectra for the pure PE waffles. However, the presence of the drug was confirmed by peaks at 600 cm-

1 and at 2330 nm, which were associated with C-F bond of the fluorouracil compound. The PE/FU waffles prepared using the higher laser power (5 W) had a higher flexural modulus, probably due to better coalescence of the PE particles, a higher sinter degree and a good dispersion of FU particles throughout the co-continuous porous PE matrix. The PE/FU waffles initially showed a rapid drug released due to the hydrophilic character of fluorouracil. This is a desirable characteristic to provide a high initial concentration of the drug locally in the cancer cells following implantation. The slow and controlled release of the drug presented subsequently by the PE/FU waffles is important to sustain appropriate levels of the chemotherapeutic agent in the region of the tumor; thus demonstrating a significant potential to improve bone cancer treatments.

#### ACKNOWLEDGEMENTS

The authors would like to thank PRONEX/FAPESC, CNPQ, CAPES and FINEP for their financial support.

#### REFERENCES

- [1] Low, K.H.; Leong, K.F.; Chua, C.K.; Du, Z.H.; Cheach, C.M., (2001) Characterization of SLS parts for drug delivery devices. *Rapid Prototyping Journal*, Vol. 7 (5), 262-267.
- [2] Leong, K.F.; Phua, K.K.S.; Chua, C.K.; Du, Z.H.; Teo, K.O.M. (2001) Fabrication of Porous Polymeric Matrix Drug Delivery Devices Using the Selective Laser Sintering Technique, *Proc Instn Mech. Engrs: Part H (Journal of Engineering in Medicine)*, Vol 215, 191 - 201.
- [3] Cheah, C.M., Leong, K.F., Chua, C.K., Low, K.H., Quek, H.S., (2002) Characterization of micro-features in selective laser sintered drug delivery devices. *Proc. Inst. Mech. Eng. H*, 216, 369-383.
- [4] Yeong, W. Y.; Chua, C.K., Leong, K. F., Chandrasekaran, M., (2004) Rapid Prototyping in Tissue Engineering: Challenges and Potential. *Trends in Biotechnology*, Vol. 22, 643-652.
- [5] Leong, K.F., Chua, C.K., Gui, W.S. and Verani W.S.G., (2006) Building Porous Biopolymeric Microstructures for Controlled Drug Delivery Devices Using Selective Laser Sintering. *The International Journal of Advanced Manufacturing Technology*, Vol. 31 (5), 483-489.
- [6] Leong, K.F.; Wiria, F.E.; Chua, C.K.; Li, S.H., (2007) Characterization of a poly-epsilon-caprolactone polymeric drug delivery device built by selective laser sintering. *Biomed. Mater. Eng.*, Vol. 17 (3), 147-157.
- [7] Salmoria G.V., Klauss P., Zepon K., Kanis L.A., Roesler C.R.M., Vieira L.F. (2012) Development of functionally-graded reservoir of PE/PG by selective laser sintering for drug delivery devices. *Virtual and Physical Prototyping*, 7 (2), 107-115.
- [8] Salmoria G.V., Klauss P., Zepon K.M., Kanis L.A. (2013). The effects of laser energy density and particle size in the selective laser sintering of polyethylene/progesterone specimens: morphology and drug release. *International Journal of Advanced Manufacturing Technology*, 66 (5), 1113-1118. doi:10.1007/s00170-012-4393-8
- [9] Salmoria, G. V., Hotza, D., Klauss, P., Kanis, L. A., Roesler, C.R.M. (2014) Manufacturing of Porous Polyethylene Prepared with Different Particle Sizes and Infrared Laser Sintering Conditions: Microstructure and Mechanical Properties, *Advances in Mechanical Engineering*, 2014, art. no. 640496. (doi: 10.1155/2014/640496)
- [10] Salmoria, G.V., Cardenuto, M.R., Roesler, C.R.M., Zepon, K.M., Kanis, L.A. (2016) PE/Ibuprofen Implants Fabricated by Selective Laser Sintering for Orbital Repair. *Procedia CIRP* 49, 188 - 192. <https://doi.org/10.1016/j.procir.2015.11.013>
- [11] Alessandro Olivi · Matthew G. Ewend Tadanobu Utsuki · Betty Tyler · Abraham J. Domb Daniel J. Brat · Henry Brem (1996). Interstitial delivery of carboplatin via biodegradable Polymers is effective against experimental glioma in the rat. *Cancer Chemother Pharmacol.* 39, 90-96.
- [12] Feng Qian, Gerald M. Sidel, Damon M. Sutton, Agata Exner, Jinming Gao (2002). Combined modeling and experimental approach for the development of dual-release polymer millirods. *Journal of Controlled Release.* 83, 427-435
- [13] Oktay Tacara, Pornsak Sriamornsak, Crispin R. Dassa (2013). Doxorubicin: an update on anticancer molecular action, toxicity and novel drug delivery systems. *Journal of Pharmacy and Pharmacology*, 65, pp. 155-150.
- [14] Weinberg, B. D., Ai, H., Blanco, E., Anderson, J. M. and Gao, J. (2007). Antitumor efficacy and local distribution of doxorubicin via intratumoral delivery from polymer millirods. *J. Biomed. Mater. Res.*, 81A: 161-170. doi:10.1002/jbm.a.30914
- [15] Brent D. Weinberg, Elvin Blanco, Jinming Gao (2008) Polymer Implants for Intratumoral Drug Delivery and Cancer Therapy. *Journal of Pharmaceutical Sciences*, Volume 97, Issue 5, Pages 1681-1702.
- [16] Solorio L1, Patel RB, Wu H, Krupka T, Exner AA. (2010) Advances in image-guided intratumoral drug delivery techniques. *Ther Deliv.* Aug;1(2):307-22.
- [17] Canadian Cancer Society. *Canadian Cancer Statistics 2004*. Toronto: National Cancer Institute of Canada; 2004.
- [18] Bleyer A, O'Leary M, Barr R, Ries L, editors. *Cancer Epidemiology in Older Adolescents and Young Adults 15 to 29 Years of Age, Including SEER Incidence and Survival: 1975-2000*. Bethesda (MD): National Cancer Institute; 2006.
- [19] Itokazu M, Esaki M, Yamamoto K, Tanemori T, Kasai T. (1991). Local drug delivery system using ceramics: vacuum method for impregnating a chemotherapeutic agent into a porous hydroxyapatite block. *J Mater Sci-Mater M.* 10(4):249-252.
- [20] Itokazu M, Kumazawa S, Wada E, Wenyi Y. (1996). Sustained release of adriamycin from implanted hydroxyapatite blocks for the treatment of experimental osteogenic sarcoma in mice. *Cancer Lett.* 107(1):11-18.

- [21] Hiroshi Seno, Kazuki Ito, Koichi Kojima, Nobuaki Nakajima, Tsutomu Chiba (1999). Efficacy of an implanted drug delivery system for advanced hepatocellular carcinoma using 5-fluorouracil, epirubicin and mitomycin C. *Journal of Gastroenterology and Hepatology*. 14, 811-816.
- [22] Shenguo Wang, Hongli Chen, Qing Cai, Jianzhong Bei (2001). Degradation and 5-Fluorouracil Release Behavior in vitro of Polyethylene/ poly(ethylene oxide)/polylactide Tri-component Copolymer. *Polym. Adv. Technol.* 12, 253-258.
- [23] Martini LG, Collett JH, Attwood D.(2000)The release of 5-fluorouracil from microspheres of poly(epsilon-caprolactone-co-ethylene oxide). *Drug Dev Ind Pharm.* 26(1):7-12.
- [24] Parul Singh, Gunjan Tyagi, Ranjana Mehrotra, A.K.Bakhshi (2009). Thermal stability studies of 5-fluorouracil using diffuse reflectance infrared spectroscopy. *Drug Test. Analysis* 2009,1, 240-244.
- [25] Gulmine J.V, Janissek P.R, Heise H.M, Akcelrud L (2002). Polyethylene characterization by FTIR. *Polymer Testing*, 21,5, 557-563.
- [26] Paquet O., Krouit M., Bras J., Thilemans W., Belgacem M. (2010). Surface modification of cellulose by PE grafts. *Acta Materialia*, 58, 792-801.
- [27] Edward SK, Mahpour M. The identification and origin of N-H overtone and combination bands in the near-infrared spectra of simple primary and secondary amides. *Spectrochim Acta A* 1973;29:1233-1246.
- [28] Hazen KH, Arnold MA, Small GW. Measurement of glucose in water with first-overtone near-infrared spectra. *Appl Spectrosc* 1998;52:1597-1605.CrossRef
- [29] Christopher V. Eddy, Mark A. Arnold (2001). Near-Infrared Spectroscopy for Measuring Urea in Hemodialysis Fluids. *Clinical Chemistry*, Vol. 47, Issue 7, pp 1279-1286.
- [30] Crandall, E. W. and Jagtap, A. N. (1977), The near-infrared spectra of polymers. *J. Appl. Polym. Sci.*, 21: 449-454. doi:10.1002/app.1977.070210211
- [31] Mirabella, F. M. and Bafna, A. (2002), Determination of the crystallinity of polyethylene/olefin copolymers by thermal analysis: Relationship of the heat of fusion of 100% polyethylene crystal and the density. *J. Polym. Sci. B Polym. Phys.*, 40: 1637-1643.
- [32] Yassin A. E.B., Anwer M K., Mowafy H. A., El-Bagory I. M., Bayomi M. A., Alsarra I. A., (2010). Optimization of 5-fluorouracil solid-lipid nanoparticles: a preliminary study to treat colon cancer. *Int. J. Med. Sci.* 5 (6), 398-408. doi:10.7150/ijms.7.398.
- [33] Lee, J.S., Chae, G.S., An, T.K., Khang G., Cho S.H., Lee H.B. (2003). Preparation of 5-fluorouracil-loaded poly(L-lactide-co-glycolide) wafer and evaluation of in vitro release behavior. *Macromolecular Research*. 11, 3,183-188.
- [34] Hanafy, A. F.A. H., El-Egaky A. M., Mortada S. A. M., Molokhia A. M. (2009). Development of implants for sustained release of 5-fluorouracil using low molecular weight biodegradable polymers. *Drug Discoveries & Therapeutics*. 3, 6, 287-295.
- [35] Sairam M. Babu V.R, Naidu B.V.K., Aminabhavi T. M. (2006). Encapsulation efficiency and controlled release characteristics of crosslinked polyacrylamide particles. *Int. J. of Pharmaceutics*, 320, 131-136.
- [36] Gao H., Gu Y., Ping Q., (2005). The implantable 5-fluorouracil-loaded poly(l-lactic acid) fibers prepared by wet-spinning from suspension. *Journal of Controlled Release*. 3, 23, 325-332.



**AD Publications**

**Sector-3, MP Nagar, Bikaner,  
Rajasthan, India**

**[www.adpublications.org](http://www.adpublications.org), [info@adpublications.org](mailto:info@adpublications.org)**